AN INVESTIGATION OF HYPERSONIC FLOW

OVER

CONCAVE SURFACES AND CORNERS

P. A. Sullivan

Imperial College, London

October, 1963

A thesis submitted for the degree of

DOCTOR OF PHILOSOPHY

in the Faculty of Engineering,

University of London.

ABSTRACT

A theoretical and experimental investigation of inviscid hypersonic flow over concave surfaces and corners is described. The approximate theories available for inviscid hypersonic flow over slender bodies are reviewed, and it is shown that they give widely differing estimates of the surface pressure when applied to a concave surface. The similar solutions to the hypersonic small disturbance equations, which have previously been used to study the blunted slender convex body, are extended to cusped concave surfaces. A class of non-similar surfaces is obtained from the similar solutions. The regions on the cusped body where the similar solutions give physically unsatisfactory behaviour are examined, and a consistent interpretation is given. It is shown that, if a concave surface does not have discontinuities in slope or curvature, then the Newtonian plus centrifugal theory gives a fairly accurate simple estimate of the surface pressure. Approximate solutions for two of the mechanisms which can occur in concave surface flows - the formation of shock waves by compression waves, and the interaction of two shock waves of the same family - are presented. The reflected waves generated in these flows are shown to become very strong at hypersonic speeds and to have considerable effect on the surface pressures. Both the inadequacy of the existing approximate methods and the usefulness of the new similar solutions are demonstrated experimentally.

ACKNOWLEDGEMENTS

The author wishes to express his appreciation of the guidance and encouragement of his supervisor, Mr. J. L. Stollery, throughout the course of this investigation. Thanks are also due to Dr. N. C. Freeman for criticism and help, and to Mr. S. Michaelson (now of Edinburgh University) for his advice on the computation problems.

The author acknowledges the help given by the Imperial College Aeronautics Department Workshop Staff who constructed the models and apparatus.

From September 1960 until September 1962, the author held a Beit Fellowship for Scientific Research.

The author wishes to thank his wife for having persevered with the typing of the manuscript under such difficult conditions.

CONTENTS

	Page
Abstract	4
Acknowledgements	5
1) Introduction	
1.1) Scope of Investigation	9
1.2) Approximate Theories	11
1.3) Similar Solutions to the Hypersonic Small Disturbance Equations	13
1.4) Overfocussed Flows	16
1.5) Experimental Work	17
1.6) Note on Previous Work	18
2) Approximate Theories in Inviscid Hypersonic Flow	
2.1) The Theory of Thin Shock Layers	19
2.2) Shock Expansion or Simple Wave Theory	23
2.3) Tangent Wedge and Newtonian Rules	28
2.4) Application to a Concave Surface	30
3) Inviscid Hypersonic Flow over Cusped Bodies	
3.1) Basic Equations	32
3.2) Analysis of the Leading Edge Section	34
3.3) Equations of the Outer Region	37
3.4) Self-Similar Solutions to the Piston Equations	40
3.5) The Low-Entropy Layer	44

4) Application of Similar Solutions to Concave Surfaces

4.1) Integration of the Equations 51

4.2) Derivation of Non-Self Similar Surfaces 54

4.3) Results and Comments 56

5) On Overfocussed Flows

5.1) Wave Structure of the Idealized Flows 58

5.2) Solution of the Interaction Equations 63

5.3) An Exact Solution of the Flow over a Double Wedge 64

5.4) An Approximate Solution of the Interaction Equations 66

5.5) Strength of the Reflected Waves in the Double Wedge Flow 68

5.6) Strength of the Reflected Waves in the Centred Compression and Shock Flow 70

6) Experimental Facility and Models

6.1) Description of Facility 72

6.2) Structure of the Flow in the Working Section 73

6.3) Models 77

6.4) Instrumentation 80

7) Test Programme and Results

7.1) Programme 83

7.2) Results of Preliminary Experiments 85

7.3) Pressure Distributions on the Wedge 86

7.4) Pressure Distributions on the Overfocussed Surface 89

7.5) Pressure Distributions on the Underfocussed Surface 92

7.6) Pressure Distributions on the Cubic Surface 93

8) Comments on Experimental Facility

9) Conclusions 96

Appendices 99

List of Symbols 112

References 116

1) Introduction

1.1) Scope of Investigation

This thesis describes an investigation of inviscid hypersonic flow over concave surfaces.

In recent years the subject of inviscid flow at high Mach numbers has received considerable attention. Because of the difficulty of solving the exact equations of inviscid compressible fluid motion, much of the published work in this field has been concerned with the development of approximate methods. These methods are based on simplifying assumptions suggested by the features peculiar to hypersonic flow and appropriate to the body geometry.

The slender body problem is more difficult than the corresponding task for supersonic speeds. The shock waves are strongly curved and the flow behind them is highly rotational. For a given angle of deflection, the difference between the pressure rise produced by a Prandtl-Meyer compression wave and a shock wave increases rapidly with increase in Mach number M_{∞}. This is in contrast to flows at moderate M_{∞} for which Busemann's wave theory shows that the difference is only of third order in the angle of deflection.

To date, most investigations have considered only convex bodies. The flow about the slender convex airfoil and the blunted slender body have been examined in some detail. An excellent survey of the contributions to the field is given by Hayes and Probstein (1959, Chaps. 2 - 6). The reader is referred to this work

for detailed references.[c]

The current interest in such problems as ram-jet intakes and rocket flares has directed attention to the flow generated by concave surfaces and corners. However, the published work has to date been mainly confined to investigations of the viscous phenomena.

Inviscid concave surface flows can differ significantly from those over a convex surface. In addition to the leading edge shock, the compression waves generated at the surface can form shock waves. The shock layer is much more likely to be thin and dense. Leading edge bluntness effects are not as significant.

The Mach waves generated in the supersonic regions of any field can be divided into two groups or families. The principal family consists of those waves generated at the surface and which travel outwards from the body. The reflected waves are those generated at the shock waves and the slip-lines in the field and which travel towards the body. In the flow over concave surfaces, the reflected waves generated at the shock waves add to the reflected waves generated at the slip-lines. The resultant reflected waves are often strong when compared with the principal waves. This is in contrast to the flow over a convex surface where the two types of reflected wave usually tend to cancel, so that the resultant reflected waves can be much weaker than the principal waves.

---

[c]References are listed in alphabetical order in the Bibliography.

It is convenient to introduce the following classification for concave surface flows. An underfocussed flow occurs when the compression waves generated by a concave surface intersect the leading edge shock wave before they themselves form shock waves. If the compression waves form shock waves, then regions of the field will be overfocussed. The field generated behind a concave shock wave is underfocussed.

1.2) Approximate Theories.

To simplify the theoretical discussion the following assumptions will be made:

(i) The flow is two-dimensional or axially symmetric.

(ii) The leading edge is sharp. Then the corresponding inviscid field is everywhere locally supersonic.

(iii) The surfaces are slender.

(iv) The gas is perfect.

The theory appropriate for slender bodies in hypersonic flow is known as the small disturbance theory. In this theory the velocity perturbations are small compared with the free stream velocity, and the pressure perturbations are small when compared with the free stream dynamic pressure. However, in contrast to the behaviour at supersonic speeds, the shock waves are strong, the velocity perturbations are not small when compared with the free stream sound speed, and the pressure perturbations are large when compared with the free stream static pressure.

Consequently the hypersonic theory is non-linear, and inherently more difficult to utilise than the supersonic theory.

Hypersonic small disturbance theory introduces two major simplifications into the analysis. The first is the hypersonic similarity rule, by which the free stream Mach number M_∞ appears only in combination with a typical slope τ. The number of characteristic parameters defining the problem is then reduced by one. The second is the equivalence principle, by which a two-dimensional steady hypersonic small disturbance flow is equivalent to a one-dimensional unsteady flow. An indication of the simplification introduced by the equivalence principle is obtained by comparing the equations describing the oblique shock wave and Prandtl-Meyer wave deflections as given by the exact and the small disturbance theories. In the exact theory the conditions of the fluid just downstream of the shock or Prandtl-Meyer wave can only be expressed as implicit functions of the angle of deflection. Consequently the equations must be solved by iteration procedures. In the small disturbance theory, the conditions downstream can be expressed explicitly in terms of the deflection. Even with this simplification, numerical methods are still required for the construction of the field about general shapes.

To avoid using numerical methods, additional assumptions have to be made. A number of methods have been developed in this way. Those applicable to this problem are:

(i) the theory of thin shock layers,

(ii) shock expansion or simple wave theory,

(iii) tangent wedge and tangent cone rules,

(iv) Newtonian theory.

These theories will be outlined in § 2 and the applicability of the underlying assumptions to concave surface flows examined.

The approximate methods noted above can also be developed without making the slenderness assumption. They then assume a more complex form.

1.3) Similar Solutions to the Hypersonic Small Disturbance Equations.

From an analytic viewpoint, the most significant result of the hypersonic small disturbance theory is that it allows the use of the self-similar solutions to the one-dimensional unsteady flow equations. These solutions are obtained by imposing certain restrictions on the choice of boundary and initial conditions to reduce the problem to ordinary differential equations. With one exception, numerical methods are still required to solve the equations, but the methods are now much simpler.

Each similar solution has the property that the distribution in the space variable y at any given time t (or streamwise variable x in the equivalent hypersonic flow) is similar to the distribution in y at any other t. Similar solutions are available only for bodies of the form $y = Dx^k$, $y = e^x$ or $y = \ln x$.

The gas must be perfect, and M_∞ must be infinite so that the single shock wave present can be strong. The shock shape is similar to the body shape. The specific heat ratio γ and the exponent k specify the solution completely.

A complete accout of the similar solutions and their extensions has been given by Sedov (1957, Chapter 4) and a summary of some of the parts relevant to hypersonic flow is given by Hayes and Probstein (1959, pp.52 - 67).

The solution which is availaole in analytic form is the well known blast wave or constant energy flow. It is a singular solution of the differential equations and it occurs when the exponent $k = k_E = \frac{2}{3}$ in plane flow and when $k = \frac{1}{2}$ in axially symmetric flow. Its most important feature is that the body ordinate is vanishingly small, so that in the hypersonic flow it represents the flow over a blunted flat plate.

When $k_E < k < 1$ the body is a blunted slender convex ogive of aerofoil. When k = 1, the body is a wedge or a cone. When $k > 1$, the surface is cusped and concave. The single shock present is also concave, so that it is an underfocussed flow.

To date only the similar solutions in the range $k_E \leqslant k \leqslant 1$ have been studied. Numerical results for the axially symmetric case are quoted by Chernyi (1961, p. 86) and given by Kubota (1957). Kubota has also extended the solutions to a finite M_∞.

There are a number of physical difficulties associated with the similar solutions. On the convex body the equivalence principle fails at the nose, since $dy/dx \to \infty$ as $x \to 0$; and the strong shock assumption does not hold far downstream, where $dy/dx \to 0$. Lees and Kubota (1957) concluded that similar solutions were available only in the range $k_E \leqslant k \leqslant 1$, since for $k < k_E$ they apparently require the introduction of an infinite amount of energy at the origin. On the convex bodies ($k < 1$) the similar solutions predict zero density at the body surface, although the pressure is finite.

On the concave body the strong shock condition is not satisfied at the cusped leading edge, and the equivalence principle fails at a point well downstream because the body is no longer slender. The solution then predicts infinite density at the surface.

The systematic investigation of the behaviour of the field on convex power law bodies for large M_∞ in the regions where the similar solutions are not uniformly valid has not been undertaken until recently. Yakura (1962) by considering the inverse problem, and Freeman (1963) by considering the direct problem have provided a more satisfactory interpretation of the field.

In § 3 the behaviour of the hypersonic flow over a cusped body will be examined in the basic hypersonic limit $M_\infty \to \infty$. The first order differential equations for the regions near the cusp and close to the body (where the similar solutions are not valid)

will be obtained. It will be shown that there is a region for which the similar solutions are the correct first order approximation to the field, and further that they predict the correct first order pressure on the body surface.

In § 4 the similar solutions for concave two-dimensional shapes will be obtained. By constructing the equations for the streamlines, the similar solutions will be extended to a class of surfaces which have non-zero leading edge angles. Because they may be regarded as exact solutions to the hypersonic small disturbance equations for infinite M_∞, the similar solutions will be used as standards against which other approximate solutions to the small disturbance equations will be compared. Confirmation of the conclusions so drawn will be sought in the experimental results.

1.4) Investigation of Overfocussed Flows.

A characteristic feature of an overfocussed flow is the presence of discontinuities in the field in addition to that generated at the leading edge shock. This implies that even on simple surfaces the inviscid field is composed of several analytically different regions. This precludes the existence of any simple solutions such as are available for underfocussed flows.

Two basic mechanisms can be distinguished in an overfocussed flow. These are :

(i) the interaction of two shock waves of the same family,

(ii) the formation of shock waves by compression waves.

Both of these mechanisms generate finite reflected shock or expansion waves. Idealised examples of the basic mechanisms will be studied in § 5. These are:

(i) the flow over a double wedge, and

(ii) the centered compression and shock wave.

By constructing approximate solutions to the idealised flows, the strength of the reflected waves will be examined.

1.5) Experimental Work

Pressure measurements, taken in the Imperial College gun tunnel on concave surfaces, were intended to confirm the theoretical studies. To simplify interpretation, two-dimensional models were used in all tests. The shapes of the models were chosen so that viscous effects were not important. Three surfaces were examined. Each was designed to generate a specific type of flow:

(i) an overfocussed field,

(ii) an underfocussed field,

(iii) the flow over a power law surface.

A number of subsidiary experiments were conducted during the investigation. These fell into two groups:

(i) Assessment of the accuracy of the pressure measurements taken in the gun tunnel,

(ii) Determination of a correcting procedure to apply for the effects of the Mach number gradient produced by a conical nozzle on the measurements.

(iii) Investigation of the effects of side-plates on the two-dimensional models.

Because of their current interest, details of these experiments are included.

1.6) Note on Previous Work.

Surprisingly little attention has been given to inviscid concave surface flows. When this investigation began only two references were available. Johannesen (1952) conducted some experiments at $M_\infty = 2$ on slender surfaces, and showed that all of the effects which were important at large M_∞ were negligible. Barenblatt (1954) obtained a self-similar solution for an axially-symmetric exponential surface. Subsequently, Bird (1963) investigated the fields generated by bodies with positive discontinuities in profile slope by using the numerical method of characteristics. The relevant parts of his paper are discussed in § 5.5.

2) Approximate Theories in Inviscid Hypersonic Flow.

2.1) The Theory of Thin Shock Layers.

A characteristic feature of hypersonic flows is the tendency of the leading edge shock wave to wrap itself around the body as M_∞ increases. For sufficiently large M_∞, the shock shape in the neighbourhood of the forepart of a body approaches the body shape. The region between the shock wave and the body, known as the shock layer, is thin. The fluid in it is dense when compared with the free stream density, and is travelling at speeds which are not much less than the free stream speed. The shape of the streamlines in the shock layer is not much different from the body shape.

Because it is thin, space rates of change of quantities across the layer are assumed to be much greater than rates of change along it. In this respect, the fluid behaves as in the classical viscous boundary layer.

These observations have been used to develop a successive approximation scheme for constructing solutions (e.g. Freeman, 1956, and Chester, 1956). The density ratio across an oblique shock wave in a perfect gas is given by

$$\frac{\rho_\Delta}{\rho_\infty} = \left\{ \frac{\gamma-1}{\gamma+1} + \frac{2}{(\gamma+1) M_\infty^2 \sin^2\sigma} \right\}^{-1} \qquad (2.1$$

When $M_\infty = \infty$, $\frac{\rho_\infty}{\rho_\Delta} \to \frac{\gamma-1}{\gamma+1}$. Hence as $\gamma \to 1$ at $M_\infty = \infty$, $\rho_\Delta \to \infty$ and the shock wave must collapse onto the body. Therefore,

in a perfect gas the thin shock layer method is developed by applying the limit

$$\varepsilon \equiv \frac{\gamma - 1}{\gamma + 1} \to 0 \ , \quad M_\infty^{-2} \sim O(\varepsilon) \qquad (2.2$$

to the equations.

If the body is slender, the first approximation is particularly simple. This analysis was given by Cole (1957), and Chernyi (1961). Their results are quoted here. Let the shape of the body be given by $y = B(x)$ where x and y are co-ordinates parallel and perpendicular to the free stream. The stream is moving at velocity U_∞, and has density ρ_∞ and pressure p_∞.

Let ξ be the value x for which a streamline ψ passing through any point (x,y) crosses the shock wave. Then

$$2\psi = \frac{B^{1+j}(x)}{1+j} + O(\varepsilon) \qquad (2.3$$

The pressure at any point in the layer is given by

$$\frac{p(x,\xi)}{\rho_\infty U^2} = B_x^2(x) + \frac{B_{xx}(x)}{1+j}\left\{ B(x) - \frac{B^{1+j}(\xi)}{B(x)} \right\} \qquad (2.4$$

The pressure on the surface of the body is

$$\frac{p(x,0)}{\rho_\infty U_\infty^2} = B_x^2(x) + \frac{B_{xx}(x)\, B(x)}{1+j} \qquad (2.5$$

This is the slender body form of the well known Newtonian plus Centrifugal formula. The first term on the right hand side of Eq. 2.5 is the shock pressure rise. The second term is the difference in pressure across the shock layer associated with

its curvature; it is identically zero if the body profile curvature (i.e. $B_{xx}(x)$) is zero.

The density can be calculated from the entropy conservation law, which becomes

$$\frac{p}{\rho}(x,\xi) = U_\infty^2\left(\frac{1}{\varepsilon M_\infty^2} + B_\xi^2(\xi)\right) \qquad (2.6$$

The streamline shape is given by

$$y(x,\xi') = B(x) + (1+j)\int_0^{\xi'} \frac{\left\{M_\infty^{-2} + \varepsilon B_\xi^2\right\} B^j(\xi)\, B_\xi\, d\xi}{(1+j)\, B_x^2 + B_{xx}\left\{B(x) - \dfrac{B^{1+j}(\xi)}{B^j(x)}\right\}} \qquad (2.7$$

The shock position is found by calculating $y(x,x)$ from Eq. 2.7.

The application of this method to power law shapes $(y_b = Dx^k)$ is of particular interest. The surface pressure on such bodies is

$$\frac{P_b}{\rho_\infty U_\infty^2 \theta_b^2} = \left\{1 + \frac{k-1}{k(1+j)}\right\} \qquad (2.8$$

where $\theta_b = kDx^{k-1}$ is the local body slope. The density at the surface is given by

$$\frac{\rho_b}{\rho_\infty} = \varepsilon M_\infty^2 \theta_b^2 \left\{1 + \frac{k-1}{k(1+j)}\right\} \qquad (2.9$$

when $k > 1$. According to this formula, $\rho_b \to \infty$ as $M_\infty \to \infty$.

When applied to convex surfaces, Eq. 2.5 is found to considerably underestimate the surface pressure. This occurs

because the shock layer is rarely thin, particularly if the body is slender. Usually the shock layer is thin only in the neighbourhood of the stagnation region; but in this region a different analysis is required because the shape of the streamlines does not approach the body shape.

There are three other situations in which the thin shock layer theory exhibits a physically unsatisfactory behaviour. According to Eq. 2.5, on a convex surface, for which $B_{xx} < 0$, at some point sufficiently far downstream from the leading edge, the pressure difference across the shock layer will balance the shock pressure rise. At this point (for which $B_x > 0$) the surface pressure becomes identically zero. According to Eq. 2.7, $y(x, \xi) \to \infty$ when this occurs, so that theory is not uniformly valid. The theory also fails downstream of points of discontinuity of profile curvature and slope. At discontinuities in curvature, the theory predicts a discontinuity in the surface pressure, when it is known from the theory of characteristics that discontinuities in pressure gradient will occur. The behaviour downstream of discontinuities in slope is of interest when ϑ_b increases through the discontinuity. The theory fails in this case because it does not take account of the shock pattern. (c.f. § 5).

2.2) Shock-Expansion (Simple Wave) Theory.

The method of characteristics provides a technique for the exact solution of the supersonic regions of an inviscid flow field. However it usually requires the use of numerical techniques, so that in practice its application is extremely laborious.

Epstein (1931) suggested a method, known as the shock-expansion or simple wave theory, which is a simplification of the method of characteristics. By this method, the properties on the surface of a two-dimensional aerofoil immersed in a flow which is everywhere supersonic are calculated by neglecting the effect of the reflected Mach waves. Hence the pressure distribution on the surface of a convex aerofoil is obtained by calculating conditions at the leading edge by the oblique shock relations, and then matching a Pfandtl-Meyer expansion to the body geometry. It is simple to apply, and it yields an estimate of the pressure which depends only on the local body shape.

The method has been extended by Eggers and Syvertson (1952) to permit the calculation of the shock shape and the field, and has been adapted to the construction of axially symmetric flows.

Consider its extension to concave surfaces. As on a convex body, at the leading edge and at positive discontinuities in profile slope, the oblique shock relations are used to obtain the pressure just downstream. Over the remainder of the profile isentropic simple wave theory is used.

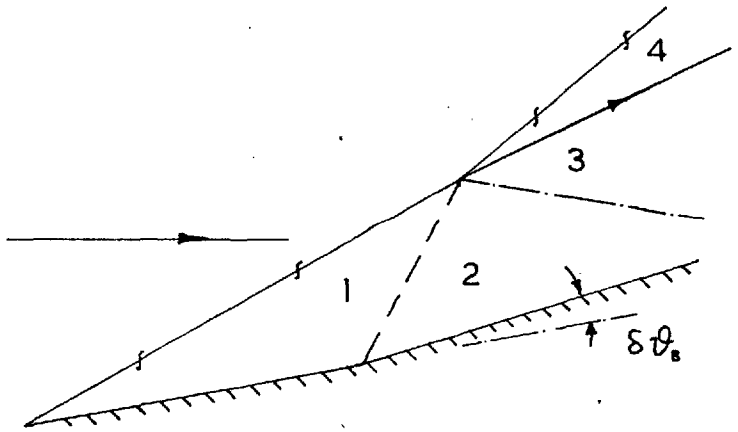


FIG. 2.1 : REFLECTION OF A PRINCIPAL WAVE AT A SHOCK WAVE

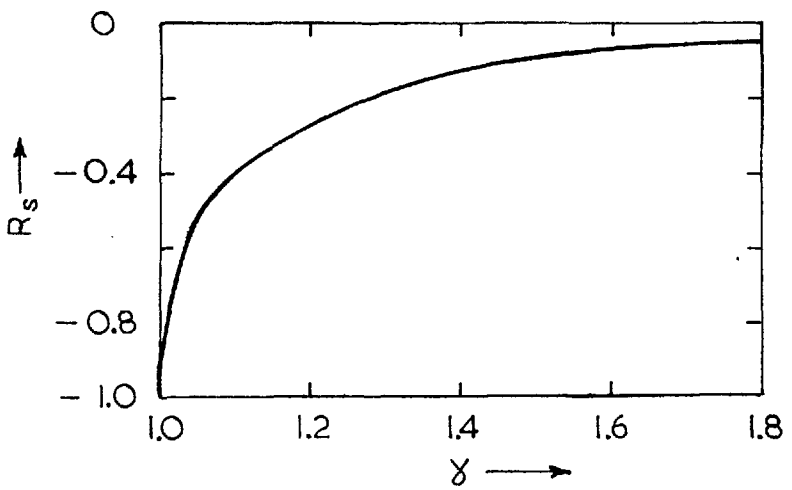


FIG. 2.2 : EFFECT OF γ ON REFLECTION AT A SHOCK WAVE.

Hayes and Probstein (1959), giving an analysis originally due to Lighthill (1949) and Chu (1952), show that for $M_\infty = \infty$ and if the shock angle $\sigma \ll 1$, then

$$R_s \simeq \frac{2\sqrt{\varepsilon} - \sqrt{\gamma(1-\varepsilon)}}{2\sqrt{\varepsilon} + \sqrt{\gamma(1-\varepsilon)}} \quad \text{as } \Delta\vartheta \to 0 \qquad (2.11$$

This limiting value of R_s depends only on γ. A plot of R_s against γ is given in Fig. 2.2. R_s is negative and is small if γ is not close to one. Hence on a convex surface ($\Delta\vartheta < 0$) the incident expansion will be reflected as a weak compression. However as $\gamma \to 1$, $R_s \to (-1)$, so that a principal wave is reflected undiminished in strength.

The reflection process at the slip-lines is depicted in Fig. 2.3. A reflection coefficient R_v is defined as before:

$$R_v = \frac{p_3 - p_2}{p_2 - p_1} \qquad (2.12$$

By matching the pressures on either side of the slip-line just downstream of the reflection, it can be shown that, if $M_i \gg 1$ and as $\Delta\vartheta \to 0$:

$$R_v \simeq \frac{M_B - M_A}{M_B + M_A} \qquad (2.13$$

When the slip-line is weak, $M_B \approx M_A$ and $R_v \approx 0$.

The analysis of the effect of R_v on the reflected waves given by Hayes and Probstein (1959, p. 271) tacitly assumes that the generating surface is convex, so that $M_B > M_A$. Then, since R_v is positive and the incident principal wave is an expansion, the reflected wave generated at the slip-lines is an expansion.

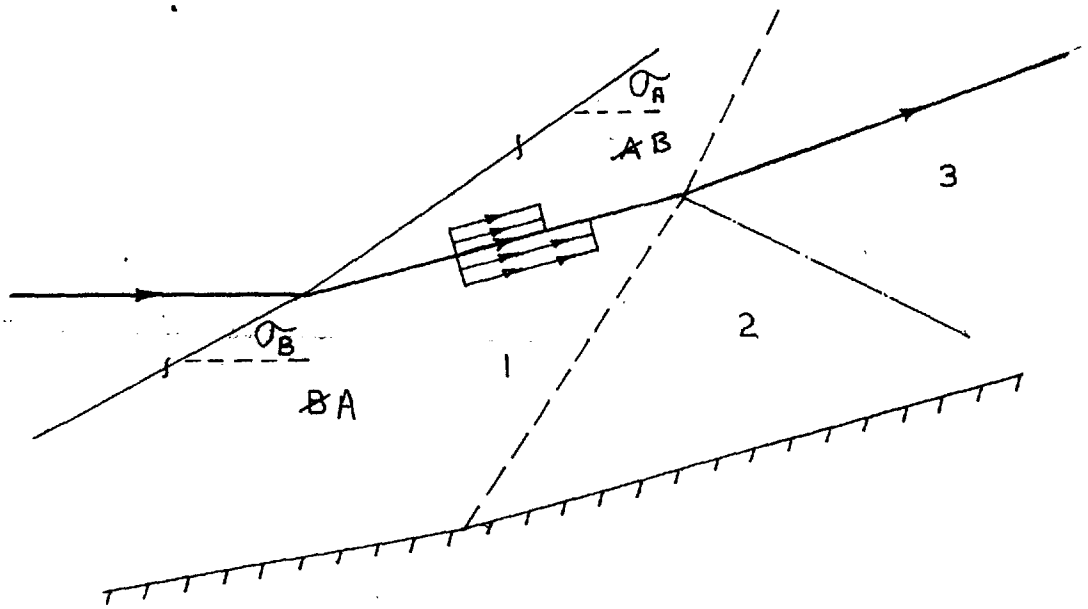


FIG. 2.3: THE IDEALISED SUPERSONIC SHEAR LAYER.

Therefore the reflected waves generated at the shock and at the slip-lines in a convex surface flow tend to cancel, and will be much weaker than consideration of either mechanism alone will indicate.

Consider now the behaviour of R_V in the flow over a concave surface, in which the principal waves are compressions. As R_S remains negative the reflected waves generated at the shock will be expansions. But as the shock is concave, in Eq. 2.13, $M_B < M_A$ and R_V is now negative. Hence the reflected waves generated at the slip-lines are expansions. In contrast to the behaviour on a convex surface, the two types of reflected wave generated on a concave surface add. The strength of the reflected waves will therefore increase with increase in the strength of the slip-lines.

Numerical comparisons with exact solutions obtained by the method of characteristics* have shown that, if $\gamma > 1.3$, the simple wave method gives excellent results on slender convex bodies with sharp leading edges. As $\gamma \to 1$ the error increases rapidly. It is expected that the method will overestimate the surface pressure when it is applied to an underfocussed flow on a a concave surface. The error should increase with increase in

---

* see for example the results quoted in

(i) Hayes and Probstein (1959) p274 &p276.

(ii) Chernyi (1961) p193, Fig. 4.15.

and the curvature of the profile.

For slender bodies the hypersonic small disturbance approximations to the shock and simple wave relations can be used. The application of the method is particularly simple. The angle of shock wave at the leading edge (σ_L) is given by

$$K_{SL} = M_\infty \sigma_L = \frac{K_L}{2(1-\varepsilon)} + \sqrt{\left(\frac{K_L}{2(1-\varepsilon)}\right)^2 + 1} \quad , \qquad (2.14$$

where $K_L = M_\infty \vartheta_L$ and ϑ_L is the leading edge slope. The pressure and Mach number behind the shock are then given by

$$\frac{p_L}{p_\infty} = (1+\varepsilon) K_{SL}^2 - \varepsilon \quad , \qquad (2.15$$

$$\frac{M_L^2}{M_\infty^2} = \frac{K_{SL}^2}{\{(1+\varepsilon) K_{SL}^2 - \varepsilon\}\{\varepsilon K_{SL}^2 + (1-\varepsilon)\}} \quad . \qquad (2.16$$

The Mach number and pressure distribution over the rest of the profile are then given by

$$\frac{1}{M} - \frac{1}{M_L} = \frac{\varepsilon}{1-\varepsilon}[\vartheta - \vartheta_L] \; ; \quad p/p_L = \{M_L/M\}^{\frac{1+\varepsilon}{\varepsilon}} , \qquad (2.17$$

where M is the Mach number, p is the pressure and ϑ is the local body slope.

2.3) Tangent Wedge and Newtonian Rules.

According to the tangent wedge rule, the pressure at a given point on the surface of a two-dimensional body is estimated by calculating the pressure generated on an "equivalent" wedge of angle equal to the local slope of the body, and which is immersed in the same free stream. The method is based on the physical idea that, if the shock layer is thin, then the properties on the surface cannot differ greatly from those just behind the shock wave. This is discussed by Lees (1955).

The advantage of this method is its simplicity. When the body is slender the equivalent wedge pressure may be obtained by using the hypersonic small disturbance equations, (Eq. 2.15) and the surface pressure is then given by a simple explicit expression. The method yields an estimate which depends only on the local surface slope.

The rule has been found useful on slender convex surfaces, particularly when the simple wave method breaks down; such as when γ is close to one, or when a blunt leading edge generates a strong shear layer adjacent to the surface.

This method neglects the wave structure of the field completely, and therefore is totally inadequate in regions where strong or finite waves of either family are generated. In contrast to the simple wave theory, the tangent wedge rule cannot be applied to those regions of the slender body having a negative slope.

The agreement mentioned above is therefore fortuitous.

A method which has often been used because of its extreme simplicity is based on one of the concepts of Newton's gas dynamics. The individual gas particles in the free stream are assumed to move in straight lines. When they hit the body they lose only their normal momentum normal to the surface and then slide along the surface in an extremely thin layer. The momentum law then requires that

$$p_b = \rho_\infty U_\infty^2 \sin^2 \vartheta_b \qquad (2.18$$

Examination of the oblique shock relations shows that this expression is exact in the thin shock layer limit Eq. 2.2 for the flow over a wedge. Hence it can be considered as an approximation to the tangent wedge rule.

The thin shock layer theory shows that the centrifugal pressure difference across the shock layer is of the same order of magnitude as the shock pressure rise. Therefore the use of the Newtonian formula without the centrifugal term is inconsistent. In spite of this, Eq 2.18 gives a better estimate of the surface pressure on convex surfaces than does the Newtonian plus centrifugal formula. This occurs because the Newtonian formula underestimates the shock pressure rise, and the centrifugal term subtracts from the shock pressure rise.

2.4) Application to Concave Surfaces

The approximate methods are applied to an under-focussed flow on a concave surface. The forward part of the body has the form:

$$\vartheta = \vartheta_L (x + x^3), \qquad (2.19$$

where ϑ_L is the leading edge angle. To demonstrate the effect of discontinuity in curvature, the surface is continued as a ramp (that is, at constant slope $\vartheta_R = 2\vartheta_L$) for $x > 1$

The slender body forms of the theories are used. Therefore (Hayes and Probstein, 1959, p36)

$$\frac{C_p}{\vartheta_L^2} = f(M_\infty \vartheta_L, \gamma) \qquad (2.20$$

The surface pressure distrib utions for $\vartheta_L = 0.1$, $\gamma = 1.4$ and $M_\infty = 10$ are given in Fig. 2.4. The theories give widely differing estimates. The tangent wedge rule gives the correct pressure at the leading edge, and far downstream ~~upstream~~ on the ramp. All of the theories predict a constant pressue on the ramp. The Newtonian plus centrifugal gives a discontinuity at the junction.

To demonstrate the accuracy of the small disturbance assumption, the pressure on the ramp, estimated by the simple wave theory, using the exact shock and Prandtl-Meyer wave relations is given. The error is less than 2%.

In Fig. 2.5, the effect of variation of M_∞ and ϑ_L

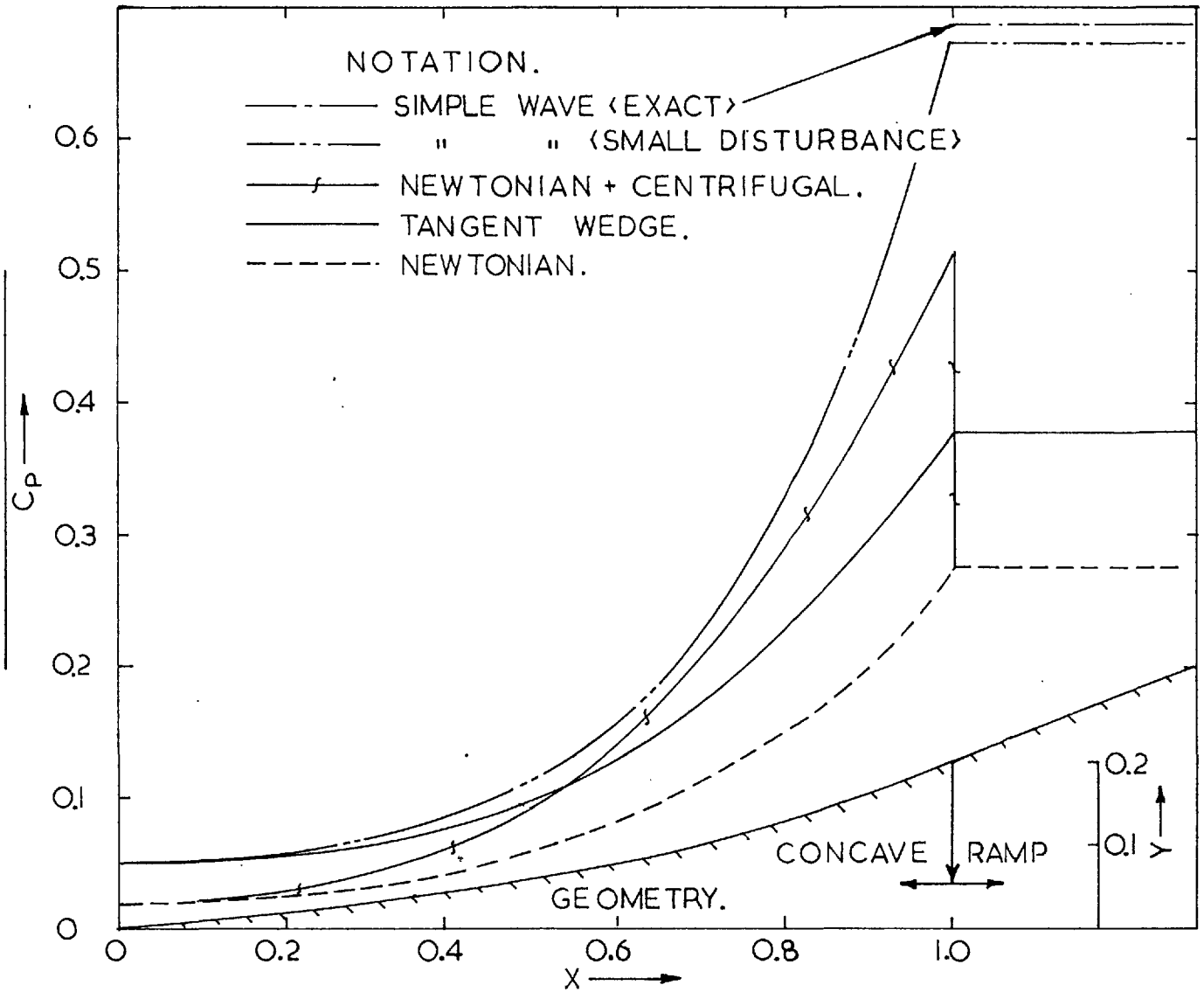


FIG. 24: COMPARISON OF APPROXIMATE THEORIES ON A CONCAVE SURFACE.

on the estimates of ramp pressure is given. The differences betweeen the estimates increase as $M_\infty \theta_L$ increases.

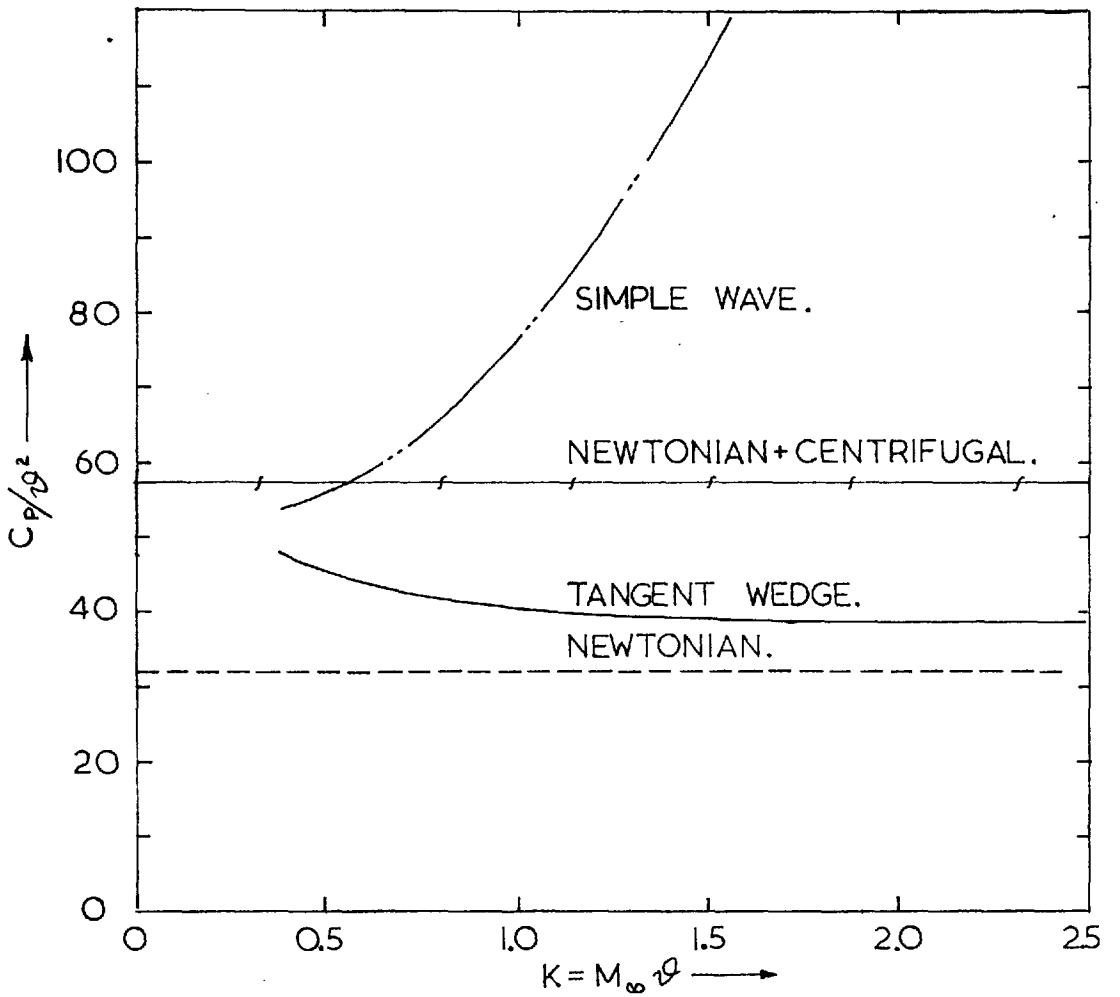


FIG 2.5 : EFFECT OF $K=M_\infty \vartheta$ ON THE ESTIMATES OF RAMP PRESSURE.

3) Inviscid Hypersonic Flow over Cusped Bodies.

3.1) Basic Equations

The equations describing the two-dimensional or axially symmetric rotational flow of an inviscid perfect gas are:

$$\frac{\partial}{\partial x}(\rho u) + \frac{\partial}{\partial y}(\rho v) + j\rho v/y = 0, \quad (3.1a$$

$$u\frac{\partial u}{\partial x} + v\frac{\partial u}{\partial y} + \frac{1}{\rho}\frac{\partial p}{\partial x} = 0, \quad (3.1b$$

$$u\frac{\partial v}{\partial x} + v\frac{\partial v}{\partial y} + \frac{1}{\rho}\frac{\partial p}{\partial y} = 0, \quad (3.1c$$

$$u\frac{\partial}{\partial x}\left(\frac{p}{\rho^{\gamma}}\right) + v\frac{\partial}{\partial y}\left(\frac{p}{\rho^{\gamma}}\right) = 0. \quad (3.1d$$

where u and v are the components of velocity in the x and y directions respectively, ρ is the density and p is the pressure. The operator $j = 0$ for two-dimensional and $j = 1$ for axially symmetric flows. Sufficiently far upstream, the stream is uniform and is travelling in the x-direction, thus:

$$\lim_{x \to -\infty} u = U_{\infty}, \quad v = 0, \quad \rho = \rho_{\infty}, \quad p = p_{\infty}. \quad (3.2$$

The boundary condition at the body, which is described by $y = y_b(x)$ is that the surface is a streamline:

$$\frac{v}{u} = \frac{dy_b}{dx} \quad \text{at } y = y_b(x) \qquad (3.3$$

It is assumed that there is only one shock present in the field, and that it is attached to the leading edge of the body. Its shape, which is part of the solution to the problem, is expressed as

$$y = y_s(x) \;, \quad \frac{dy_s}{dx} = \tan\sigma \qquad (3.4$$

The jump conditions which hold across the shock wave can be cast into the form:

$$\frac{p_s}{\rho_\infty U_\infty^2} = \frac{\delta}{\gamma} + (1-\varepsilon)\{\sin^2\sigma - \delta\} \qquad (3.5a$$

$$\frac{\rho_\infty}{\rho_s} = \varepsilon + \frac{(1-\varepsilon)\,\delta}{\sin^2\sigma} \qquad (3.5b$$

$$\frac{v_s}{U_\infty} = (1-\varepsilon)\cot\sigma\{\sin^2\sigma - \delta\} \qquad (3.5c$$

$$\frac{u_s}{U_\infty} = 1 - (1-\varepsilon)\{\sin^2\sigma - \delta\} \qquad (3.5d$$

where $\delta = M_\infty^{-2}$ and the subscript s denotes quantities just downstream of the shock. The slope of the streamlines just downstream of the shock is

$$\cot \vartheta_s = \tan\sigma \left\{ \frac{1-\varepsilon}{(\sin^2\sigma - \delta)} - 1 \right\} \qquad (3.5e$$

The behaviour of the field will be examined in the basic hypersonic limit $\delta = M_\infty^{-2} \to 0$. A characteristic feature of this problem is that the parameter M_∞ appears in the formulation only in the shock jump conditions. Hence the behaviour of the field in the limit $\delta \to 0$ is determined by the behaviour of the shock conditions in that limit. If in some region σ becomes much larger than $\delta^{1/2}$ as $\delta \to 0$, then the shock is said to be strong in the hypersonic sense, and the field behind it is said to be Mach number independent. The shape of the shock wave is then determined primarily by the body shape. If, on the other hand, there is a region where the Mach number is at least as important as the body slope in determining the shock slope, then the shock is said to be weak and the flow behind it is Mach number dependent. Such behaviour occurs at sufficiently large distances from any body, or if for given M_∞, the body is sufficiently slender.

3.2) Analysis of Conditions Near the Leading Edge.

The shape of a cusped body may be conveniently expressed in the form

$$y_b = D x^k \left[1 + \sum_{i=1}^{n} a_i x^i \right], \quad k > 1 \qquad (3.6$$

The slope ϑ_b of such a body tends to zero as $x \to 0$. Therefore at the origin, the leading edge shock becomes a Mach wave, $\sin \sigma(0) = \delta^{1/2}$. For some region downstream of the origin therefore $\sigma \sim O(\delta^{1/2})$. Hence $\vartheta_b \sim O(\delta^{1/2})$ in this region, which will be called the leading edge section. Since $y_b \sim O(x^k)$ as $x \to 0$, it follows that in the leading edge section

$$x \sim O(\delta^{\frac{1}{2(k-1)}}); \quad y \sim O(\delta^{k/2(k-1)}) \tag{3.7}$$

To find the limiting behaviour of the shock conditions in the ~~slender~~ leading edge section put $\sigma = \delta^{1/2}\bar{\sigma}$, so that $\bar{\sigma} \sim O(1)$ in the leading edge section. In the limit $\delta \to 0$, the first order approximations to Eqs. 3.5 become

$$\frac{p_s}{\rho_\infty U_\infty^2 \delta} = 1/\gamma + (1-\varepsilon)\{\bar{\sigma}^2 - 1\} \tag{3.8a}$$

$$\frac{\rho_\infty}{\rho_s} = \varepsilon + \frac{(1-\varepsilon)}{\bar{\sigma}^2} \tag{3.8b}$$

$$\frac{v_s}{U_\infty \delta^{1/2}} = (1-\varepsilon)\bar{\sigma}^{-1}\{\bar{\sigma}^2 - 1\} \tag{3.8c}$$

$$\frac{u_s}{U_\infty} = 1 - \delta(1-\varepsilon)\{\bar{\sigma}^2 - 1\} \tag{3.8d}$$

Thus the properties of the fluid which has passed through the

the leading edge section are Mach number dependent. Typically, behind the shock wave, $M_s \sim O(\delta^{-1/2})$ and the slope of the Mach lines is

$$(u \pm v) \sim O(\delta^{1/2}) \qquad (3.9$$

Guided by the orders just behind the shock wave the following reduced quantities are introduced to study the behaviour of Eqs. 3.1 in the limit $\delta \to 0$

$$\frac{p}{\rho_\infty U^2} = \delta \bar{p} \quad , \quad \frac{\rho}{\rho_\infty} = \bar{\rho} \qquad (3.10a$$

$$\frac{v}{U_\infty} = \delta^{1/2} \bar{v} \quad , \quad \frac{u}{U_\infty} = 1 + \delta \bar{u} \qquad (3.10b$$

Also, put

$$\bar{x} = \frac{x}{\ell} \delta^{-1/2(k-1)} \quad , \quad \bar{y} = \frac{y}{\ell} \delta^{-k/2(k-1)} \qquad (3.11$$

where ℓ is a typical length. Eq. 3.6 shows that a convenient $\ell = D^{1/1-k}$. All the reduced quantities are assumed to be $O(1)$ in the leading edge section.

The first order approximation to Eq. 3.1 is

$$\frac{\partial \bar{u}}{\partial \bar{x}} + \bar{v} \frac{\partial \bar{u}}{\partial \bar{y}} + \frac{1}{\bar{\rho}} \frac{\partial \bar{p}}{\partial \bar{x}} = O(\delta) \qquad (3.12a$$

$$\frac{\partial \bar{v}}{\partial \bar{x}} + \bar{v} \frac{\partial \bar{v}}{\partial \bar{y}} + \frac{1}{\bar{\rho}} \frac{\partial \bar{p}}{\partial \bar{y}} = O(\delta) \qquad (3.12b$$

$$\frac{\partial \bar{\rho}}{\partial \bar{x}} + \frac{\partial}{\partial \bar{y}}(\bar{\rho}\bar{v}) + j\,\frac{\bar{\rho}\bar{v}}{\bar{y}} = O(\delta), \quad (3.12c$$

$$\frac{\partial}{\partial \bar{x}}\left(\bar{P}/\bar{\rho}^{\gamma}\right) + \bar{v}\,\frac{\partial}{\partial \bar{y}}\left(\bar{P}/\bar{\rho}^{\gamma}\right) = O(\delta). \quad (3.12d$$

The body condition becomes :

$$\bar{v} = d\bar{y}/d\bar{x} = k\,\bar{x}^{k-1} + O\left(\delta^{\frac{1}{2}\left(\frac{1}{k-1}\right)}\right). \quad (3.13$$

Eqs. 3.12 are identical with the hypersonic small disturbance equations. The boundary conditions imply that solutions to this system of equations can only be obtained by numerical techniques such as the method of characteristics. The leading edge section contains a smaller section adjacent to the origin, where $\bar{\sigma} = 1 + \nu$, $\nu << 1$. The classical perturbation theory applies in this region.(See Appendix 9.)

3.3) Equations of the Outer Region

Just downstream of the leading edge section there must be a region for which $\sigma \to 0$ as $\delta \to 0$ but for which $\sigma/\delta^{\frac{1}{2}} \to \infty$ as $\delta \to 0$. In this region (which is in the outer region)

$$\sigma \sim O(\delta^{\beta}), \quad \tfrac{1}{2} > \beta \geq 0 . \quad (3.14$$

Let $\sigma = \delta^{\beta}\sigma^{*}$; then $\sigma^{*} \sim O(1)$ when Eq. 3.14 holds.

Consider the behaviour of the oblique shock relations

in this region. Typically, Eq. 3.5a becomes

$$\frac{p_\Delta}{\rho_\infty U_\infty^2 \delta^{2\beta}} = (1-\varepsilon)\sigma_*^2 - \frac{\varepsilon}{\gamma}\delta^{1-2\beta} + O(\delta^{2\beta}) \quad (3.15$$

Hence

$$\frac{p_\Delta}{\rho_\infty U^2 \delta^{2\beta}} = (1-\varepsilon)\sigma_*^2 + O(\delta^\tau) \quad (3.16a$$

where

$$\left.\begin{aligned} \tau &= 1-2\beta \quad , \quad \beta > 1/4 \\ \tau &= 1/2 \quad , \quad \beta = 1/4 \\ \tau &= 2\beta \quad , \quad \beta < 1/4 \end{aligned}\right\} \quad \tau \leq 1/2 \quad (3.17$$

Hence the error is due to the strong shock assumption if $\beta > 1/4$ and to the slenderness approximation if $\beta < 1/4$. The other shock relations become

$$\frac{\rho_\Delta}{\rho_\infty} = \varepsilon^{-1} + O(\delta^{1-2\beta}) , \quad (3.16b$$

$$\frac{v_\Delta}{U_\infty \delta^\beta} = (1-\varepsilon)\sigma_* + O(\delta^\tau), \quad (3.16c$$

$$\{u_\Delta/U_\infty - 1\} = -(1-\varepsilon)\delta^{2\beta}\sigma_*^2\{1 + O(\delta^\tau)\}. \quad (3.16d$$

Accordingly the following set of reduced variables are introduced

to replace Eqs. 3.12:

$$\frac{p}{\rho_\infty U^2 \delta^{2\beta}} = \bar{p} \quad , \quad \rho/\rho_\infty = \bar{\rho} \qquad (3.18$$

$$\frac{v}{U_\infty \delta^{\beta}} = \bar{v} \quad , \quad \frac{u}{U_\infty} = 1 + \delta^{2\beta}\bar{u}$$

In the region where Eq. 3.14 holds, $x \sim O(\delta^{\beta/k-1})$, $y \sim O(\delta^{k\beta/k-1})$

Hence the co-ordinate distortions are introduced:

$$x/\ell = \delta^{\beta/k-1}\bar{x}; \quad y/\ell = \delta^{k\beta/k-1}\bar{y} \qquad (3.19$$

The introduction of the reduced variables into Eqs. 3.1 leads to Eqs.3.12 as the first approximation, but the order of error is now δ^{γ}. Hence there is a region just downstream of the leading edge section where the shock is strong and where the hypersonic small disturbance equations hold. The region of the body where the small disturbance equations hold will be called the slender section.

It should be noted that the derivation of the hypersonic small disturbance equations given above is not valid when $\beta = 0$. However for sufficiently small δ there must be a region for which $\sigma \sim O(1)$ as $\delta \to 0$ and yet $\sigma \ll 1$. The slenderness approximations hold and the small disturbance equations apply. Therefore to define the downstream bound of the slender section the usual slenderness parameter must be introduced.

In the limit $\delta \to 0$, the leading edge section becomes

vanishingly small, while the slender section has a finite length.

3.4) The Self-Similar Solutions to the Piston Equations

Eqs. 3.12 can be rewritten in the physical variables and transformed to the piston equations. If $x = U_\infty t$, then the equations for p, ρ and v become

$$\frac{\partial v}{\partial t} + v\frac{\partial v}{\partial y} + \frac{1}{\rho}\frac{\partial p}{\partial y} = 0 \qquad (3.20a$$

$$\frac{\partial \rho}{\partial t} + \frac{\partial}{\partial y}(\rho v) + j\rho v/y = 0 \qquad (3.20b$$

$$\frac{\partial}{\partial t}\left(p/\rho^\gamma\right) + v\frac{\partial}{\partial y}\left(p/\rho^\gamma\right) = 0 \qquad (3.20c$$

The corresponding shock conditions become (with the Mach dependence retained)

$$\frac{p_s - p_\infty}{\rho_\infty V_s^2} = (1-\varepsilon)\left\{1 - a_\infty^2/V_s^2\right\}, \quad a_\infty^2 = U_\infty^2\delta \ , \qquad (3.21a$$

$$\frac{\rho_\infty}{\rho_s} = \varepsilon + (1-\varepsilon)a_\infty^2/V_s^2 \qquad (3.21b$$

$$\frac{v_s}{V_s} = (1-\varepsilon)\left\{1 - a_\infty^2/V_s^2\right\} \qquad (3.21c$$

on

$$y_s = Y_s(t); \quad \frac{dY_s}{dt} = V_s = U_\infty \sigma \qquad (3.22$$

The body condition becomes

$$v = \frac{dY_B}{dt} = U_\infty \vartheta_b \qquad (3.23$$

on

$$y = Y_B(t) = t^k \sum_i^s c_i t^i \qquad (3.24$$

A frequently used method of obtaining solutions to partial differential equations is to search for the conditions under which they may be reduced to ordinary differential equations. Solutions obtained in this way are called self-similar. The conditions under which the piston equations have self-similar solutions can be obtained by the Π-theorem of dimensional analysis.

An abbreviated account of the origins of the similarity exploited here is given below. Sedov (1959) gives a rigorous and detailed discussion of the similarity.

Inspection of Eqs. 3.22 and 3.24 shows that the dependent variable ϕ, which may be taken as typical, is a function of (s+7) independent variables and parameters; thus

$$f(\phi; y, t; a_\infty, \rho_\infty, \gamma, k, c_0, c_1, c_2 .. c_s) = 0. \qquad (3.25$$

By the Π-theorem, since there are three independent dimensions, Eq. 3.25 can be reduced to a relation between (s+5) non-dimensional groups. The quantities chosen as having the independent dimensions

are picked so that , in the non-dimensional expression, certain of the non-dimensional groups can be set to zero or a constant without making the problem trivial. Here y, t, ρ_∞ have independent dimensions and satisfy this criterion. Hence the non-dimensional groups corresponding to the dependent variables are:

$$P = \frac{pt^2}{\rho_\infty y^2}, \quad R = \frac{\rho}{\rho_\infty}, \quad V = \frac{vt}{y} \tag{3.26a}$$

and to the independent variables and parameters are .

$$A_\infty = \frac{a_\infty t}{y}; \quad \bar{C}_0 = \frac{y}{C_0 t^k}, \quad \bar{C}_1 = \frac{y}{C_1 t^{k+1}}, \ldots, \bar{C}_s \tag{3.26b}$$

Hence

$$P = P(A_\infty, \bar{C}_0, \bar{C}_1, \ldots \bar{C}_s, \gamma, k) \tag{3.26c}$$

and corresponding relations hold for R and V.

Examination of Eqs. 3.26 shows that there are just two cases in which P, R and V depend only on a single combination, φ, of x and t, $\varphi = \varphi(x,t)$. These are:

(i) if $\bar{C}_1 = \bar{C}_2 = \bar{C}_3 = \ldots = \bar{C}_s = 0$ and $k = 1$.

Hence

$$P = P\left(\frac{a_\infty t}{y}, \frac{C_0 t}{y}\right) = P(\varphi) \text{ where } \varphi = \frac{t}{y} \tag{3.27}$$

(ii) if $\bar{C}_1 = \bar{C}_2 = \cdots = \bar{C}_s = 0$ and $a_\infty = 0$.

Then

$$P = P\left(\frac{C_0 t^k}{y}\right) = P(\varphi) \text{ where } \varphi = \frac{C_0 t^k}{y} \tag{3.28}$$

In both cases there is now only one independent variable φ so that P, R, V satisfy ordinary differential equations. In the equivalent hypersonic flow, case (i) corresponds to the flow over a wedge or cone, whilst case (ii) corresponds to the flow over a power law body at $M_\infty = \infty$.

We set up the equations for case (ii). Introducing Eqs. 3.26 into Eqs. 3.21, we obtain

$$\varphi\left\{\frac{1}{R}\frac{dR}{d\varphi}(V-k) + \frac{dV}{d\varphi}\right\} + (1+j)V = 0 \qquad (3.29a$$

$$\varphi\left\{(V-k)\frac{dV}{d\varphi} + \frac{1}{R}\frac{dP}{d\varphi}\right\} + V(V-1) + \frac{2P}{R} = 0 \qquad (3.29b$$

$$\varphi(V-k)\left\{\frac{1}{P}\frac{dP}{d\varphi} - \frac{\gamma}{R}\frac{dR}{d\varphi}\right\} + 2(V-1) = 0 \qquad (3.29c$$

These are the equations given by Sedov (1959) p.155). The boundary condition at the body becomes

$$V_B = k \text{ at } \varphi = 1 \qquad (3.30$$

Since $a_\infty = 0$, the shock position y_s, and hence φ_s can only be a function of γ, k, C_0, ρ_∞, t. But φ_s is dimensionless. Since C_0, ρ_∞, t, have independent dimensions, it is impossible to form a non-dimensional combination from them, Therefore φ_s = constant, and

$$y_s = \varphi_s(\gamma, k)\, C_0 t^k . \qquad (3.31$$

By Eq. 3.1, Eqs. 3.21 become, when $a_\infty = 0$:

$$V_s = (1-\varepsilon)k$$
$$R_s = (\varepsilon)^{-1} \qquad (3.32$$
$$P_s = (1-\varepsilon)k^2$$

at $y_s = \phi_s C_o t^k$

Eqs. 3.29 exhibit a singular behaviour near the body where $V = k$. It can be shown that

$$V - k = V_o(\phi - 1) + \cdots \qquad (3.33a$$

$$P = P_o + P_1(\phi - 1)^{2-\alpha} \qquad (3.33b$$

$$R = R_o(\phi - 1)^{-\alpha} \qquad (3.33c$$

where

$$\alpha \equiv \frac{2(k-1)}{2(k-1) + \gamma k(1+j)} \qquad (3.33d$$

and V_o, R_o and P_o are constants which depend on the boundary conditions at the shock. Hence, when $k > 1$, $R \to \infty$ as $\phi \to 1$; and when $k < 1$, $R \to 0$ as $\phi \to 1$. This behaviour was first noted by Lees and Kubota (1957). Since P remains finite at the body, the temperature is infinite at the body for $k < 1$ and zero when $k > 1$.

3.5) The Low-Entropy Layer.

So that Eqs. 3.32 may hold at $M_\infty = \infty$ it is necessary that the oblique shock relations tend to the Mach-independent form Eqs. 3.16 as $\delta \to 0$. But in the (vanishingly small) leading edge

section the shock relations tend to the Mach-dependent form Eqs. 3.8 This implies that certain of the properties of the fluid which has passed through the shock in the leading edge section will be Mach-dependent.

The asymptotic behaviour of the field in the limit $\delta \to 0$ is depicted in Fig. 3.1. Region I is the leading edge section. That part of the body upstream of CG is the slender section. Regions II and IV comprise the outer region. Region III contains the fluid which has crossed the shock in the leading edge section and has passed downstream. The entropy in region III is much less than that of the field above it:

$$S_{\underline{III}}/S_{\underline{II}} \sim O(\ln \delta)$$

For this reason it is called a low-entropy layer. It corresponds to the conventional entropy layer generated downstream on a blunted slender convex body.

Consider the effect of the entropy layer on the outer region. The quantity of fluid which has passed through region I is

$$\frac{\psi_s}{\rho_\infty U_\infty \ell^{1+j}} = \psi_s^{1+j} \sim O\left(\delta^{\frac{k(1+j)}{2(k-1)}}\right) = O\left(\delta^{\frac{1}{\alpha}\left(\frac{1}{2}-j\right)}\right) \quad (3.34$$

where α is defined in Eq. 3.33d. Sufficiently far downstream of I, $p/\rho_\infty U^2 \sim O(1)$ as $\delta \to 0$ in the shock layer. From Eq. 3.1d and since $\rho/\rho_\infty \sim O(1)$ and $p/\rho_\infty U^2 \sim O(\delta)$ in I, then in III :

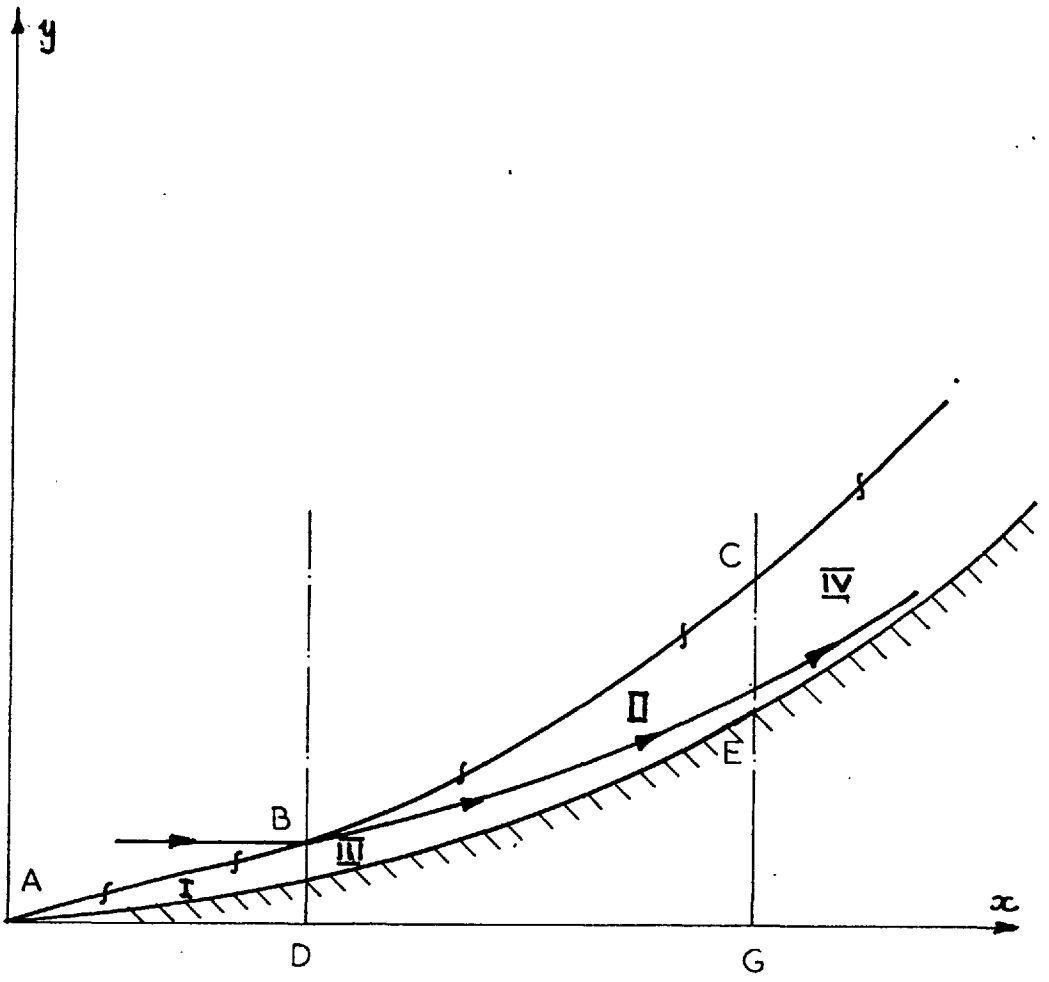


FIG.3.1 : REGIONS OF FLOW ON POWER LAW BODY.

$$\rho/\rho_\infty \sim O(\delta^{-1/\gamma}) \qquad (3.35$$

In the outer region $\rho/\rho_\infty \sim O(1)$ as $\delta \to 0$.

By continuity and from Eq. 3.34, the quantity of fluid in III is $\psi \sim O(\delta^{1/\gamma(1/\alpha-1)})$. Hence, if the velocity along the layer remains O(1), the thickness of the layer must be

$$T_{III} \sim O(\delta^{1/\alpha\gamma}) \qquad (3.36$$

The quantity $1/\alpha\gamma$ is plotted against k in Fig. 3.2. For $k>1$, $1/\alpha\gamma > \frac{2+\gamma(1+j)}{2\gamma}$. Hence in the slender section, the first order inner boundary on the outer region is

$$v_{II} = U_\infty \frac{dy_b}{dx} + O(\delta^{1/\alpha\gamma}) \qquad (3.37$$

that is, the low-entropy layer displaces the outer region by an amount $O(\delta^{1/\alpha\gamma})$. Therefore the similar solutions are the correct first order approximation to the field in the region II on a power law body. Further the error imposed by the low-entropy layer is always of higher order than that imposed by the strong shock approximation. The latter remark also applies when $\sigma \sim O(\delta^\beta)$. Then, $T_{III} \sim O(\delta^{1/\alpha\gamma-2\beta})$ and the error in the strong shock approximation is $O(\delta^\gamma)$.

To construct the equations of the low-entropy layer the usual boundary layer type co-ordinates are introduced. In this system, which is orthogonal curvilinear, a point is specified by its distance n along a normal from the body surface, and the arc length s along the body measured from some suitable reference

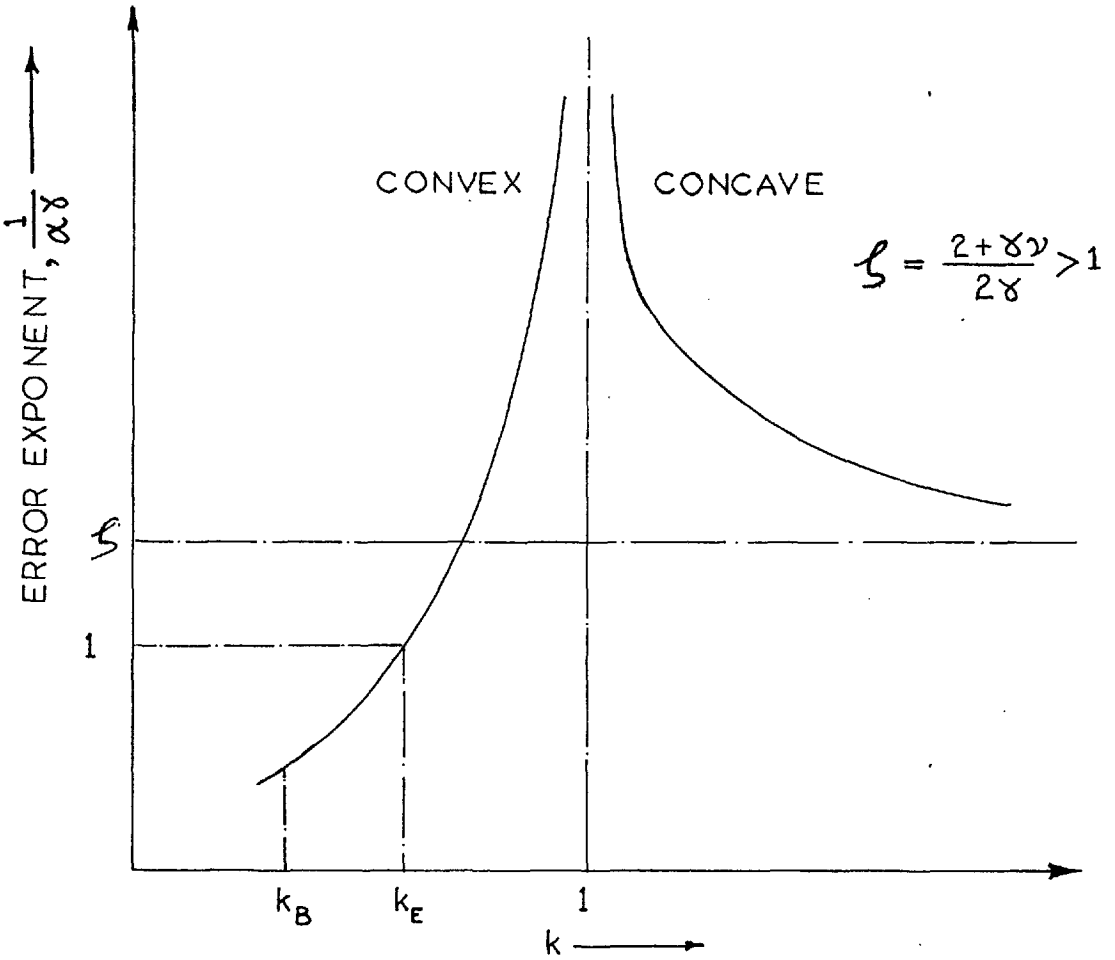


FIG. 3.2 : ENTROPY LAYER ERROR EXPONENT.

point. If $\tilde{u}$ and $\tilde{v}$ are the components of velocity in the s and n directions respectively, then the Eqs. 3.1 assume the form :

$$\frac{\partial}{\partial s}\left(\rho \tilde{u} y^{j}\right) + \frac{\partial}{\partial n}\left(\rho \tilde{v} y^{j}\{1 + n/R\}\right) = 0 \qquad (3.38a$$

$$\frac{R\tilde{u}}{R+n}\frac{\partial \tilde{u}}{\partial s} + \tilde{v}\frac{\partial \tilde{u}}{\partial n} + \frac{\tilde{u}\tilde{v}}{R+n} + \frac{1}{\rho}\frac{R}{R+n}\frac{\partial p}{\partial s} = 0 \qquad (3.38b$$

$$\frac{R\tilde{u}}{R+n}\frac{\partial \tilde{v}}{\partial s} + \tilde{v}\frac{\partial \tilde{v}}{\partial n} - \frac{\tilde{u}^{2}}{R+n} + \frac{1}{\rho}\frac{\partial p}{\partial n} = 0 \qquad (3.38c$$

$$\frac{R\tilde{u}}{R+n}\frac{\partial}{\partial s}\left(p/\rho^{\gamma}\right) + \tilde{v}\frac{\partial}{\partial n}\left(p/\rho^{\gamma}\right) = 0 \qquad (3.38d$$

where $\mathcal{R}$ is the radius of curvature of the body profile :

$$\mathcal{R} = \frac{\left\{1 + \left(dy_{b}/dx\right)^{2}\right\}^{3/2}}{d^{2}y_{b}/dx^{2}} \qquad (3.39$$

In III, $n/\ell \sim O(\delta^{1/\alpha\gamma})$. Hence since $\tilde{u}/U_{\infty}$ $O(1)$, if continuity is to be non-trivial, $\tilde{v}/U_{\infty} \sim O(\delta^{1/\alpha\gamma})$. This suggests the introduction of the reduced variables :

$$\begin{aligned} p/\rho_{\infty}U_{\infty}^{2} &= p' \quad , \quad \rho/\rho_{\infty} = \delta^{-1/\alpha}\rho' \\ \tilde{v}/U_{\infty} &= \delta^{1/\alpha\gamma}\tilde{v}' \quad , \quad \tilde{u}/U_{\infty} = \tilde{u}' \end{aligned} \qquad (3.40$$

$$s/\ell = s' \quad , \quad n/\ell = \delta^{1/\alpha\gamma} n' \qquad \text{(3.40 (cont.)}$$

Introducing these reduced quantities into Eqs. 3.17 and retaining lowest order terms, it is found that :

$$-\frac{\partial}{\partial s'}\left(\rho' \tilde{u}' y_b'^{j}\right) + \frac{\partial}{\partial n'}\left(\rho' \tilde{v}' y_b'^{j}\right) = O\left(\delta^{1/\alpha\gamma}\right) \qquad \text{(3.41a}$$

$$\tilde{u}' \frac{\partial \tilde{u}'}{\partial s'} + \tilde{v}' \frac{\partial \tilde{u}'}{\partial n'} = O\left(\delta^{1/\gamma}\right) \qquad \text{(3.41b}$$

$$\frac{\partial p'}{\partial n'} = O\left(\delta^{\frac{1}{\gamma}\left(\frac{1}{\alpha}-1\right)}\right) \qquad \text{(3.41c}$$

$$\tilde{u}' \frac{\partial}{\partial s'}\left(p'/\rho'^{\gamma}\right) + \tilde{v}' \frac{\partial}{\partial n'}\left(p'/\rho'^{\gamma}\right) = O\left(\delta^{1/\alpha\gamma}\right) \qquad \text{(3.41d}$$

Eq. 3.20b asserts that $\tilde{u}' = \tilde{u}'(\psi')$, where $\psi' \sim O(1)$. Since in the slender section ($\tilde{s} \to 0$) $q = (u^2 + v^2)^{1/2} = U_\infty + O(\delta)$ then

$$\tilde{u}(s,n) = U_\infty + O\left(\delta^{1/\gamma}\right) \qquad \text{(3.42}$$

Eq. 3.20c asserts that the pressure is constant along normals to the body surface in the entropy layer and equal to its value at the body, Since, in the limit $\delta \to 0$, the entropy layer becomes vanishingly thin, the inner boundary of the outer region

co-incides with the body. Hence

$$p_b' = p'(s', n') = p'(s', \infty) = p'(s, 0) \qquad (3.43$$

The error term in Eq 3.20c is contributed entirely by the curvature term in Eq 3.17c. The convective terms contribute an error which is $O(\delta^{\frac{1}{2}(\frac{2}{\alpha}-1)})$.

The density distribution in the entropy layer, written in the physical variables is

$$\frac{\rho}{\rho_\infty}(\psi) = \frac{\left\{p_b/\rho_\infty U^2\right\}^{1/\gamma}}{\left\{\left\langle\frac{\delta}{\gamma} + \frac{2}{\gamma+1}\left(\sigma^2(\psi) - \delta\right)\right\rangle^{\frac{1}{2}}\left\langle\frac{\gamma-1}{\gamma+1} + \frac{2}{(\gamma+1)\sigma^2(\psi)}\right\rangle\right\}} \qquad (3.44$$

and the streamline distribution is given by

$$n(\psi) = \frac{1}{y_b' U}\int_0^{\psi} \frac{d\psi_0}{f(\psi_0)} \qquad (3.45$$

Since $\sigma(\psi)$ is only given in a solution for region I, it is not given explicitly here. However, since $\sigma(0) = \delta^{\frac{1}{2}}$, the surface density is given by

$$\frac{\rho_b}{\rho_\infty} = \left\{\gamma \frac{p_b}{\rho_\infty U^2} M_\infty^2\right\}^{1/\gamma} \qquad (3.46$$

Hence $\rho_b/\rho_\infty \to \infty$ as $M_\infty \to \infty$.

The above analysis shows that the similar solutions predict the correct first order pressure on the power law body. Eq. 3.46 suggests that they may be regarded as exact solutions to

the hypersonic small disturbance equations at $M_\infty = \infty$.

It is interesting to compare the properties of the low-entropy layer with those of the conventional layer. Both have constant pressure across the layer, but in other respects they have different properties. The low-entropy layer is cold and dense and the velocity along the layer is almost constant throughout it. The entropy layer is hot and at low density, and the velocity along it varies rapidly across it. It is also possible for the displacement effect of the entropy layer to impose a lower order on the solution in the outer region than that imposed by the strong shock approximation. Freeman (1962) has shown that the displacement effect of the entropy layer on a power law convex body ($k < 1$) is $O(\delta^{-1/\alpha\gamma})$ where $\alpha < 0$. For $k < k_E$ in Fig. 3.2, $-1/\alpha\gamma < 1$.

Although the analysis given above has considered only the cusped body, it can be extended to a body having finite ϑ_L provided that $\vartheta_L \sim O(\delta^{1/2})$.

4) Application of the Similar Solutions to Concave Surfaces.

4.1) Integration of the equations.

Eqs. 3.29 are invariant under the change of variable

$$\lambda = \Omega \varphi \tag{4.1}$$

where Ω is a constant. φ is replaced by λ as the independent variable. Ω is chosen such that $\lambda = 1$ at the shock. As the problem is now formulated, the body condition is specified at a point which is itself part of the solution to the problem. Now since V_b and V_s are functions of γ and k only, this difficulty is removed if V is chosen as independent variable. Let

$$V = \xi + k \,, \quad \xi_b = 0 \tag{4.2}$$

Also, put

$$z = \frac{\gamma P}{R} \,, \quad \mu = \ln R \,, \quad \eta = \ln \lambda \tag{4.3}$$

Here z is the non-dimensional speed of sound.

After some algebra, the following equations are obtained:

$$\frac{dz}{d\xi} = \frac{z}{\xi} \frac{\{A\xi^3 + B\xi^2 + C\xi - 2z(\xi + D)\}}{\{\xi^3 + E\xi^2 + F\xi - z((1+j)\xi + G)\}} \tag{4.4a}$$

$$= \frac{z}{\xi} \frac{\Psi(z, \xi)}{\Phi(z, \xi)} \tag{4.4b}$$

$$\frac{d\eta}{d\xi} = \frac{z - \xi^2}{\Phi} \qquad (4.4c$$

$$\xi \frac{du}{d\xi} = -\left\{ (1+j)(\xi + k) \frac{d\eta}{d\xi} + 1 \right\} \qquad (4.4d$$

where

$$A = 2 + j(\gamma - 1) \quad , \quad B = (k-1)(3-\gamma) + j(\gamma-1)k$$

$$C = k(k-1)(1-\gamma) \quad , \quad D = (k-1)/\gamma$$

$$E = 2k - 1 \quad , \quad F = -k(k-1)$$

$$G = 2(k-1)/\gamma + (j+1)k$$

The equation for z is decoupled from those for η and u. Hence Eq. 4.4a may be solved independendtly, and Eqs. 4.4b and 4.4c are reduced to quadratures. This, in principle, is a simplification. Eqs. 4.4 are modified forms of the equations of self similar flow given by Sedov (1959, p.155) and Hayes and Probstein (1959, p.55).

There are nine singularities of Eq. 4.4a, but when $k > 1$ only one is of interest.

In Eq. 4.4a, assume that $z/\xi \to \infty$ as $\xi \to 0$. Then, as $\xi \to 0$:

$$\frac{dz}{d\xi} \longrightarrow \frac{z}{\xi}\,\frac{2D}{G} \tag{4.5}$$

where $2D/G = \alpha$ is the quantity defined in Eq. 3.33d.

Hence by Eq. 4.5

$$z \simeq z_0 \xi^{\alpha} + \cdots \tag{4.6}$$

which is consistent with Eq. 3.26. z_0 is the constant of integration. Now

$$\frac{2}{2+\gamma(1+j)} \geq \alpha \geq 0 \;;\; \infty \geq k \geq 1 \tag{4.7}$$

Hence $z \to 0$ as $\xi \to 0$, but $dz/d\xi \to \infty$ as $\xi \to 0$

The point $\xi = 0$ is a node.

At the shock wave

$$z_s = \varepsilon(1+\varepsilon)k^2, \quad \xi_s = -\varepsilon k \tag{4.8}$$

so that this is an ordinary point of Eq. 4.4.

The integral curves in the $z - \xi$ plane are depicted in Fig. 4.2. Numerical integration procedures are required to obtain solutions to Eq. 4.4a. The method is to integrate from the shock wave point towards the origin. But since the origin is a node, numerical methods will become unstable as it is approached. Therefore it is necessary to change to a series solution at some point ξ_m before this occurs. Since an infinity of integral curves pass through the origin, the required path to the origin is determined by matching the series solution (by choosing z_0) to the value of

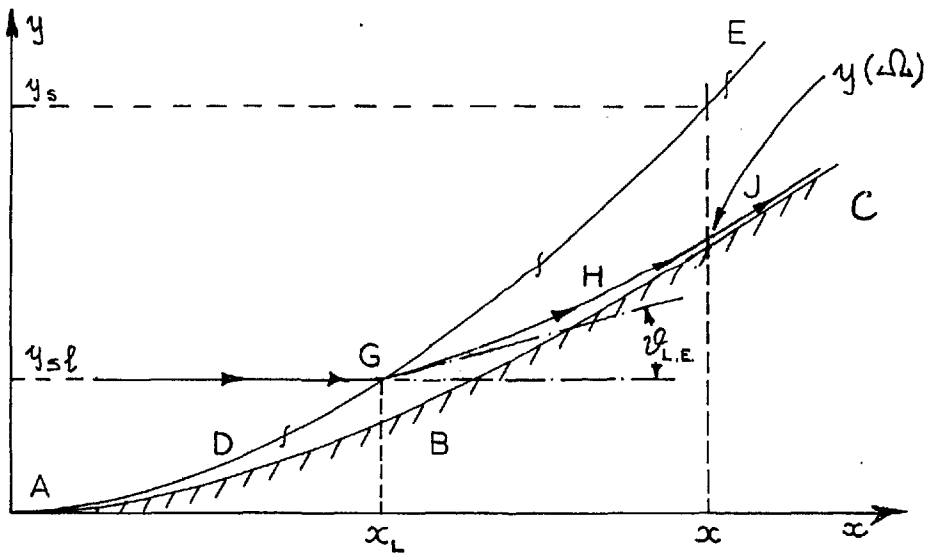


FIG.4.1 : THE CLASS OF NON-SELF-SIMILAR SURFACES.

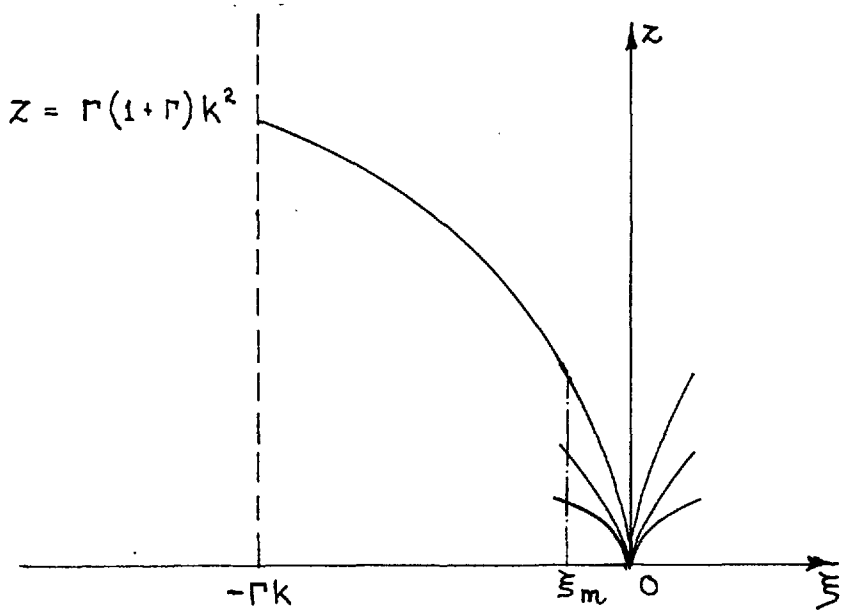


FIG. 4.2: THE $\xi - Z$ PLANE.

z at ξ_m obtained by numerical integration up to the match point.

The equations were integrated on the University of London digital electronic computer using a fourth order Runge-Kutta variable step length method. The error of computation at the body was less than 0.2% (see Appendix 2). The series solutions for z, η and μ to third order in ξ are given in Appendix 2.

4.2) Derivation of Non Self Similar Surfaces.

By constructing the equations for the streamlines in the field, the solutions for similar surfaces may be extended to a certain class of surfaces which have non-zero leading edge angles. Although only the case $k > 1$ will be considered here, the procedure to be given below applies to convex surfaces for which $k < 1$. This technique has not been exploited in the literature.

Fig. 4.1 depicts the field for a self-similar flow when $k > 1$. The curve ABC is the body and ADGE is the shock. The shape of a streamline ψ = constant not passing through the origin is depicted by GHJ. In the hypersonic flow, GHJ may be replaced by a surface of the same shape.

If x_L is the value of x for which the derived surface has the required leading edge angle, then

$$\vartheta_L = (1-\varepsilon)\sigma = \frac{(1-\varepsilon)}{\lambda_b} D k x_L^{k-1} \qquad (4.9$$

This expression is obtained from Eq. 2.14 by letting $M_\infty \to \infty$; the shock shape is given by $y_s = D/\lambda_0 x^k$. By continuity,

$$\frac{\rho_\infty U_\infty}{1+j}\left\{ y_{sL}^{1+j} - y_s^{1+j} \right\} = \int_{y_s}^{y} \rho U_\infty y_0^j \, dy_0 \qquad (4.10$$

This equation may be non-dimensionalized to give

$$\tilde{\Psi} \equiv \frac{1}{1+j}\left\{ \left(\frac{x_L}{x}\right)^{1+j} - 1 \right\} = \int_{\lambda_s=1}^{\lambda} R(\lambda_0)\lambda_0^j \, d\lambda_0 \qquad (4.11$$

$\tilde{\Psi}$ is a non-dimensional stream function. Eq. 4.11 can be written as

$$d\tilde{\Psi}/d\xi = \left\{ \exp\left(\mu(\xi) + (1+j)\eta(\xi) \right) \right\} \cdot \left\{ \frac{z(\xi) - \xi^2}{\Phi(\xi)} \right\} d\xi \qquad (4.12$$

where $\tilde{\Psi}_b = \tilde{\Psi}(0) = -1/(1+j)$

Since $\tilde{\Psi}$ is a function of ξ only, it may be evaluated simultaneously with Eqs. 4.4.

To construct a non-similar surface, the following procedure is adopted:

(i) Given γ , k , D and ρ_L ; x_L is determined from Eq. 4.9

(ii) Given an x , $\tilde{\Psi}$ is determined from Eq. 4.11.

(iii) The values of V, R, P and λ corresponding to $\tilde{\Psi}$ are obtained from the tabulated solution.

(iv) The ordinate of the surface is given by

$$y = \frac{\lambda}{\lambda_b} D x^k \qquad (4.15$$

(v) The slope is

$$\vartheta = \frac{v}{U_\infty} = \frac{V y}{x} \qquad (4.16$$

(vi) The pressure is

$$p = \rho_\infty U_\infty^2 y^2/x^2 \, P(\tilde{\Psi}) \qquad (4.17$$

Since the streamline chosen to be the non-similar surface does not pass through the origin, then for M_∞ sufficiently large, the solution is valid at the leading edge and near the surface of the derived body. When $k < 1$, the derived surface also has a sharp leading edge. If $x_\perp$ is sufficiently far from the origin it then satisfies the equivalence principle at the leading edge.

4.3) Results and Comments.

The values of V, R, P and $\tilde{\Psi}$ for certain values of k and γ in the ranges $1.5 \leq k \leq 6.0$ and $1.15 \leq \gamma \leq 1.67$ for $j = 0$ are tabulated in Appendix 3. The distribution of Z, R and P within the shock layer for $k = 4.0$ and $\gamma = 1.4$ are given in Fig. 4.3.

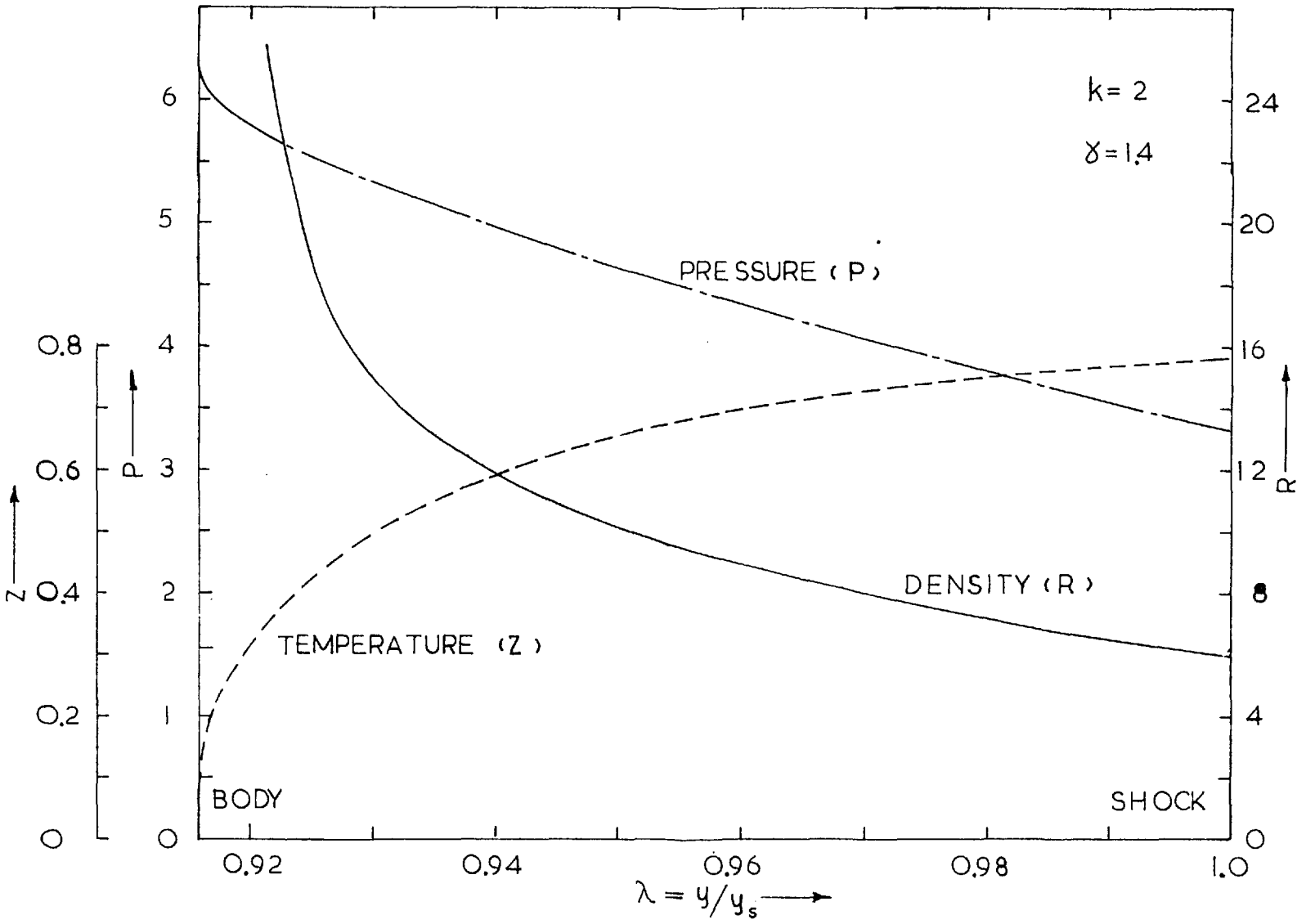


FIG.4.3 : DISTRIBUTION OF PROPERTIES IN THE SHOCK LAYER ON A POWER LAW BODY.

In Fig. 4.4, the quantity

$$\frac{p_b}{\rho_\infty U_\infty^2 \vartheta_b^2} = P_b^*/k^2 \qquad (4.22$$

is plotted against k for $\gamma = 1.4$ and $j = 0$. The other curves are the tangent wedge estimate for $M_\infty = \infty$ (Eqs. 2.14 and 2.15), the Newtonian (Eq. 2.18) and the Newtonian plus Centrifugal (Eq. 2.5) theories. The Newtonian plus Centrifugal estimate agrees moderately well with the similar solution, except near $k = 1$.

As $M_\infty \to \infty$, the simple wave estimate (Eq. 2.17) for a cusped body becomes

$$\frac{p_b}{\rho_\infty U^2 \vartheta_b^2} \simeq \frac{\gamma-1}{2} (M_\infty \vartheta_b)^{2/\gamma-1} \qquad (4.23$$

Hence $p_b \to \infty$ as $M_\infty \to \infty$. In Fig. 4.5, P_b/k^2 is plotted against γ for $k = 4$, and is compared with the approximate estimates used in Fig. 4.4. The similar solution depends only weakly on γ and tends to the estimate given by Newtonian plus Centrifugal theory as $\gamma \to 1$.

The results for $\gamma = 1.4$ and $k = 4$ have been used to construct a solution for a non-similar surface and to estimate the pressure distribution on it. The loading edge angle $\vartheta_L = 10°$. The shape of the surface and the pressure distribution on it are given in Fig. 4.6. The simple wave theory can be applied to this shape at $M_\infty = \infty$, since the leading edge angle is finite; and

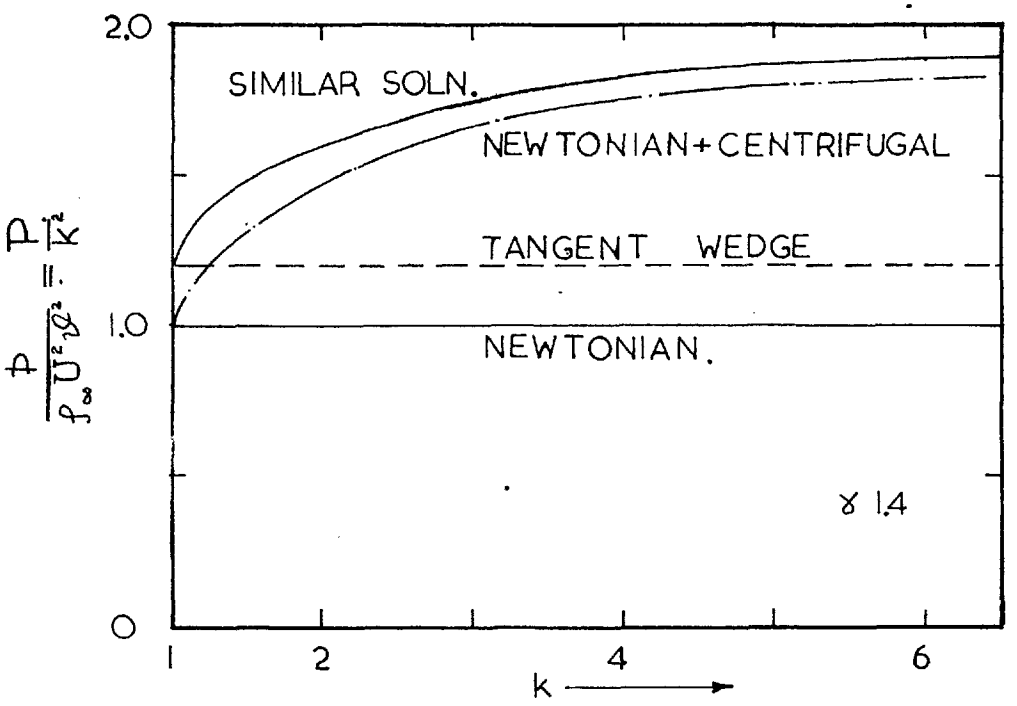


FIG.4.4 : EFFECT OF k ON SIMILAR SOLUTIONS.

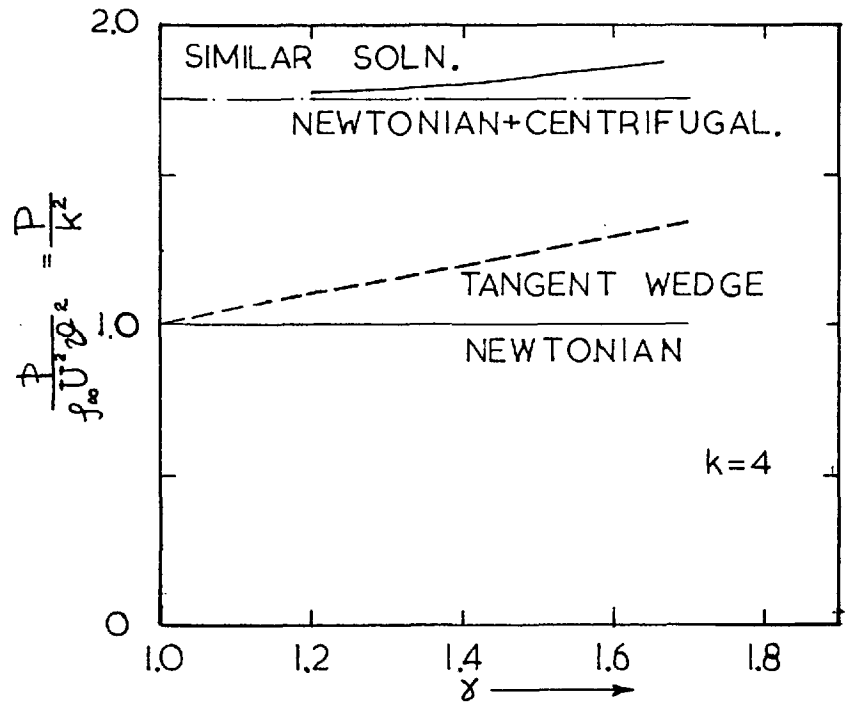


FIG 4.5 : EFFECT OF γ ON SIMILAR SOLUTIONS.

this and the tangent wedge estimate are included in Fig. 4.6.* The simple wave theory overestimates the surface pressure , particularly towards the rear of the body. The tangent wedge theory underestimates it. This example shows that the reflected waves generated in an underfocussed flow can be very strong, particularly when M_∞ is very high.

The relatively good agreement between the estimates of surface pressure given by the similar solutions and the Newtonian plus Centrifugal theory occurs because the shock layer generated on a concave surface is thin. Hence, if the flow is underfocussed, and if the shape of the surface can be expressed as an analytic function, then the methods described in § 2.1 will be useful.

The similar solutions may be used to indicate the effect of discontinuity in profile curvature on the surface pressure distribution. Consider a power law body which is continued as a ramp for $x \geqslant x_R$ (i.e. at constant slope, $\vartheta = \vartheta_R$). The similar solutions will give the most accurate estimate of surface pressure at the beginning of the ramp. Sufficiently far downstream on the ramp, the pressure tends to the tangent wedge value. Hence the fall-off in pressure will be the difference between these two:

---

* A Newtonian plus Centrifugal estimate was not readily available, since the body shape is in tabular form.

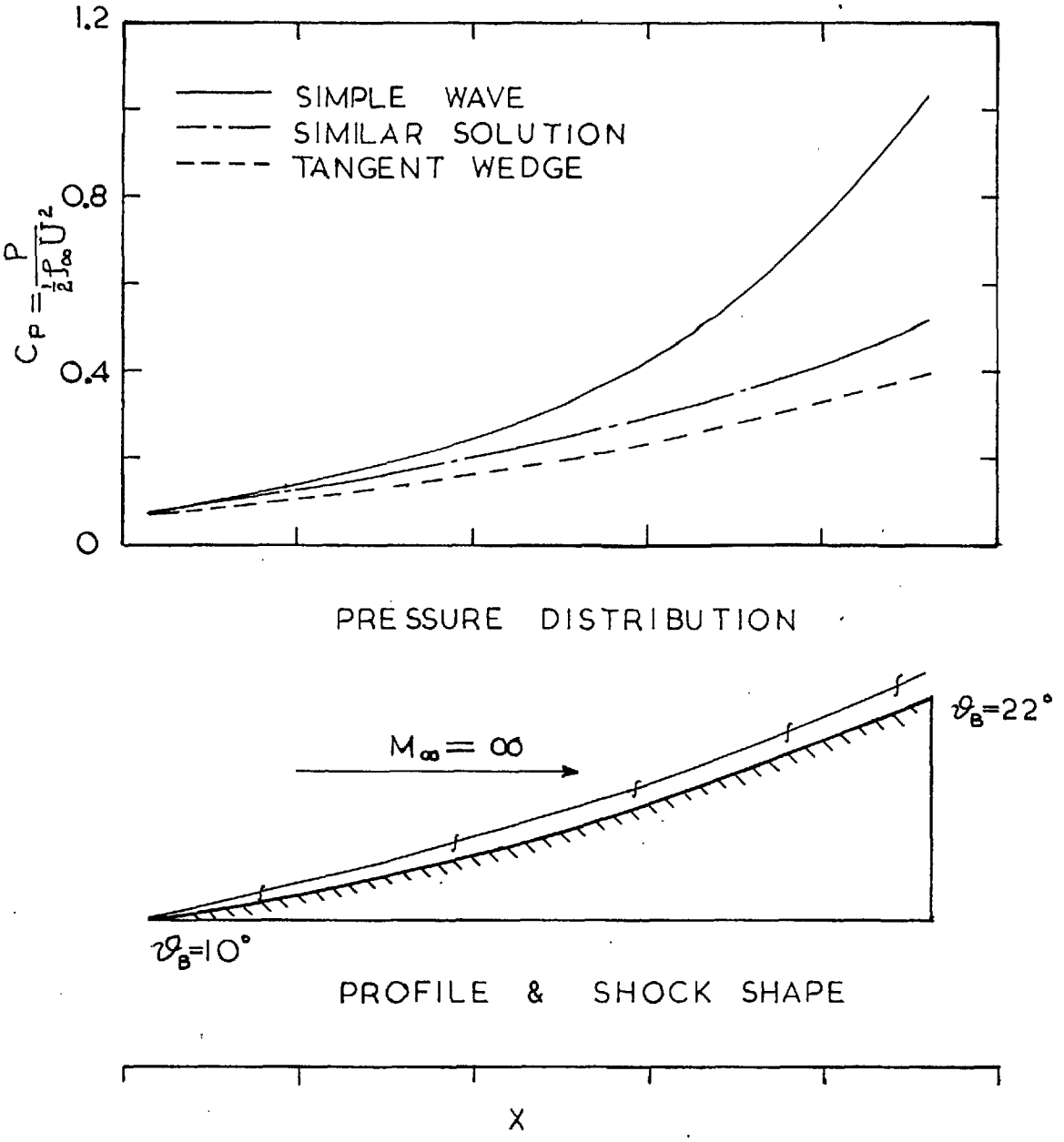


FIG. 4.6 : PRESSURE DISTRIBUTION ON A NON — SIMILAR SURFACE

$$\Delta p = \rho_\infty U_\infty^2 \vartheta_R^2 \left\{ P_b/p^2 - \frac{\gamma+1}{2} \right\} \qquad (4.24$$

Figs. 4.4 and 4.5 show that there will be a significant fall-off in pressure along the ramp. The approximate methods described in this thesis cannot describe the flow in this region.

5) On Overfocussed Flows.

5.1) Wave Structure of the Idealised Flows.

The wave structure of the idealised flows introduced in § 1.4 will be described briefly. A detailed discussion of the interaction process is given by Courant and Freidrichs (1948, p.343).

5.11) Double Wedge Flow. Referring to Fig. 5.1, the shock waves generated at A and B by sucessive wedges of angles ϕ_1 and ϕ_2, respectively, intersect at C. Downstream of C, a third shock wave CD belonging to the same family as AC and BC, a slipline CE, and a centred reflected wave CFG are generated. At hypersonic speeds CFG is an expansion (Bird, 1963). Across the slipline CE there are discontinuities in density, temperature and entropy. The pressure and the streamline inclination are continuous across it.

The interaction can be visualised on a wave polar diagram in which the pressure p and the streamline inclination θ are the co-ordinates. The diagram is given in Fig. 5.3. The curve ADBC is the locus of all the points attainable from the free stream conditions by a single shock deflection. The point D, given by $\theta = \phi_1$ denotes conditions behind the first shock AC in Fig. 5.1. The curve DHF is the locus of the points accessible by a single oblique shock wave with the conditions in region (1) of Fig. 5.3 as initial conditions. H, given by $\theta = \phi_1 + \phi_2 = \phi_x$, corresponds to conditions in region (2), just downstream of the second shock. The curve GHKJ is the locus of points attainable from conditions in (2)

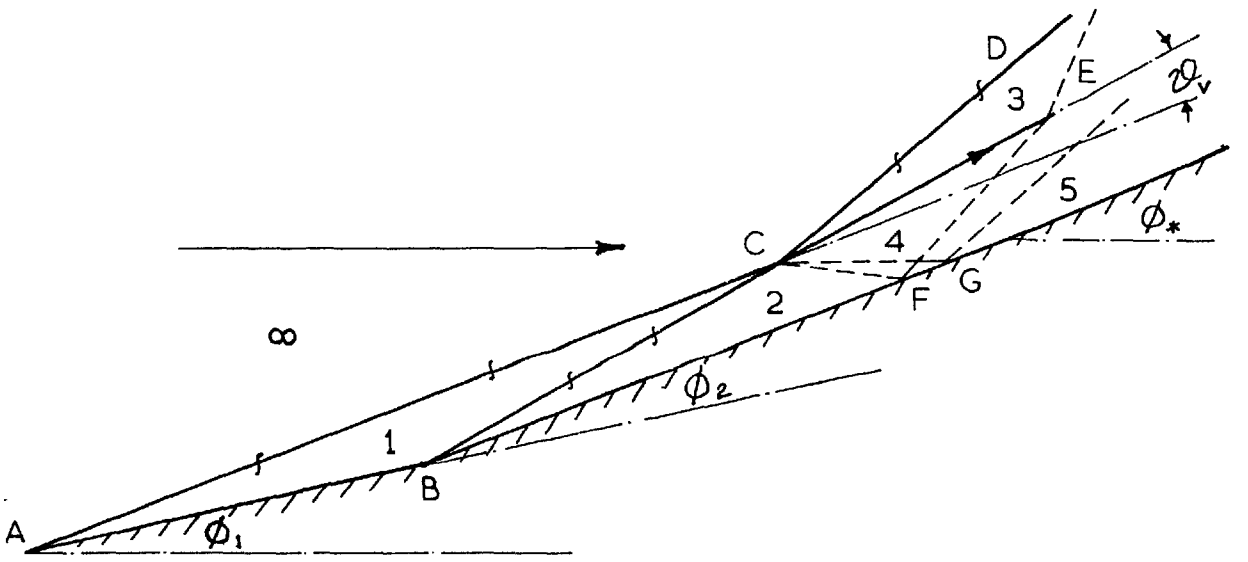


FIG. 5.1 : HYPERSONIC FLOW OVER A DOUBLE WEDGE

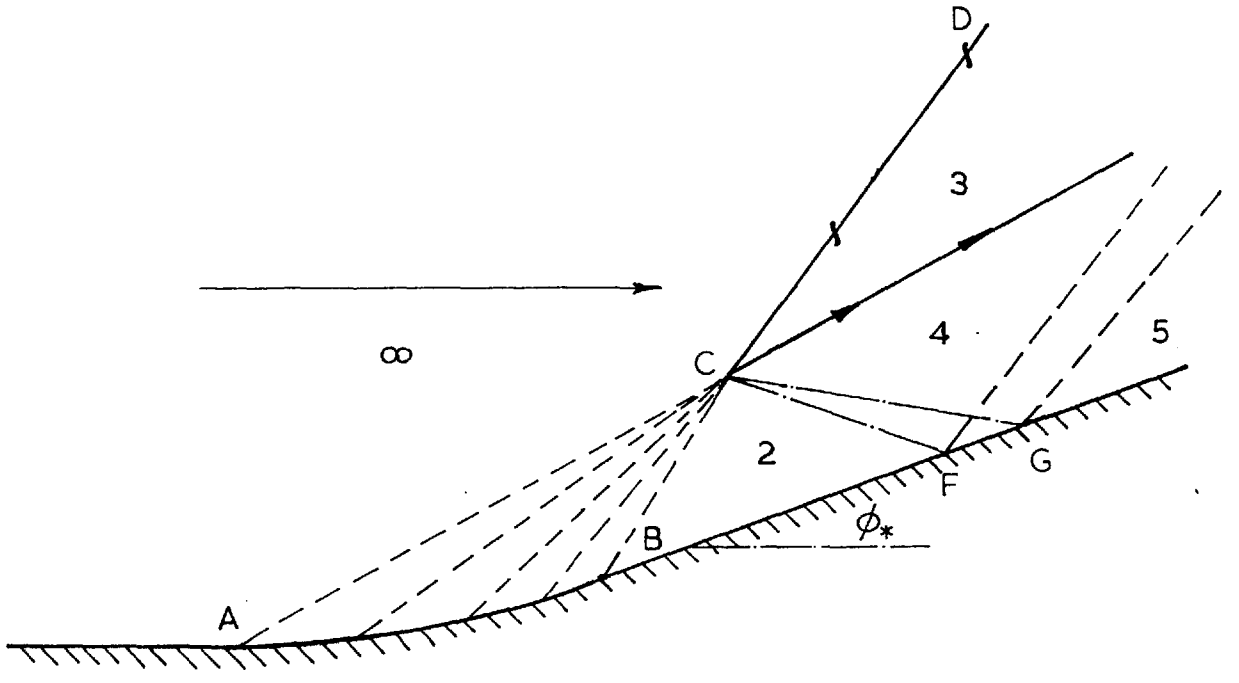


FIG. 5.2 : CENTRED COMPRESSION AND SHOCK .

by a simple wave. The pressure and deflection produced by the shock CD in region (3) of Fig. 5.1 lie on the polar ABC. Since the pressure and the deflection ($\vartheta_v + \phi_*$) is the same both sides of the slipline CE, the point K gives the conditions just downstream of the interaction.

The equations describing this system are

(i) across the oblique shock CD :

$$p_3/p_\infty = (1+\varepsilon)\, M_\infty^2 \sin^2\sigma_3 - \varepsilon \qquad (5.1$$

$$\cot(\phi_* + \vartheta_v) = \tan\sigma_3 \left\{ \frac{M_\infty^2}{(1-\varepsilon)(M_\infty^2 \sin^2\sigma_3 - 1)} - 1 \right\}, \qquad (5.2$$

(ii) across the expansion wave CFG :

$$\frac{p_4}{p_2} = \left\{ \frac{1 + \frac{\varepsilon}{1-\varepsilon} M_2^2}{1 + \frac{\varepsilon}{1-\varepsilon} M_4^2} \right\}^{\frac{1+\varepsilon}{2\varepsilon}}, \qquad (5.3$$

$$\vartheta_v = \nu_4 - \nu_2 \qquad (5.4$$

$$\nu_i = \varepsilon^{-\frac{1}{2}} \arctan\left(\varepsilon(M_i^2 - 1)\right)^{\frac{1}{2}} - \arctan\left(M_i^2 - 1\right)^{\frac{1}{2}}$$

(iii) across the slipline CE :

$$p_3 = p_4 \qquad (5.5$$

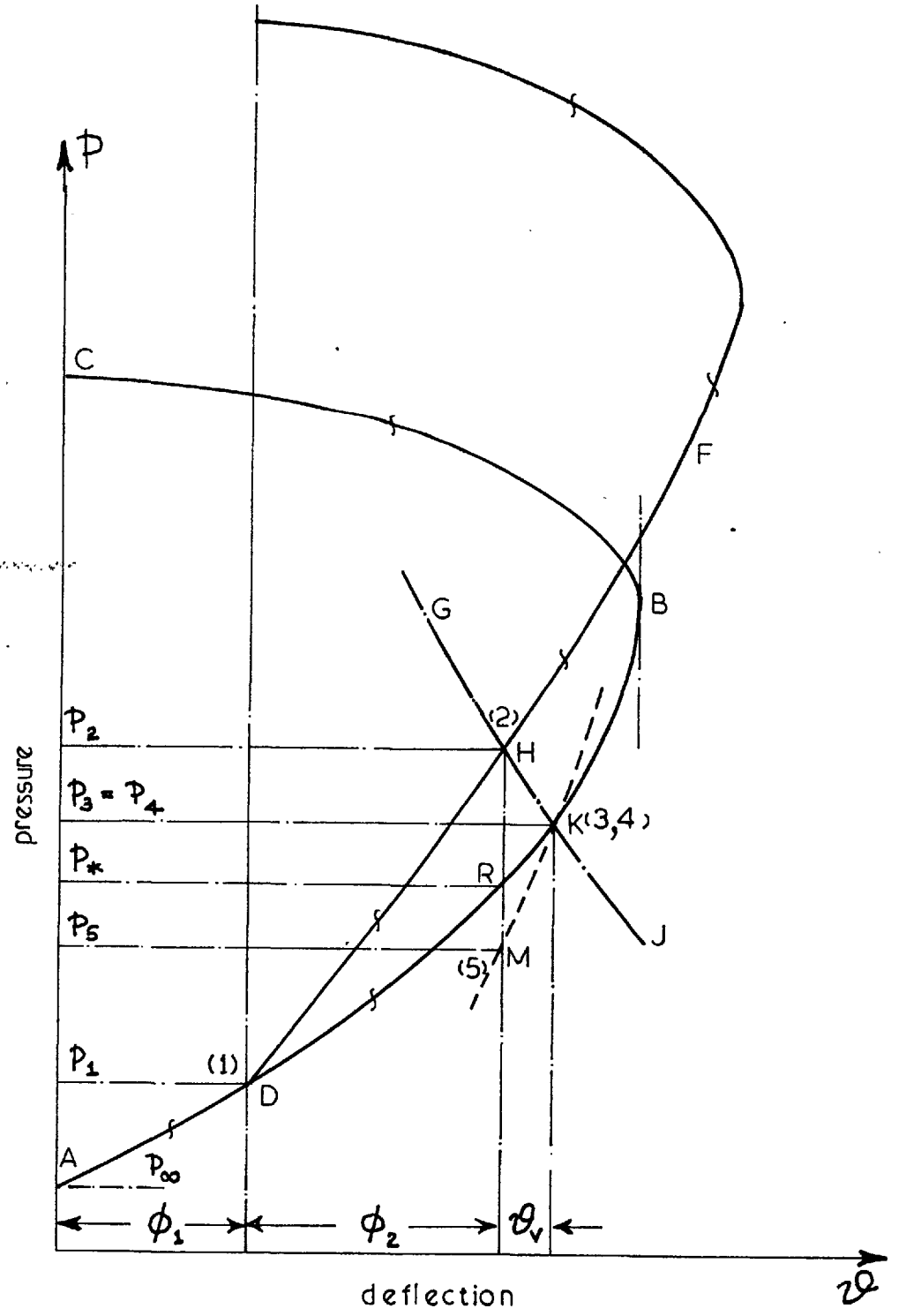


FIG. 5.3 : POLAR DIAGRAM FOR THE DOUBLE WEDGE FLOW.

The subscripts denote the constant-property regions so marked in Fig. 5.1. M_2 and p_2 are assumed known.

Downstream of the interaction the expansion wave CFG impinges on the second wedge. A principal wave FGE is generated, and this wave intersects the slipline and is partly reflected and partly transmitted. The transmitted wave intersects the outer shock CD and curves it. Downstream of this point the wave structure becomes complex, but the pressure in the field tends to that generated by a single wedge of angle $\phi_* = (\phi_1 + \phi_2)$, (point R in Fig. 5.3).

It is possible to find a streamline which is deflected only by simple isentropic waves in passing from region (2) to region (5) in Fig. 5.1. Therefore the pressure in region (5) can be obtained by the use of simple wave relations. Since the deflection of a streamline which goes from (4) to (5) in Fig 5.1 is $(-\theta_v)$, the pressure is given by the point M in Fig. 5.3.

5.12) Centered Compression and Shock Wave: The pressure in region (2), Fig. 5.2 is generated by the compression wave AB, centered at C. The wave pattern downstream of C is the same as for the double wedge flow.

Since Eqs. 5.1 to 5.5 balance the change in pressure and deflection through the third shock CD and the expansion fan CFG without reference to the method by which the pressure in region (2) was obtained, they apply to the centered compression flow.

The wave polar diagram is given in Fig. 5.4. The curve AEB is the locus of points attainable by isentropic compression from the free stream conditions. The rest of the polar is the same as for the double wedge flow.

Johannesen (1952), by using Busemann's third order simple wave theory, which is valid for $\phi_* \ll 1$, has shown that the simple wave CFG is a shock wave when

$$\frac{6-2\gamma-2\sqrt{\gamma^2-1}}{5-3\gamma} < M_\infty^2 < \frac{6-2\gamma+2\sqrt{\gamma^2-1}}{5-3\gamma} \qquad (5.6$$

If $\gamma = 1.4$, then the range is

$$1.25 < M_\infty < 2.54$$

Outside this range it is an expansion.

5.2) Solutions to the Interaction Equations

Analytic solutions to Eqs. 5.1 to 5.5 in the limit $\phi_2 \to 0$ have been given by Lighthill (1949) and by Chu (1952). When ϕ_1 and ϕ_2 are finite, solutions in closed form are not available. To obtain solutions a simple iteration procedure can be used. This is summarised below.

(i) Given an approximation ϑ_{v_i} to ϑ_v, calculate σ_3 from Eq. 5.2.

(ii) Given σ_3, calculate p_3/p_∞ from Eq. 5.1.

(iii) From Eq. 5.3 and the condition $p_3 = p_4$ calculate M_4

(iv) From Eq. 5.4 calculate ν_4 and $\vartheta_{v_{i+1}}$

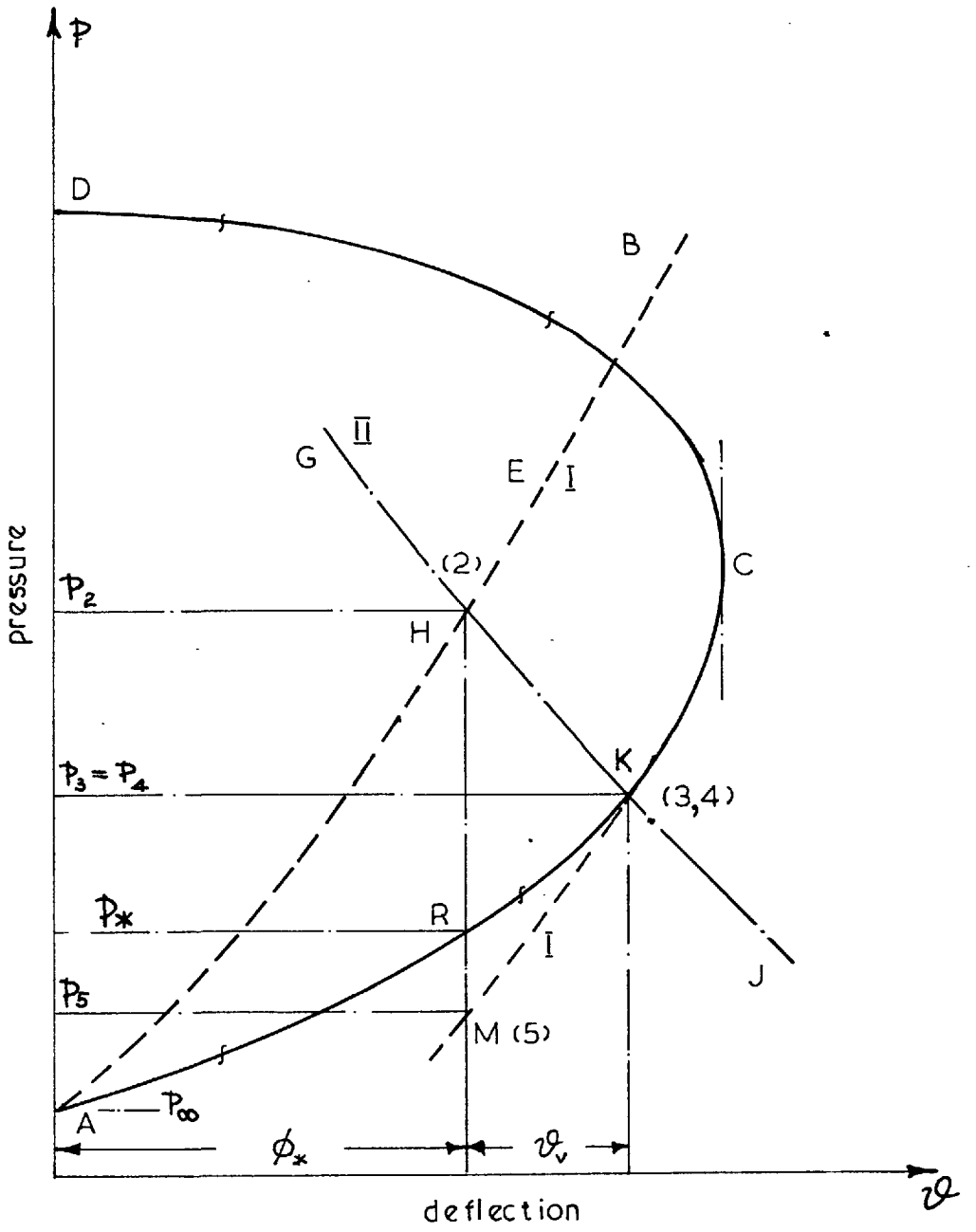


FIG.5.4 : POLAR DIAGRAM FOR CENTRED COMPRESSION AND SHOCK.

In the absence of any other approximation, put $\vartheta_v = 0$ initially.

Eq. 5.2 cannot be solved for σ_3 in terms of ϑ_3 in closed form. Consequently an iteration procedure such as that described by Collar (1959) must be used. If x_i is the i-th approximation to cot σ_3, then Eq. 5.2 can be cast into the form:

$$x_{i+1} = \left\{ A - \frac{B}{x_i + C} \right\}^{1/2} \qquad (5.7$$

where

$$A = M_\infty^2 - 1 \; ; \; B = \left(\frac{M_\infty^4}{1-\varepsilon} \right) \tan \vartheta_3 \; ; \; C = \left(\frac{M_\infty^2}{1-\varepsilon} + 1 \right) \tan \vartheta_3$$

The procedure which is the reverse of that given above is simpler, since ϑ_v is calculated from σ_3 in Eq. 5.2. However the reverse procedure was found to diverge.

5.3) An Exact Solution of The Flow Over a Double Wedge.

A solution of the flow over a double wedge was constructed using the method of characteristics (Ferri, 1955). The interaction equations were solved by using the method described in § 5.2. The values of the parameters are;

$$\varphi_1 = 10^\circ, \quad \varphi_2 = 20^\circ, \; M_\infty = 10, \; \gamma = 1.4$$

The wave pattern is given in Fig. 5.5. The values of the variables in the regions of constant property are marked. The arrows on the Mach lines indicate the sense of the local associated positive-

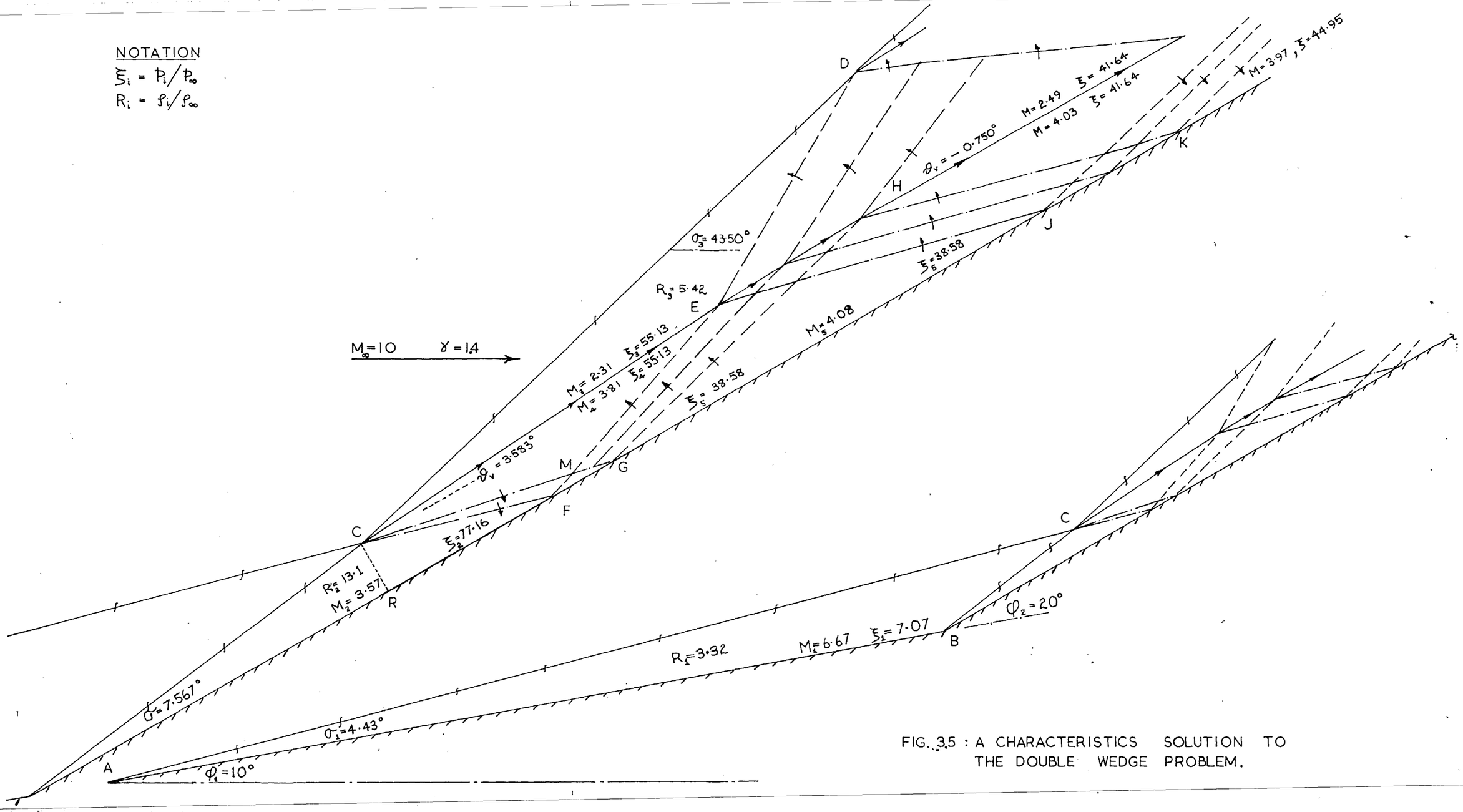


FIG. 3.5 : A CHARACTERISTICS SOLUTION TO THE DOUBLE WEDGE PROBLEM.

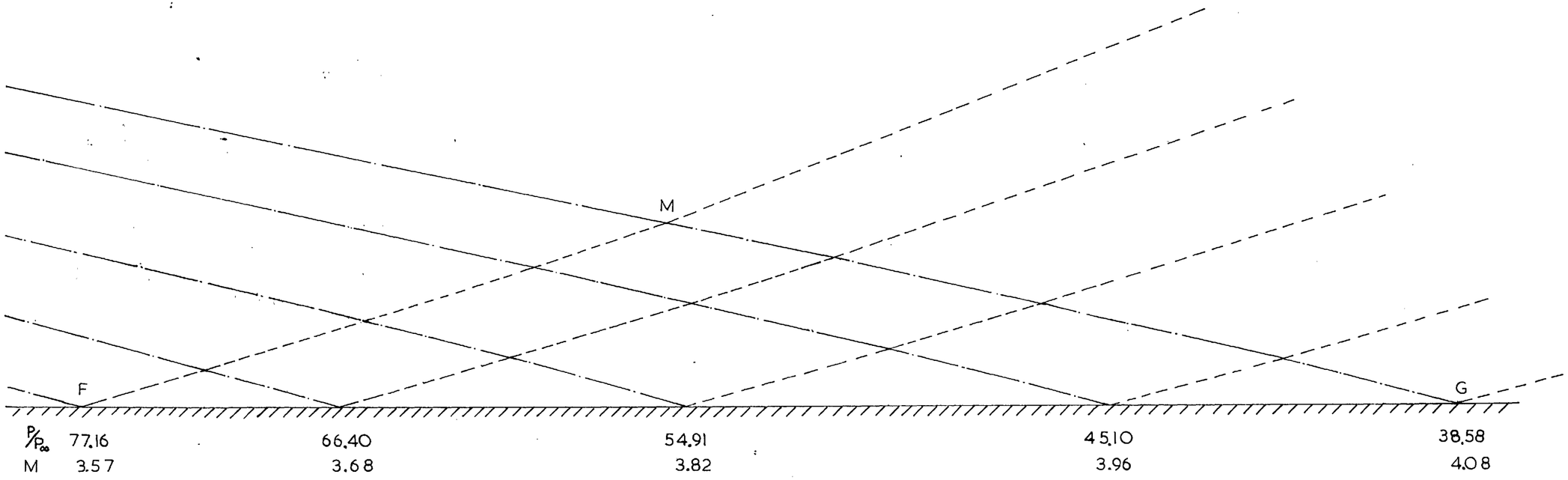


FIG. 3.6 : WAVE STRUCTURE OF THE REGION (CMG)

pressure gradient.

Most of the pressure variation occurs across the region FG. In some regions, the pressure falls below its value far downstream p_*. Downstream of JK the disturbances are relatively weak. There are large discontinuities in Mach number, temperature and density across the slipline CEH. The gas under the slipline is denser, colder, and has a larger Mach number than the gas above it. It corresponds to the low-entropy layer generated on the cusped body, (§ 3). The initial angle of the slipline relative to the second wedge is small when compared with the maximum deflections in the field : thus $\vartheta_v / \phi_* << 1$

Downstream of C the field consists of a series of analytically different regions matched together along characteristics. This shows that flows involving the interaction of two shock waves of the same family or the formation of shocks by compression waves cannot be described by the approximate methods reviewed in § 2. Step-by-step numerical solutions of the full equations would be required.

The wave pattern in the reflection region FMG is given in Fig. 5.6. The Mach number and pressure ratio is marked at each lattice point. A notable feature is that, although there are large changes in pressure throughout the region, the characteristics are nearly straight lines.

The pressure distribution on the second wedge is given

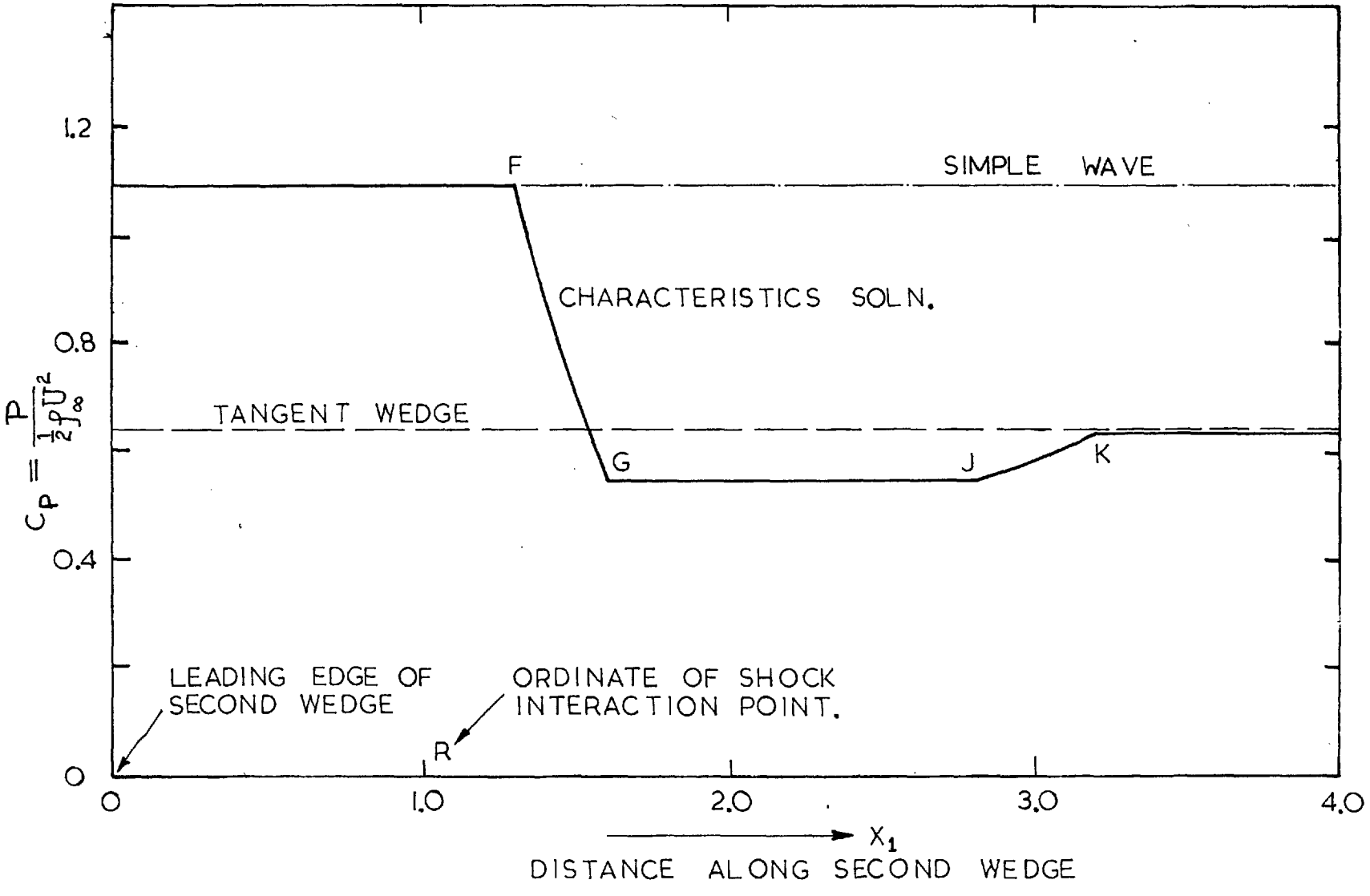


FIG. 5.7: PRESSURE DISTRIBUTION ON SECOND WEDGE

in Fig. 5.7. The simple wave estimate, which gives the correct pressure in region (2), and the tangent wedge estimate are included.

Fig. 5.8 is a Schlieren photograph of the flow at $M_N = 7.5$ over a double wedge ($\phi_1 = 10^\circ$, $\phi_2 = 20^\circ$) taken in the Imperial College Gun Tunnel. The boundary layer formed a small separation bubble in the corner. However, the photograph shows a remarkable qualitative similarity to Fig. 5.5. A similar photograph was taken at $M_N = 10$, but in this case a much larger separation bubble was formed, so that the wave pattern was more complex.

5.4) An Approximate Solution to the Interaction Equations.

If $M_\infty \gg 1$ and $\phi_* \ll 1$, then an approximate solution to Eqs. 5.1 to 5.5 which is valid for finite wave strengths can be obtained.

The quantities p_2/p_∞ and M_2 in the regions (2) in the double wedge and the centred compression flows, and the pressure ratio p_*/p_∞ on the second wedge or ramp far downstream can, consistently with the above assumptions, be calculated using the hypersonic small disturbance equations* (c.f. Eqs. 2.14 to 2.17).

Now the pressure ratio for region (3) in Figs. and 5.2 is, from Eqs. 2.14 to 2.17 :

---

*For certain values of γ and ranges of M_∞, these quantities can be obtained from charts. However, for small ϕ_* and large M_∞ the error involved in reading such charts can be large.

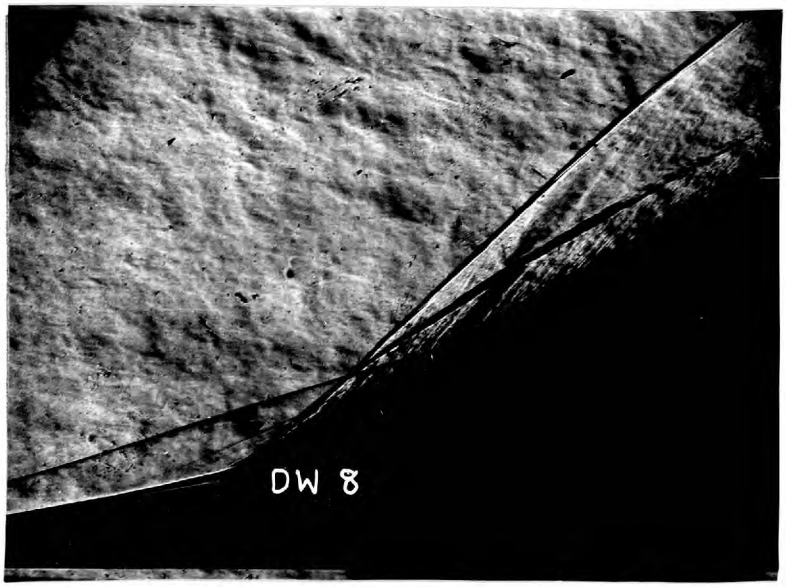


Fig. 5.8, Schlieren photograph of the flow over a double wedge at $M = 7.5$.

$$p_3/p_\infty = (1+\varepsilon) M_\infty^2 \sigma_3^2 - \varepsilon , \qquad (5.8a$$

where

$$M_\infty \sigma_3 = \xi + \sqrt{\xi^2 + 1} \; ; \; \xi = \frac{M_\infty (\phi_* + \vartheta_v)}{2(1-\varepsilon)} \qquad (5.8b$$

The pressure change across CFG (region (2) to region (4)) is

$$p_4/p_2 = \left\{1 - \frac{\varepsilon}{1-\varepsilon} M_2 \vartheta_v\right\}^{\frac{1+\varepsilon}{\varepsilon}} \qquad (5.9$$

The minus sign inside the brackets occurs because positive ϑ_v corresponds to an expansion.

Guided by the example in § 5.3 it is assumed that $\vartheta_v/\phi_* << 1$. Eqs. 5.8 and 5.9 can be expanded in Taylor's series about $\vartheta_v = 0$ to obtain

$$p_3/p_\infty = p_*/p_\infty + 2\vartheta_v \left\{p_*/p_\infty + \varepsilon\right\}\left\{\phi_*^2 + \left(\frac{2(1-\varepsilon)}{M_\infty}\right)^2\right\}^{-\frac{1}{2}} \qquad (5.10$$

and

$$p_4/p_\infty = p_2/p_\infty \left\{1 - \left(\frac{1+\varepsilon}{1-\varepsilon}\right) M_2 \vartheta_v\right\} + \cdots \qquad (5.11$$

By using the matching condition $p_3 = p_4$ across the slipline CE an equation for ϑ_v is obtained :

$$\vartheta_v = \frac{p_2 - p_*}{p_\infty}\left\{\gamma M_2 \frac{p_2}{p_\infty} + 2\left(\frac{p_*}{p_\infty} + \varepsilon\right)\left(\phi_*^2 + \left(\frac{2(1-\varepsilon)}{M_\infty}\right)^2\right)^{\frac{1}{2}}\right\} \qquad (5.12$$

By using this expression and Eq. 5.11, the variables in regions (3) and (4) may be calculated. Also the pressure in region (5) is simply

$$p_5/p_\infty = p_2/p_\infty \left(1 - 2\gamma M_2 \vartheta_v + \cdots\right) \qquad (5.13$$

The solution is valid in the limit $M_2 \vartheta_v \to 0$ and the error is $O(M_2 \vartheta_v)$. Eq. 5.11 is the first term approximation to the Busemann's series for simple wave in the limit of large M_∞. Hence Eq. 5.11 is also valid when CFG is a shock wave. ϑ_v is then negative.

In general, even if the hypersonic small disturbance theory is used, construction of the field downstream of the interaction would require the use of step-by-step procedures.

5.5) Strength of the Reflected Waves in the Double Wedge Flow.

The pressures p_2, $p_3 = p_4$, p_5 and p_* in the double wedge flow can be used to measure the strength of the reflected waves. Variation coefficients χ and ξ are defined as

$$\chi = \frac{p_2 - p_5}{p_2}, \quad \xi = \frac{p_* - p_5}{p_2 - p_5} \qquad (5.14$$

χ is the ratio of the fall-off in pressure through FG in Fig. 5.1 to the maximum pressure generated on the surface, and ξ is the ratio of the change across subsequent waves to that through FG.

Now

$$\chi \text{ and } \xi \sim \text{fns}\left(M_\infty, \phi_1, \phi_2, \gamma\right) \qquad (5.15$$

When the hypersonic small disturbance conditions hold,

$$\chi \text{ and } \xi \sim \text{fns}\left(M_\infty \phi_1, \phi_2/\phi_1, \gamma\right) \qquad (5.16$$

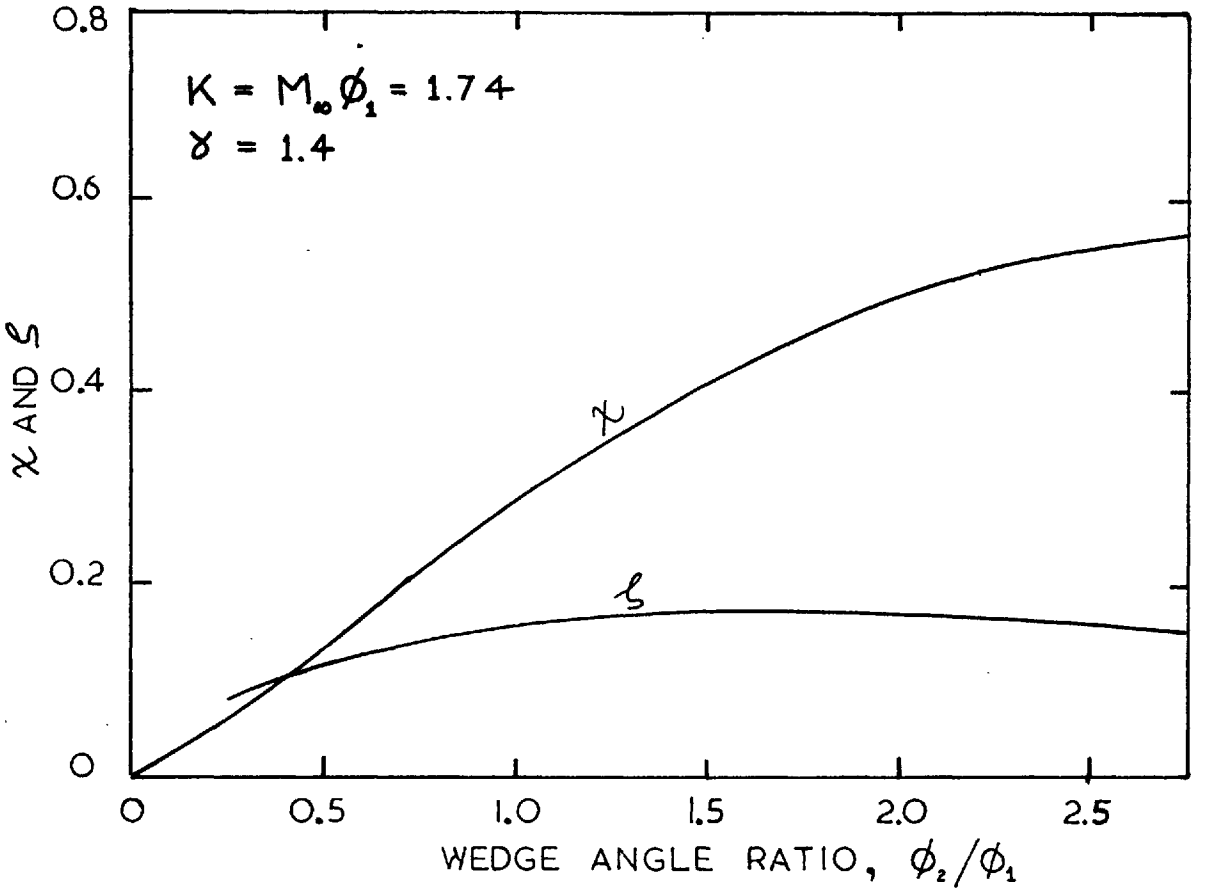


FIG. 5.9 : VARIATION OF χ AND ς WITH ϕ_2/ϕ_1

and the number of independent variables is reduced by one, (Hayes and Probstein, 1959, p.36).

Numerical results calculated by using the solution in §5.4 are now given. In Fig. 5.9, χ and ξ are plotted against ϕ_2/ϕ_1 for $K = M_\infty \phi_1 = 1.74$ and $\gamma = 1.4$. χ is large and increases with increase in ϕ_2/ϕ_1. ξ remains moderately small, indicating that most of the pressure variation occurs through the first reflected wave (FG in Fig. 3.1). In Fig. 3.10, χ and ξ are plotted against γ for $K = 1.74$ and $\phi_2/\phi_1 = 2$. χ increases as $\gamma \to 1$; whilst ξ remains almost independent of γ.

After this investigation was completed, Bird (1963) published some results for the double wedge problem, which were based on numerical solutions to the exact equations. An interesting comparison with this work can be made. This will be combined with the investigation of the effect of $K = M_\infty \phi_1$ on χ and ξ. Bird's results are given in the form of reflection coefficients. These are

$$R_1 = \frac{p_2 - p_3}{p_2 - p_1}, \quad R_2 = \frac{p_2 - p_*}{p_2 - p_1} \qquad (5.17$$

in which the variations are now compared with the strength of the second shock. In Fig. 3.11, χ and ξ are given for $\gamma = 1.4$ and $\phi_2/\phi_1 = 1$ in the range $0.5 \leq K \leq 3.5$. The exact solutions are those given by Bird ($M_\infty = 8$, and 16, at $\phi_1 = 10^\circ$) and the author ($M_\infty = 10$ and $\phi_1 = 10^\circ$). The excellent agreement between the two

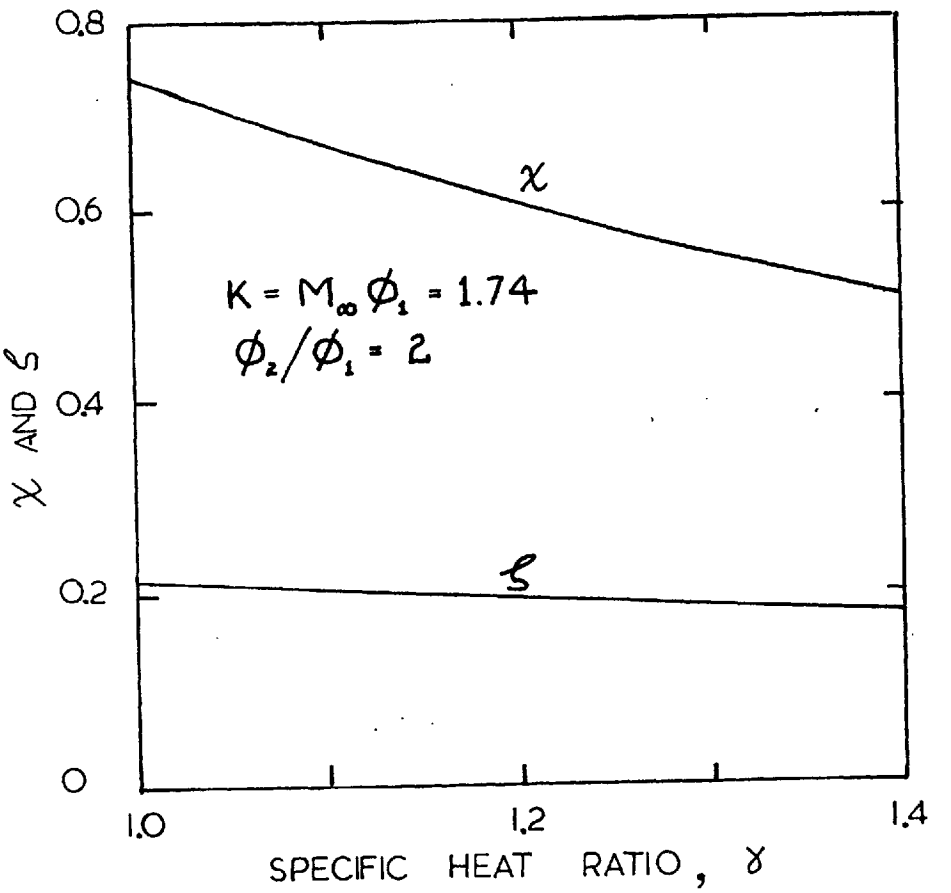


FIG 5.10 : VARIATION OF χ AND ζ WITH γ.

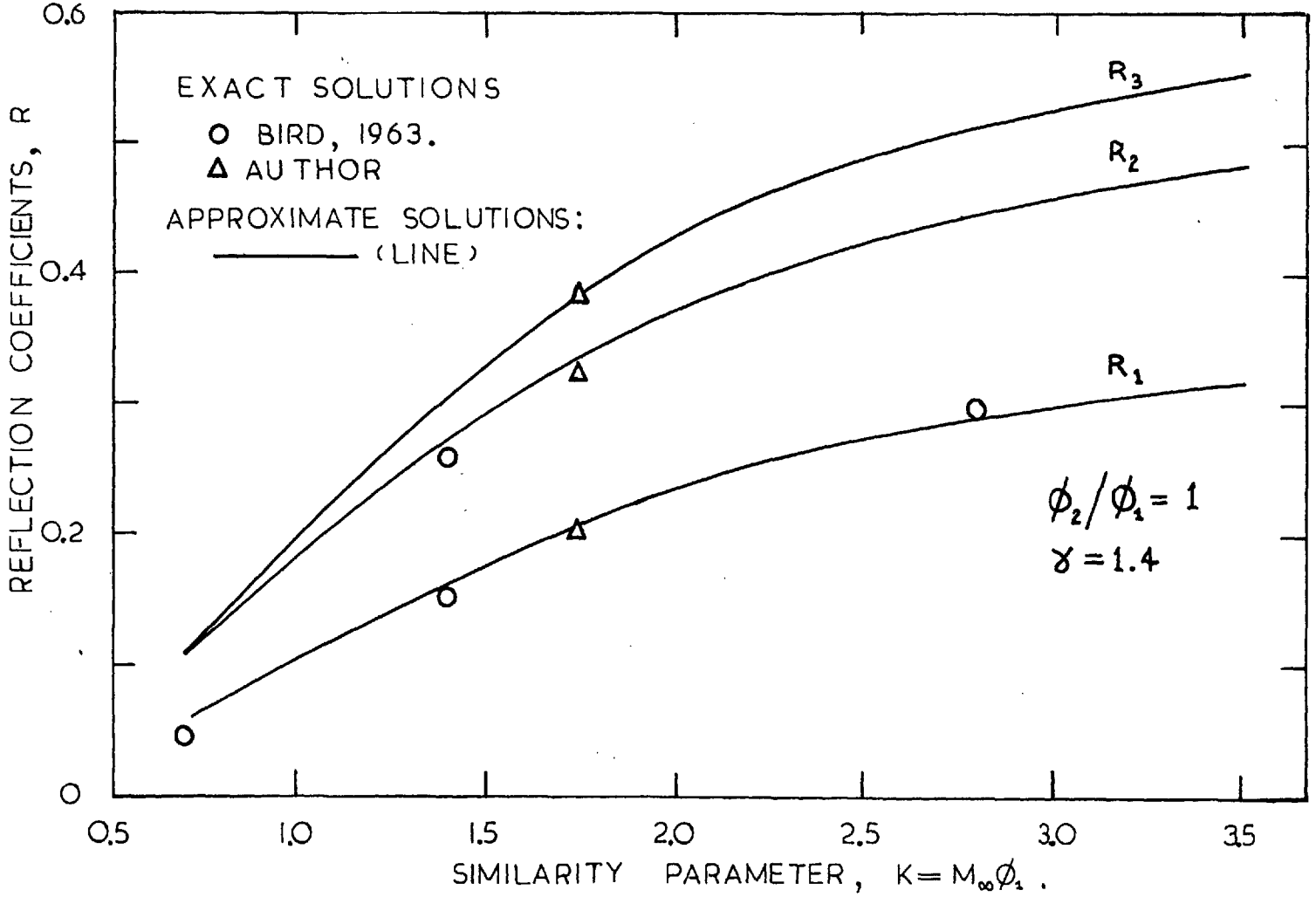


FIG.5.11 : VARIATION OF R_1, R_2 AND R_3 WITH K .

demonstrates the usefulness of the hypersonic small disturbance theory when investigating this type of problem.

The coefficients R_1 and R_2 increase rapidly with increase in $K = M_\infty \phi_1$, thus indicating that the reflected waves are strong in hypersonic flow. It has been noted that at hypersonic Mach numbers, $p_5 < p_*$. Consequently it appears that a better measure of the effect of the reflected waves on the wedge might be given by

$$R_3 = \frac{p_2 - p_5}{p_2 - p_1} \qquad (5.18$$

rather than R_2. R_3 is given in Fig. 5.11. R_3 exceeds R_2 and the difference between them increases as K increases.

The quantity v_v / ϕ_* is plotted against K for $\phi_2/\phi_1 = 1$ and $\gamma = 1.4$ in Fig. 5.12. The assumption that $v_v/\phi_* \ll 1$ made in § 5.4 is confirmed.

5.6) Strength of the Reflected Waves in the Centred Compression and Shock Flow.

The quantities χ and ξ are defined as for the double wedge flow. When Eq. 5.12 applies :

$$\chi \text{ and } \xi \sim fns\,(M_\infty \phi_*, \gamma) \qquad (5.19$$

In Figs. 5.13 and 5.14, χ and ξ are plotted against K and γ respectively. χ increases rapidly with increase in either M_∞ or ϕ_* ; it increases moderately as $\gamma \to 1$. In both

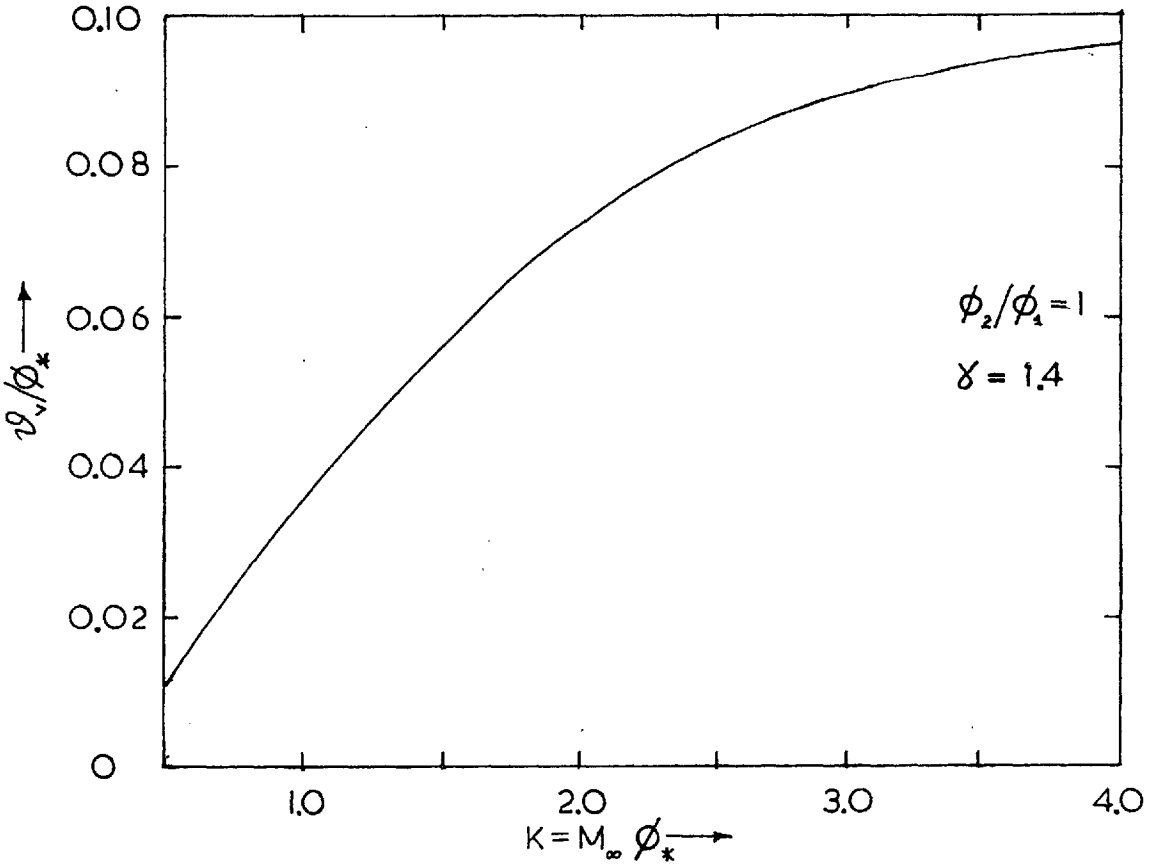


FIG. 5.12 : VARIATION OF ϑ_v/ϕ_* WITH $K = M_\infty \phi_*$.

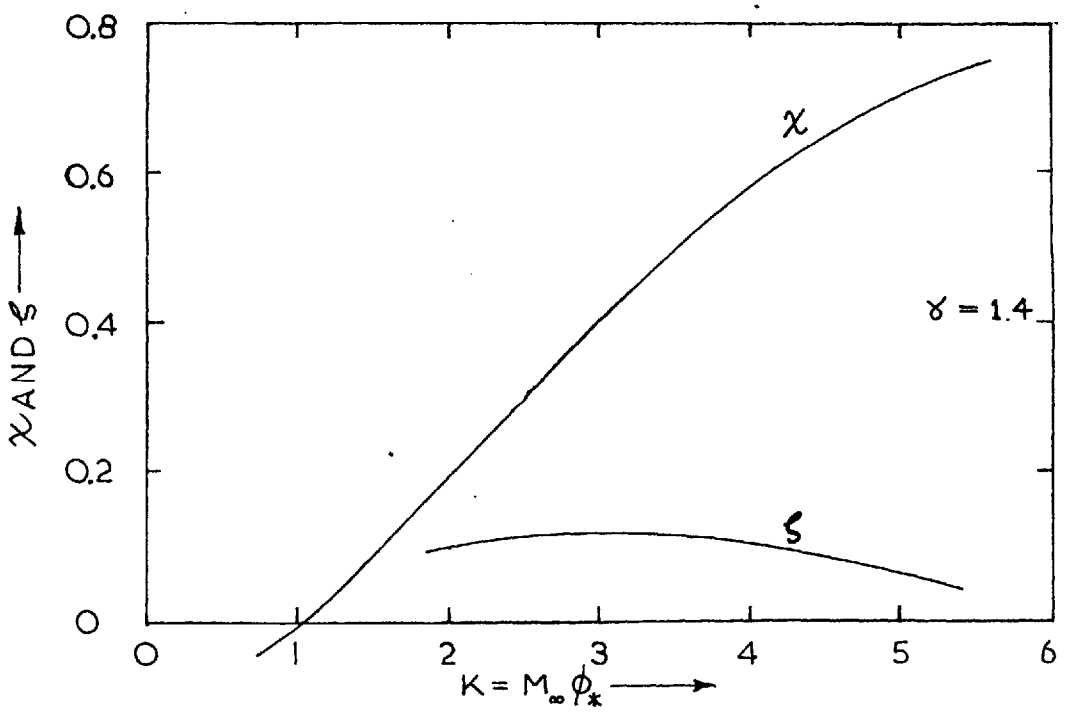


FIG.5.13 : VARIATION OF χ AND ζ WITH $K = M_\infty \phi_*$

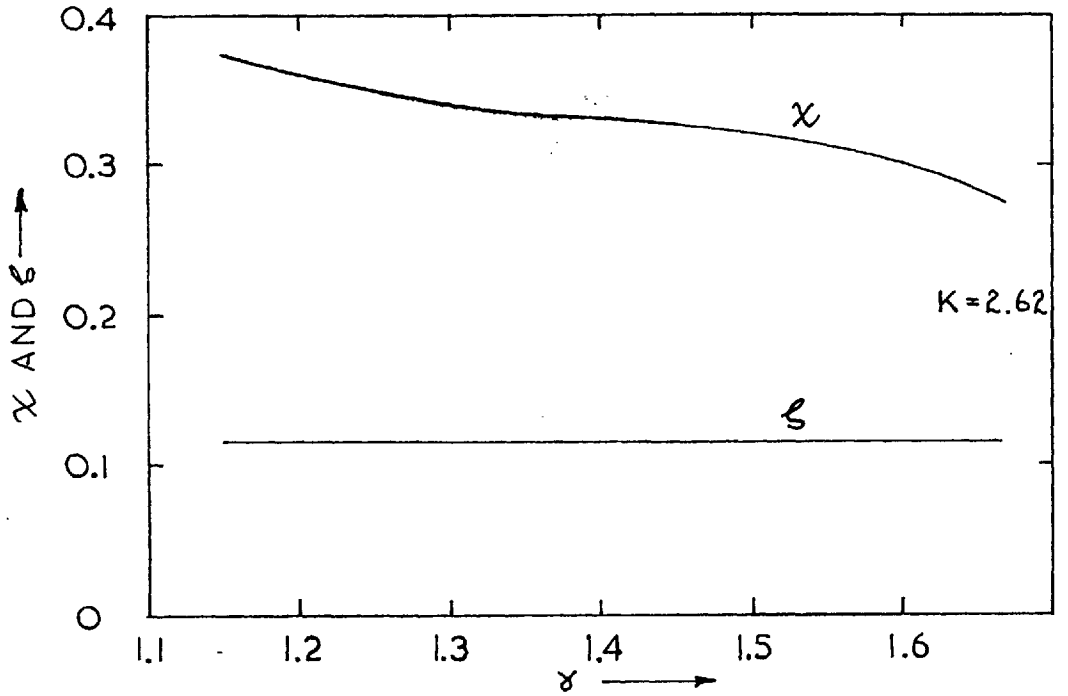


FIG: 5.14 : VARIATION OF χ AND ζ WITH γ.

cases δ remains relatively small.

Examination of the hypersonic small disturbance relations for the shock and simple wave deflections, shows that, in the limit $M_\infty \to \infty$,

$$\chi = \frac{p_2 - p_*}{p_2} = 1 + O\left(M_\infty^{(\varepsilon-1)/\varepsilon}\right) \qquad (5.20$$

This model shows that the formation of shock waves by compression waves will generate reflected Mach waves which will be strong at hypersonic speeds.

6) Experimental Facility and Models

6.1) Description of Facility

The Imperial College Gun Tunnel is a cold blowdown hypersonic facility in which the reservoir conditions are generated by free piston compression. An outline drawing of the tunnel is given in Fig. 6.1. High pressure air, stored initially in the driver reservoir A is released into the barrel C by bursting a metal diaphragm B. This accelerates a piston D, which is brought to rest by compressing the gas initially in the barrel into a small space just ahead of the tunnel nozzle E. This slug of gas forms the effective tunnel reservoir. The gas expands through the nozzle E into the working section F and the dump tank G. Prior to each run, the working section - which is evacuated - is isolated from the barrel by an adhesive tape diaphragm placed across the throat. Details of the tunnel design and operation are given by Needham (1963).

The flow is delivered to the open jet working section by a conical nozzle having an included angle $\alpha_N = 20^\circ$ and an exit plane diameter $D_E = 8$ inches. The nozzle is fitted with interchangeable throats which permit the flow to be delivered at nominal Mach numbers (M_N) of 7.5, 10, and 15.

For a given tunnel geometry, the effective reservoir pressure p_R is determined only by the initial piston drive pressure p_D ; whereas the reservoir temperature T_R and the tunnel

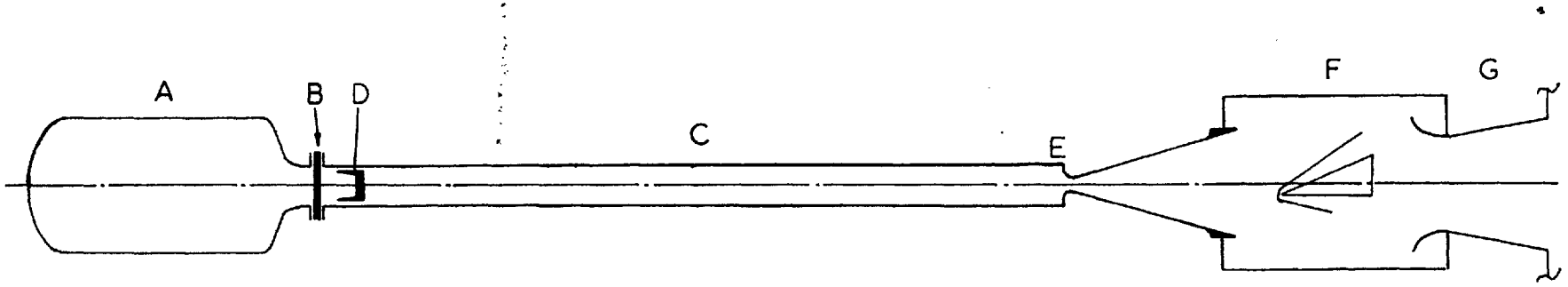


FIG. 6.1 : DIAGRAM ILLUSTRATING MODE OF OPERATION OF THE GUN TUNNEL.

running time t_R depend on the ratio p_0/p_B .. The attainable flow conditions are summarized in table 6.1.

TABLE 6.1

ATTAINABLE TUNNEL CONDITIONS

$p_0 = 2015$ psia , $p_R = 1590$ psia

UNIT REYNOLDS NUMBER AND RUNNING TIMES

p_B psia	T_R °K	$M_N = 7.5$		$M_N = 10$		$M_N = 15$	
		Re/in	t_R	Re/in	t_R	Re/in	t_R
14.7	13000	3.0×10^5	12	1.6×10^5	60	$.55 \times 10^5$	400
50	800	5.9×10^5	32	3.2×10^5	140	1.2×10^5	1000
80	740	7.8×10^5	40	4.2×10^5		1.6×10^5	
100	670	8.9×10^5	45	5.0×10^5		1.8×10^5	

t_R in milliseconds.

The tunnel is equipped with conventional Schlieren flow visualisation apparatus. The light source is an electric spark having a duration of less than 3 microseconds. The spark timing is controlled by an electronic delay unit.

6.2) Structure of the Flow in The Working Section

It is common practice to use conical nozzles in hypersonic wind tunnels. Such nozzles produce a corresponding conical or source-like flow in the working section(see, for example Vas and Bogdonoff, 1959). This flow has a considerable

effect on the pressure distributions generated on the models tested in the tunnel. Such effects can be minimised by making the models as as possible in relation to the jet size: $\ell_M / D_E << 1$. In the tests described here, instrumentation requirements imposed $\ell_M / D_E \doteq 0.9$. For models as large as this, the measurements must be corrected to account for the effects of the source flow.

The distribution of Mach number ($M = M(x)$) and free stream static pressure (p_∞) on the jet centre line in the College tunnel are given in Fig. 6.2.

The slope of the streamlines relative to the jet axis can be calculated from the measured Mach number distribution. Near the jet axis, if $y / R_E << 1$;

$$\alpha\left(x/R_E\right) = \tilde{\omega}\, y/R_E + \cdots ; \quad R_E = \frac{D_E/2}{\tan(\alpha_N/2)} \qquad (6.1$$

R_E is a characteristic length, and is the distance from the nozzle cone apex to the exit plane, and (x,y) are co-ordinates parallel and perpendicular to the jet axis, with origin in the exit plane.

An approximate expression for $\tilde{\omega}$ is given in Appendix 4, and the calculated values of $\tilde{\omega}$ in the working section are given in Fig. A1. The geometric estimate is based on the assumption that the nozzle flow is inviscid. Then $\tilde{\omega} = \alpha_N / D_E$. The values of $\tilde{\omega}$ at the nozzle exit plane are given in Table 6.2.

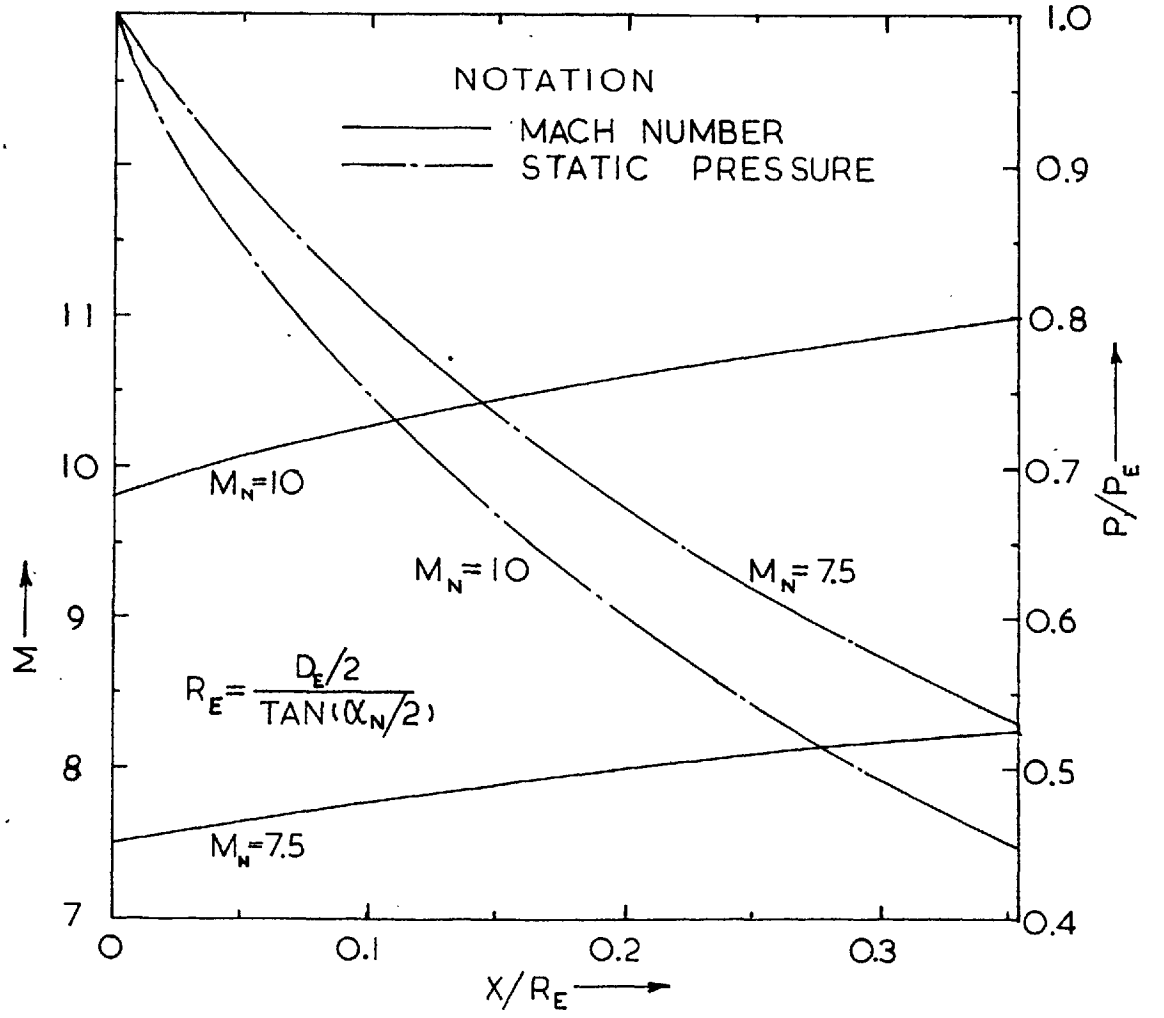


FIG. 6.2: AXIAL DISTRIBUTION OF MACH NUMBER AND STATIC PRESSURE.

TABLE 6.2

INCIDENCE FACTOR $\tilde{\omega}$ (DEGREES / INCH)

Geometric	M = 7.5	M = 10
2.5	2.2	2.9

To illustrate the way in which such a field affects the pressure distributions on a model, consider the flow on a wedge of angle Φ_w. Using the concepts of Newtonian impact theory, it is easily shown that

$$p_w(x) = \rho_\infty(x) U_\infty^2(x) \sin^2\left(\Phi_w - \alpha(y_b)\right) \qquad (6.2$$

where all quantities are evaluated at the point of impact. This can be put in the form

$$p_w(x) = K_1 \left\{ M(x) \right\}^{\frac{-2}{\gamma-1}} \sin^2\left\{ \Phi_w \left(1 - \tilde{\omega} x\right) - \tilde{\omega} K_2 \right\} \qquad (6.3$$

where K_1 and K_2 are constants. Since $dM/dx > 0$ in a conical flow, $dp/dx < 0$ on the wedge. This can be conveniently considered to arise from two causes :

(i) the Mach number gradient, and

(ii) the change of incidence of the free stream along the model.

In general, both of these effects will superpose a negative pressure gradient on the pressure distribution obtained on the model in a uniform flow. Eq. 6.3 shows that, for a given Mach number distribution, an increase in the angle of the wedge

will increase the gradient of the superposed curve. Only the Mach number gradient will affect the pressure distribution on a flat plate which is mounted along the jet axis.

Two empirical methods for correcting results obtained in a conical flow have been proposed in the literature. Vas and Bogdonoff (1959) suggested that the measured pressure $p(x)$ be expressed in the form:

$$P_c = \frac{p(x)}{p_\infty(x)} \quad , \quad C_{P_c} = \frac{p(x)}{\frac{1}{2}\gamma M^2(x_L) p_\infty(x)} \qquad (6.4$$

P_c is the corrected pressure ratio, $p(x)$ is the measured pressure on the model, and $p_\infty(x)$ is the free stream static pressure distribution on the tunnel axis. The corrected pressure coefficient C_{P_c} follows from the definition of P_c ; $M(x_L)$ is the free stream Mach number just ahead of the leading edge of the model. The results are then corrected to the free stream conditions at the model leading edge. This is known as the "local pressure" correction.

The second is the "buoyancy" method (Baradell and Bertram, 1960). This is a linear correction, in which the pressure decrement gradient:

$$\lambda = 1 - p_\infty(x)/p_\infty(x_L) \qquad (6.5$$

is added to the measured pressure ratio:

$$P_c = p(x)/p_\infty(x_L) + \lambda . \qquad (6.6$$

Baradell and Bertram examined these correction procedures

by applying them to the pressure distributions generated on a flat plate with a blunt leading edge in an ideal source flow as calculated by the sonic wedge characteristics theory. The corrected results were then compared with the solution obtained for a uniform flow having the same free stream conditions as that generated by the source flow at the leading edge. The "local pressure" method was found to considerably overcorrect, whereas the "buoyancy" method was found to give good agreement.

In these comparisons the calculated pressures on the plate were of the order of the free stream static pressure. In the present tests, the measured surface pressures are normally much greater than (up to 100 times) the free stream static pressure. Under such conditions the "buoyancy" method does not give useful corrections, since in Eq. 6.6, $p(x)/p_\infty(x) >> \lambda$.

6.3) Models

6.31) Model "A", 20 Wedge: This model was used to investigate the effect of the conical flow on the pressure distributions obtained on the other models.

The layout of the tappings is given in Fig. A2, Appendix. Two sets of tappings (Generators A and B) were fitted to permit the spanwise pressure distribution to be examined. Detachable side wedges were fitted.

The effect of leading edge bluntness and shock-boundary layer

on the pressure distribution near the leading edge was examined (Appendix 5). The calculations showed that both of these effects were negligible at the first tapping.

6.32) Model "B", Overfocussed Surface; The profile and layout of the pressure tappings on the surface are given in Fig. A3, Appendix. The surface comprises a 10° wedge forebody, a concave curve, and a 30° ramp. The geometry was chosen (by trial and error) so that the flow was overfocussed.

The simple wave theory (§ 2.2) predicts a constant pressure on the ramp. Thus (in a uniform flow) pressure variations on the ramp would be caused entirely by reflected waves. The model was designed so that all of the reflected waves intersected the model surface at the ramp.

Generators A, B and C were included to examine the spanwise pressure distributions. Tappings nos. 10 and 11 on generature B were fitted with different size tubes to examine the effect of tapping size on the measurements.

During the tests it was found necessary to use side plates on this model. The calculations in § 6.2 indicated that the streamlines in the jet were inclined at approximately 5° to the axis at the sides of the model. Hence, if the side-plates were mounted parallel to the axis, they would have been at 5° incidence to the free stream. This in turn would have caused them to generate

strong shock waves over the model, and to produce undesirable three-dimensional effects. To minimise such effects, the sides of the model were cut at 5° to the axis, so that the side-plates would be approximately aligned with the local stream.

The leading edge effects examined in Appendix 5 were estimated to be negligible at generator "A".

6.33) Model "C", Underfocussed Surface; This model comprised a 10 wedge forebody, a curved surface, and a 20° ramp. The geometry of the model was chosen so that, at $M_N = 10$:

(i) The principal waves generated by the curved surface intersected the leading edge shock before they formed a shock wave, and

(ii) the first reflected wave intersected the surface upstream of the ramp. The design wave structure is given in Fig. A4, which also gives the layout and distribution of tappings on the model.

Initial experiments on a pilot model indicated that at $M_N = 7.5$ the first reflected waves hit the ramp well downstream. Hence significant pressure fall-off was expected only at $M_N = 10$. Estimation of the effect of shock-boundary layer interaction indicated that at tapping no. 1 on the wedge,

$$p/p_w = 1.20 \quad @ \; M_N = 10, \qquad (6.7$$

where p_w is the theoretical inviscid 10° wedge pressure.

6.34) Model "D", Cubic Surface; This model was designed to test the similar solutions described in § 4. The equation of the surface is

$$y_b = x^3/150 \qquad (6.8$$

The slope at the end of the surface is $\vartheta_R = 28^\circ$. The surface was continued as a ramp to measure the centrifugal pressure rise across the shock layer at the end of the cubic surface.

Sufficiently far downstream on the ramp, the pressure should approach the tangent wedge value. Hence, for $k = 3$ and $\gamma = 1.4$, we expect (Eq. 4.24)

$$\frac{p_c - p_R}{\rho_\infty U_\infty^2 \vartheta_R^2} \simeq 0.55 \text{ as } M_\infty \to \infty, \qquad (6.9$$

where p_c is the pressure at the end of the cubic surface and p_R is the pressure far downstream on the ramp.

The theory given in § 3 shows that in the first order problem, the behaviour in the leading edge section does not affect the region where the similar solutions are valid. It is therefore expected that small changes in the shape of the leading edge region such as that caused by the boundary layer growth will not affect the experimental results significantly.

6.4) Instrumentation.

6.41) Electronics; Pressures were measured by unbonded strain-gauge, absolute pressure d.c. excited C.E.C. type transducers. The outputs were transmitted to Tektronix 502 oscilloscopes and recorded on Polaroid-Land Cameras. Up to seven measurements could be taken per tunnel run. The outputs of the transducers varied between 1.5

and 0.25 milliVolts . The maximum sensitivity of the oscilloscopes was 200μV/cm , so that the minimum pressure that could be detected was .05 psi ± 10% on one channel and 0.15 psi ± 10% on the others. This limitation restricted tests to Mach numbers $M_\infty \leq 10$.

6.42) Pneumatic Considerations Affecting Model Design; The shortest running time of the tunnel occurs when $M_N = 7.5$ and is approximately 30 milliseconds. Consequently the pneumatic rise time of the measuring system had to be less than 10 milliseconds. However, the system had to be constructed so as to allow each transducer to be connected to any tapping.

The arrangement chosen is given in Fig. 6.3. The model A was mounted on the sting B . The tube from each tapping, such as C was brought to one of a number of short tubes D mounted in a framework E (the tapping exchange) bolted to the rear of the model. The transducers and enclosing chambers (typically, F) were mounted in a box attached to the rear of the exchange. Each transducer was connected to a tube in the exchange. The transducer was connected to the selected tapping by a bridge pipe G. The structure was provided with a detached fairing. With this arrangement the rise time was usually less than 5 milliseconds. Average tube dimensions were 1/16" dia. by 5" to 8" long.

The natural frequency of the transducer diaphragms was about 12 kC. During the preliminary tests, it was found that if the connecting pipes were made sufficiently short (say 2" long), then

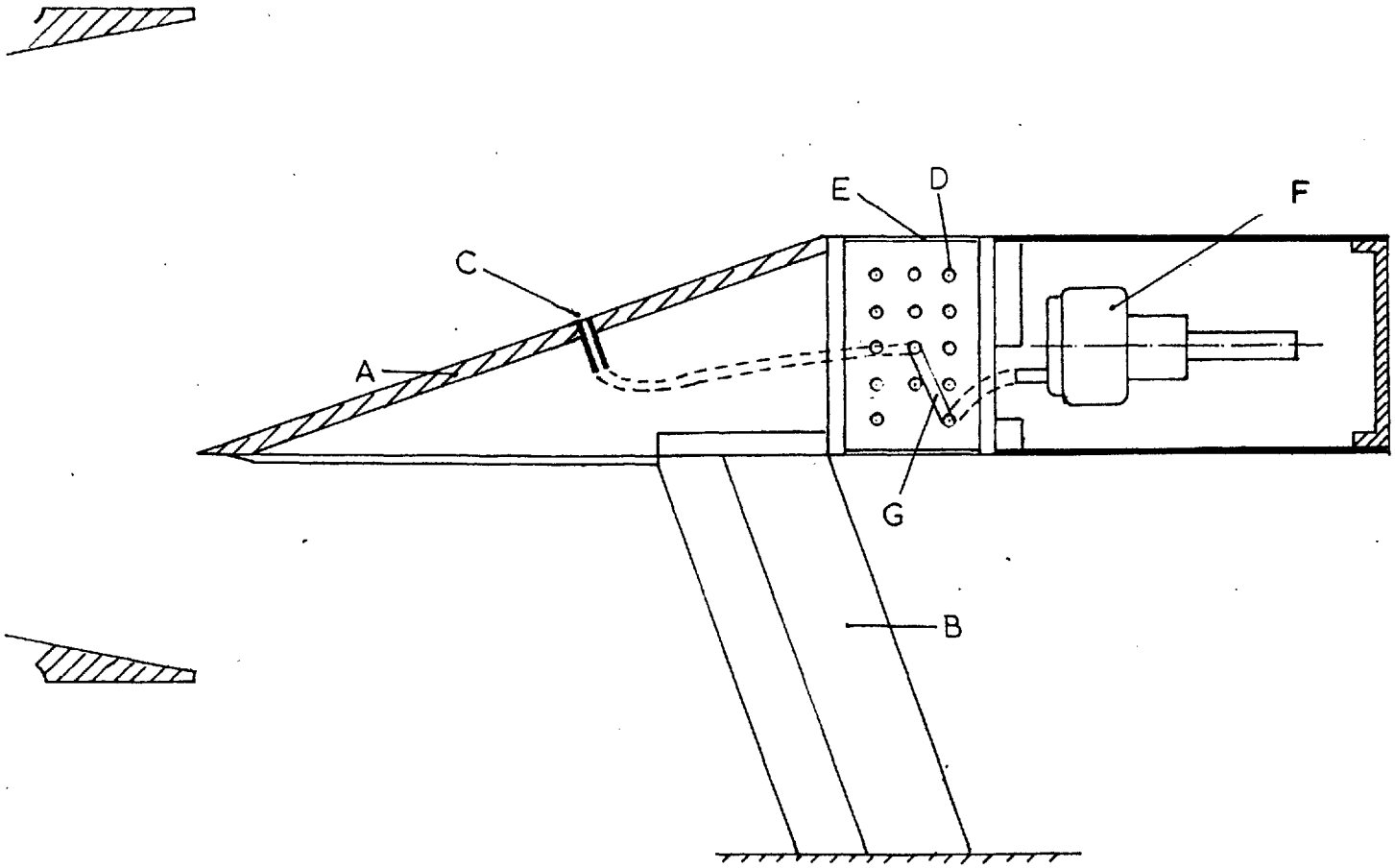


FIG. 6.3 : ARRANGEMENT OF PRESSURE TRANSDUCER PIPEWORK

the oscilloscope traces showed a spurious oscillation or "ringing" at about this frequency. To suppress this, the pipes were kept not less than 5" long.

This arrangement did not allow the models to be tested at incidence.

6.43) Interpretation of Oscilloscope Traces; A typical oscilloscope trace showing the pressure recorded at the transducer is given in Fig. 6.4. A characteristic feature of the tunnel is the periodic fluctuations in the effective reservoir pressure. This is caused by the reflections of waves in the driver gas in the barrel. Corresponding fluctuations occur in the static pressure traces.

To minimise errors from this source, the reading on the trace was taken to be the average ordinate over a small region about a point at a specific time t_r after the commencement of the run. The time t_r was made long enough to ensure that the tapping tube lag did not influence the reading.

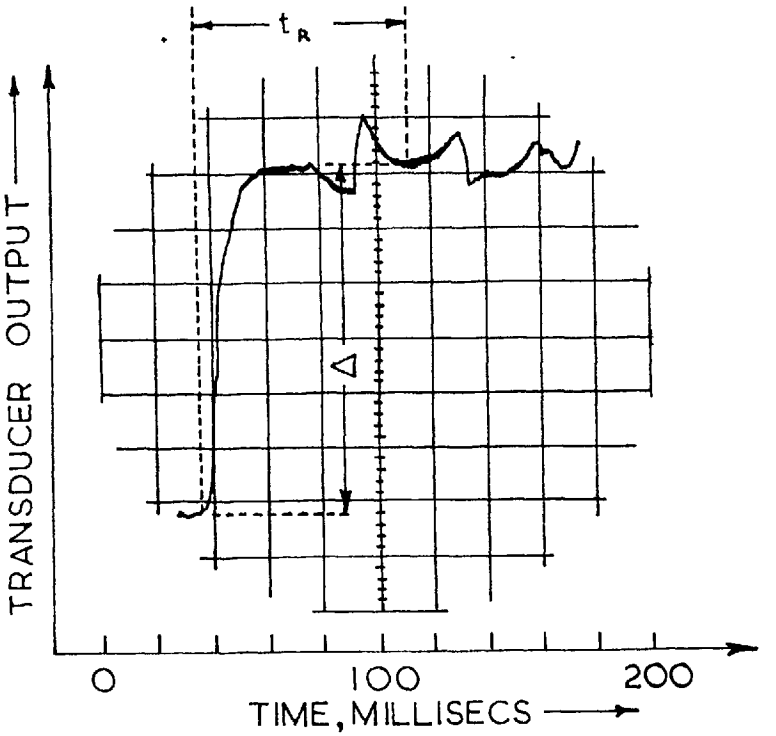


FIG.6.4: TYPICAL OSCILLOSCOPE TRACE AT M_N=10.

7) Test Programme and Results.

7.1) Programme;

7.11) Preliminary Experiments;

(i) Repeatability and Accuracy Tests: To obtain the required number of measurements at any given combination of test conditions, the tunnel had to be fired several times. A test was conducted to examine the overall accuracy and repeatability of the tunnel and measuring system. Measurements were taken on generators B and C of Model B at $M_N = 7.5$ and 10. Repeated readings were taken at each tapping. Between readings, the tappings and transducers were interchanged, so that each of the readings at a given tapping was interpreted by a different transducer.

(ii) Effect of Tapping Size and Pipe Length: Checks for possible effects of tapping size were conducted by comparing measurements taken through the symmetrically placed tappings numbered 10 and 11 on generator B, model B. Tapping number 8 was fitted with a tube of length greater than the standard to examine the effect of variation of tube length. Both of these checks were carried out simultaneously with (i) above.

(iii) Effects of Barrel Pressure p_B; All of the runs but one in (i) above were taken with $p_B = 50$ psia, the other was taken with $p_B = 85$ psia.

(iv) Effect of Side-Plates on Spanwise Pressure Distributions; The spanwise pressure distributions on generator C of model B, were examined with three pairs of side-plates fitted in turn.

The approximate dimensions of the side-plates are :

(α) : 5" × 4" × 3/16" ,

(β) : 5" × 2" × 3/16" ,

(γ) : 3" × 1½" × 0.010.

The side-plates are shown superimposed on the model B in Fig. A6. One of the set β (designated β - B) was fitted with a blunt leading edge ($t_L \simeq 1/16"$) to examine the effect of plate bluntness.

7.12) Pressure Distribution on Model A Wedge;

(i) Two-Dimensional Flow Tests; Of the geometry of the four models, that of model A was the least favourable to the generation of a core of two-dimensional flow. Consequently, tests were conducted to ensure that there was a region near the centreline for which the flow was two-dimensional. The pressure distribution on generator B, was examined for three configurations :

(i) no side-wedges or side-plates,

(ii) side-plates (δ) fitted,

(iii) side-wedges fitted.

Side-plates (δ) are shown superimposed on the model in Fig. A2.

(ii) Axial Pressure Distributions; These were taken with side-wedges fitted.

7.13) Pressure Distributions on Models B, C and D; The spanwise pressure distribution at the rear of each model was checked to ensure that there was a core of two-dimensional flow; after which the axial measurements were taken.

7.2) Results of Preliminary Experiments

(i) Repeatability and Accuracy; The pressure distribution on generator C of model B at $M_N = 7.5$ is given in Fig. 7.1. Results obtained from individual runs are marked. The pressure on generator C appears constant within the range of the tappings. All points lie within 3% of the mean. The distributions on generator B at $M_N = 7.5$ is given in Fig. 7.2; the scatter is less than 3%. However at $M_N = 10$ on generator B (10° wedge) the scatter increased to 6%.

(ii) Tapping Size and Pipe Length; The pressures measured on tapping numbers 8 (tube length), 10, and 11 (tapping size) were not detectably different from the mean.

(iii) Effect of Barrel Pressure p_A; The results of the run taken with $p_B = 85$ psia are marked in Figs. 7.1 and 7.2. There was no detectable difference from the mean.

(iv) Side-plate Tests; The pressure distributions obtained at $M = 10$ on generator C of model B with the side-plates α, β, and γ fitted in turn are given in Fig. 7.3. Curve (1) is the distribution obtained with the largest set (α) fitted. Curves 2A and 2B are those for the set (β). Curve 2A is the distribution obtained when the plate β-B was fitted to the side of the model marked R in Fig. 7.3, whilst 2B gives the distribution obtained when β-B was fitted to the side L. Curve 3 is the distribution obtained when the set (γ) was fitted.

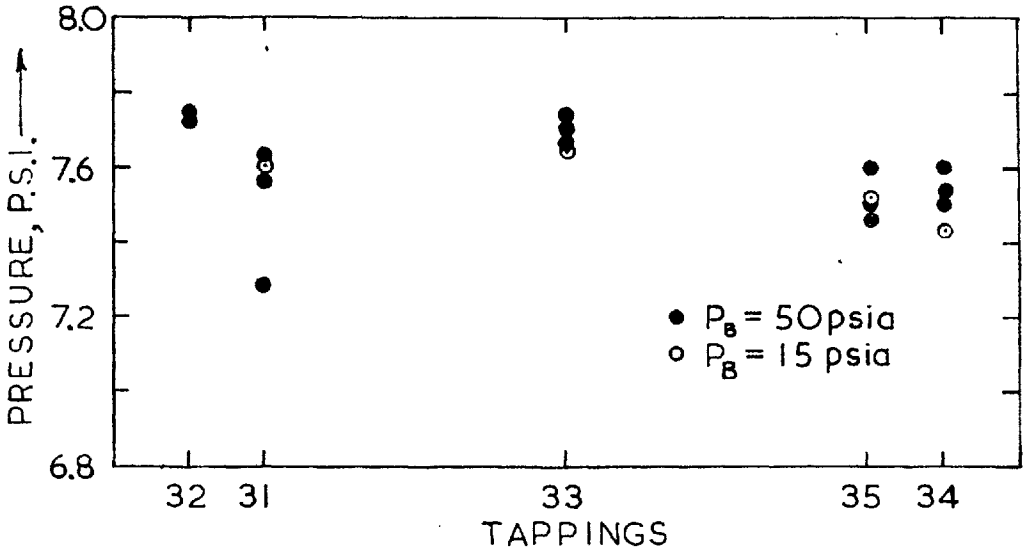


FIG. 7.1 : PRESSURE DISTRIBUTION ON GEN. "C" OF MODEL "B" AT M_N 7.5.

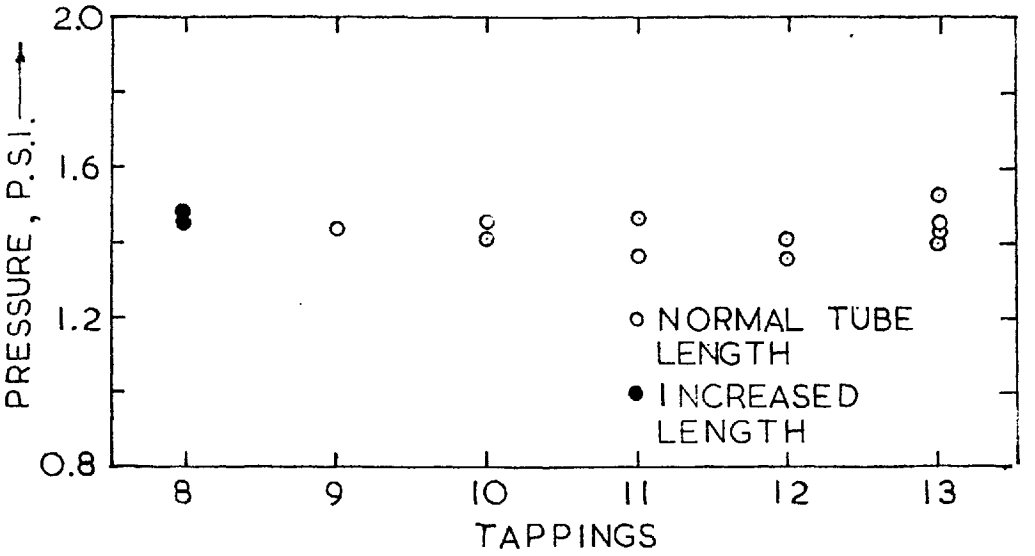


FIG. 7.2 : PRESSURE DISTRIBUTION ON GEN. "B" OF MODEL "B" AT M_N=7.5.

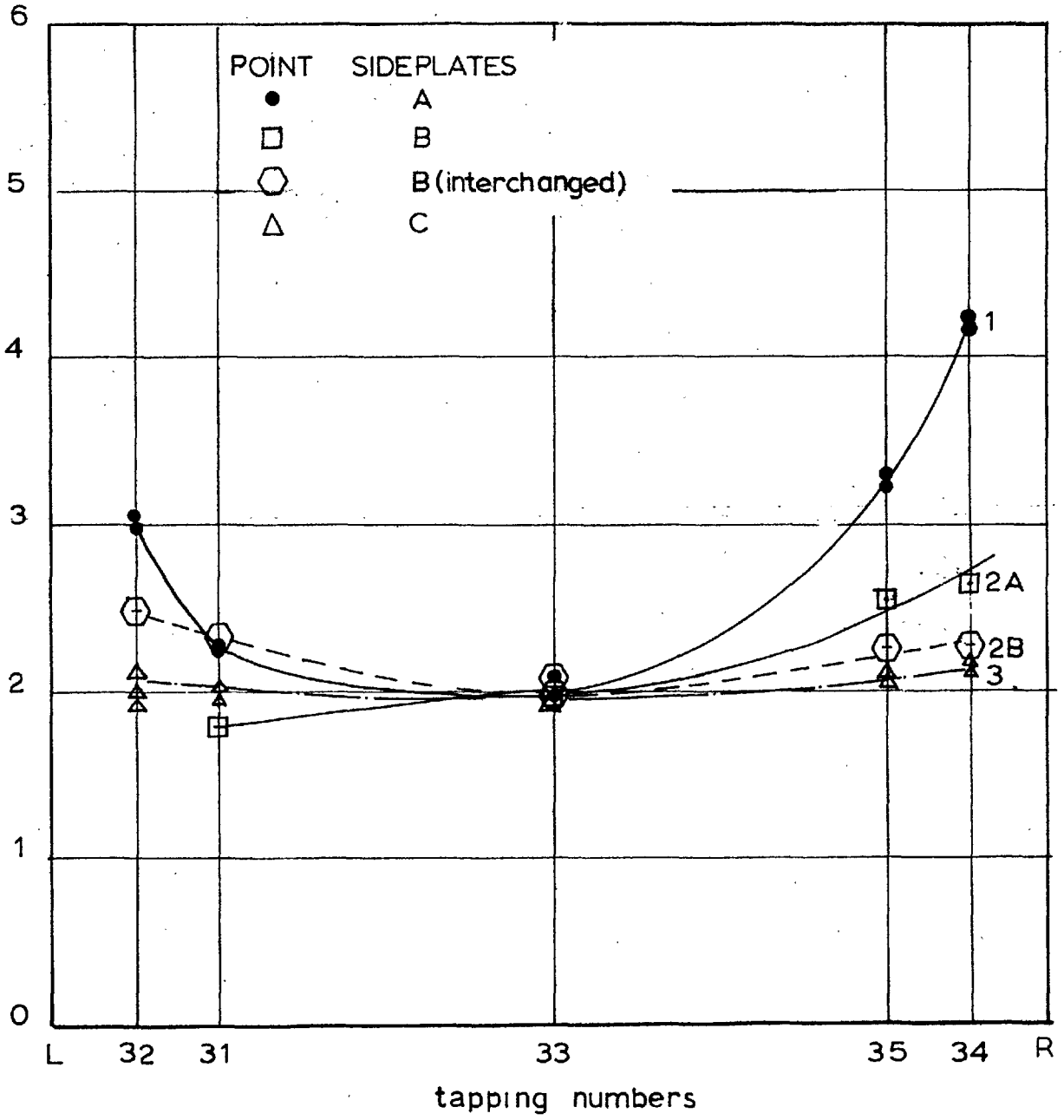


FIGURE 7.3 : EFFECT OF SIDEPLATES ON PRESSURE DISTRIBUTION ON GENERATOR "C"

Four points should be noted:

(i) All curves are asymmetric,

(ii) The magnitude of the spanwise variation decreases with decrease in the size of the side-plates.

(iii) The higher side of the asymmetry in curves 2A and 2B occurs on the side of the model to which (β-B) (the plate with the blunt leading edge) was attached.

(iv) The pressure at the centre of the model is independent of the size of the side-plates.

7.3) Pressure Distributions on Model A - the Wedge

7.31) Results

(i) Two-Dimensional Flow Tests: The pressure distributions obtained on generator B of model A are given for $M_N = 7.5$ and $M_N = 10$ in Figs. 7.4 and 7.5.

At both $M_N = 7.5$ and $M_N = 10$, the centre-line pressure is the same for the three configurations given in § 7.12 (i). This suggests that the two-dimensional wedge pressure has been attained at the rear of this model.

The pressure distribution at $M_N = 7.5$ obtained when the side-plates δ were attached, showed large spanwise variations. However a similar variation was not detected at $M_N = 10$. Because the tappings on generator B were spaced at large intervals, it seems possible that a variation corresponding to that obtained at

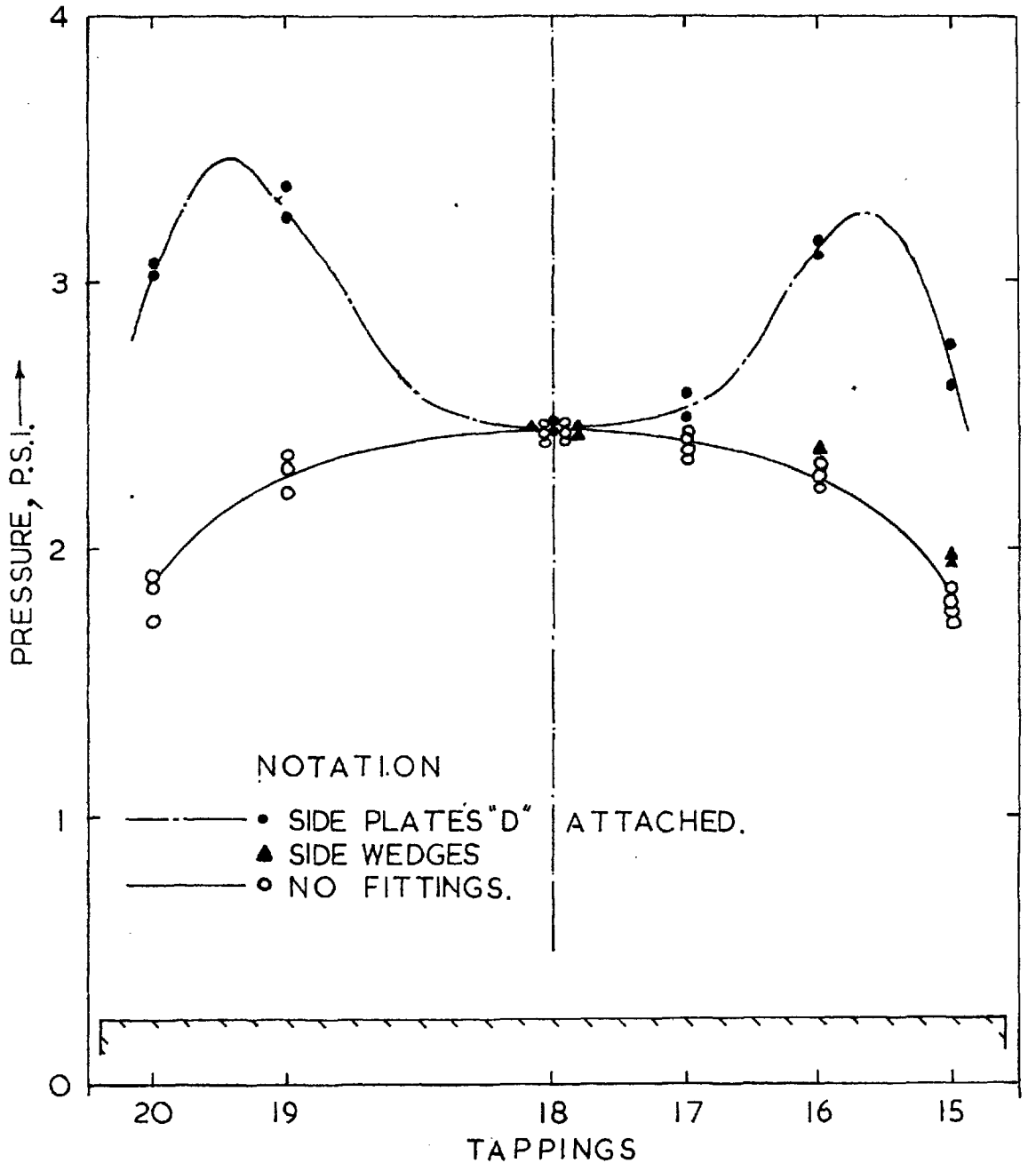


FIG.7.4 : SPANWISE PRESSURE DISTRIBUTION ON MODEL "A" AT $M_N = 7.5$.

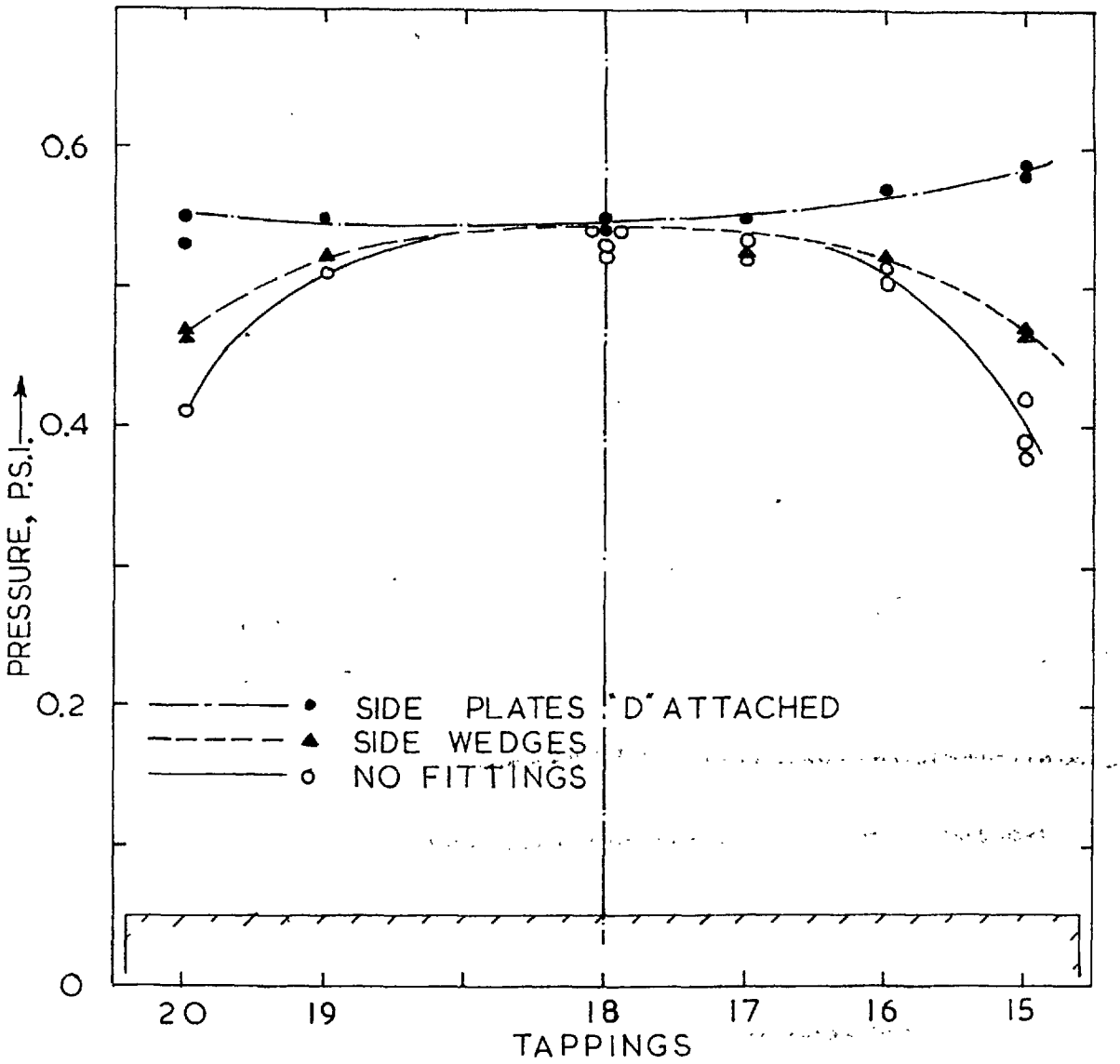


FIG. 7.5 : SPANWISE PRESSURE DISTRIBUTION ON MODEL 'A' AT M_N=1.0

$M_N = 7.5$ could have occurred at $M_N = 10$ and yet remained undetected.

The side-wedges were found to improve the spanwise pressure distribution slightly at $M_N = 10$, but at $M_N = 7.5$ no apparent benefit was obtained.

(ii) Axial Pressure Distributions: The axial distributions of surface pressure are given in Figs. 7.6 and 7.7 for $M_N = 7.5$ and $M_N = 10$ respectively. The abscissa is the quantity p/p_U, where p_U is the inviscid wedge pressure based on the measured free stream conditions at the leading edge of the model. The ordinate is x/R_M where R_M is the distance of the model leading edge from the nozzle cone apex, and x is the distance downstream from the leading edge of the model along the tunnel axis.

In both cases the pressure at the leading edge of the model is greater than the theoretical value. It falls continually along the wedge until, at the rear, it is well below the theoretical value. An explanation of this behaviour is that, in Fig. 7.6, since $\frac{\Delta Y}{R_M}$ is negative at the leading edge, the effective angle of the wedge relative to the local stream is greater than the wedge angle relative to the jet axis (Φ_w). It follows from Fig. A1 that

(i) at $x = 0$, $(\Phi_w - \alpha) \simeq 23^\circ$

(ii) at $x = l_M$, $(\Phi_w - \alpha) \simeq 18^\circ$

At the rear of the wedge its effective angle is less than Φ_w

7.32) Derived Correction Procedure:

According to the correction procedure of Eq. 6.4, the measured

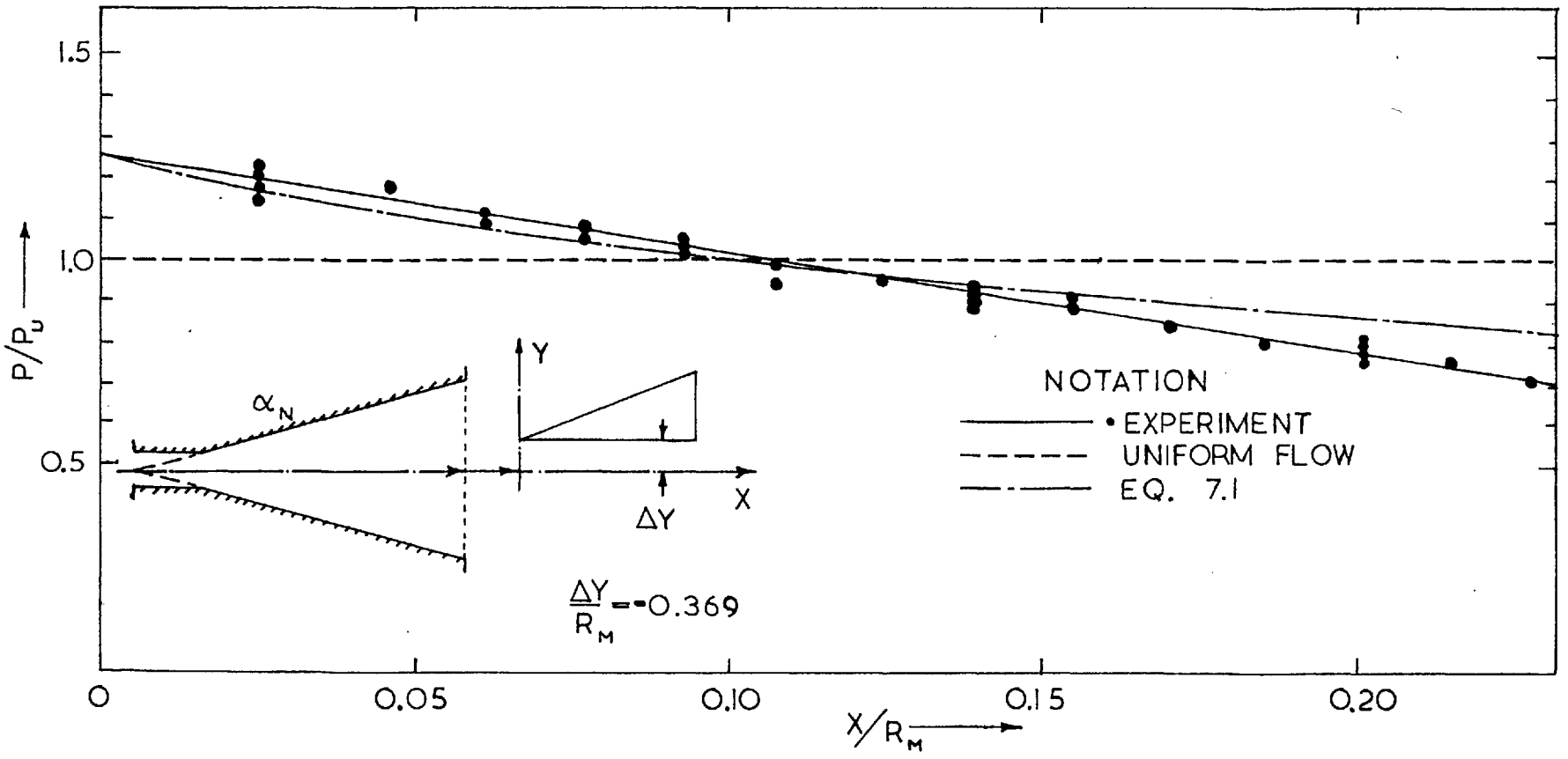


FIG. 7.6: AXIAL PRESSURE DISTRIBUTION ON MODEL "A" AT $M_N = 7.5$.

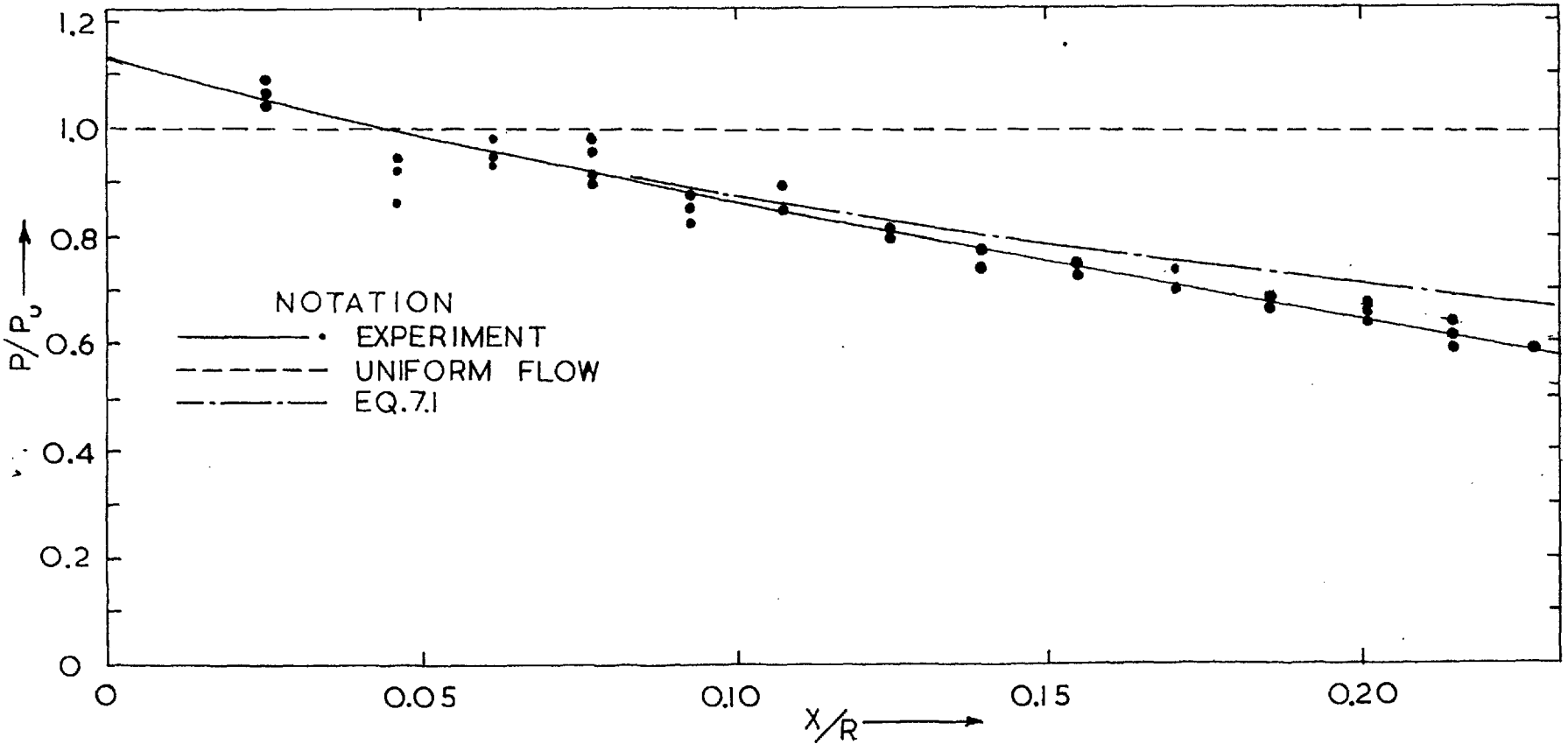


FIG. 7.7 : AXIAL PRESSURE DISTRIBUTION ON MODEL "A" AT M_N=10 .

pressure distribution on the wedge would be given by

$$p(x) = p(0) \cdot p_\infty(x) / p_\infty(0) \qquad (7.1$$

where $p(0)$ is the measured wedge pressure at the leading edge. Eq. 7.1 is plotted in Figs. 7.6 and 7.7. It appears to estimate the pressure gradient reasonably well on the forward parts of the wedge; but it underestimates the gradient towards the rear of the wedge. In contrast, Vas and Bogdonoff showed that it overestimated the gradient superimposed by the conical flow when applied to measurements taken on a flat plate. Since the method always gives a correction factor of unity at the leading edge of the model, it does not account for the incidence effects in the conical flow.

An adequate correction procedure must account for the incidence effects as well as the Mach number gradient. It is expected that incidence effects are primarily dependent on the distance (y) from the tunnel axis. Hence in the subsequent tests, the corrected pressure p_c at any point x is computed from the product:

$$p_c(x) = p(x) \frac{p_\infty(0)}{p_\infty(x)} F(y, M_N) . \qquad (7.2$$

F is an incidence correction factor assumed to be a function of M_N and y only, where y is the distance of the point on the model from the jet axis. F is chosen so that when Eq. 7.2 is applied to the measured pressure distribution on the wedge, $p_c(x)$ is the inviscid wedge pressure for the free stream conditions at the leading edge of the wedge. The function F as determined from

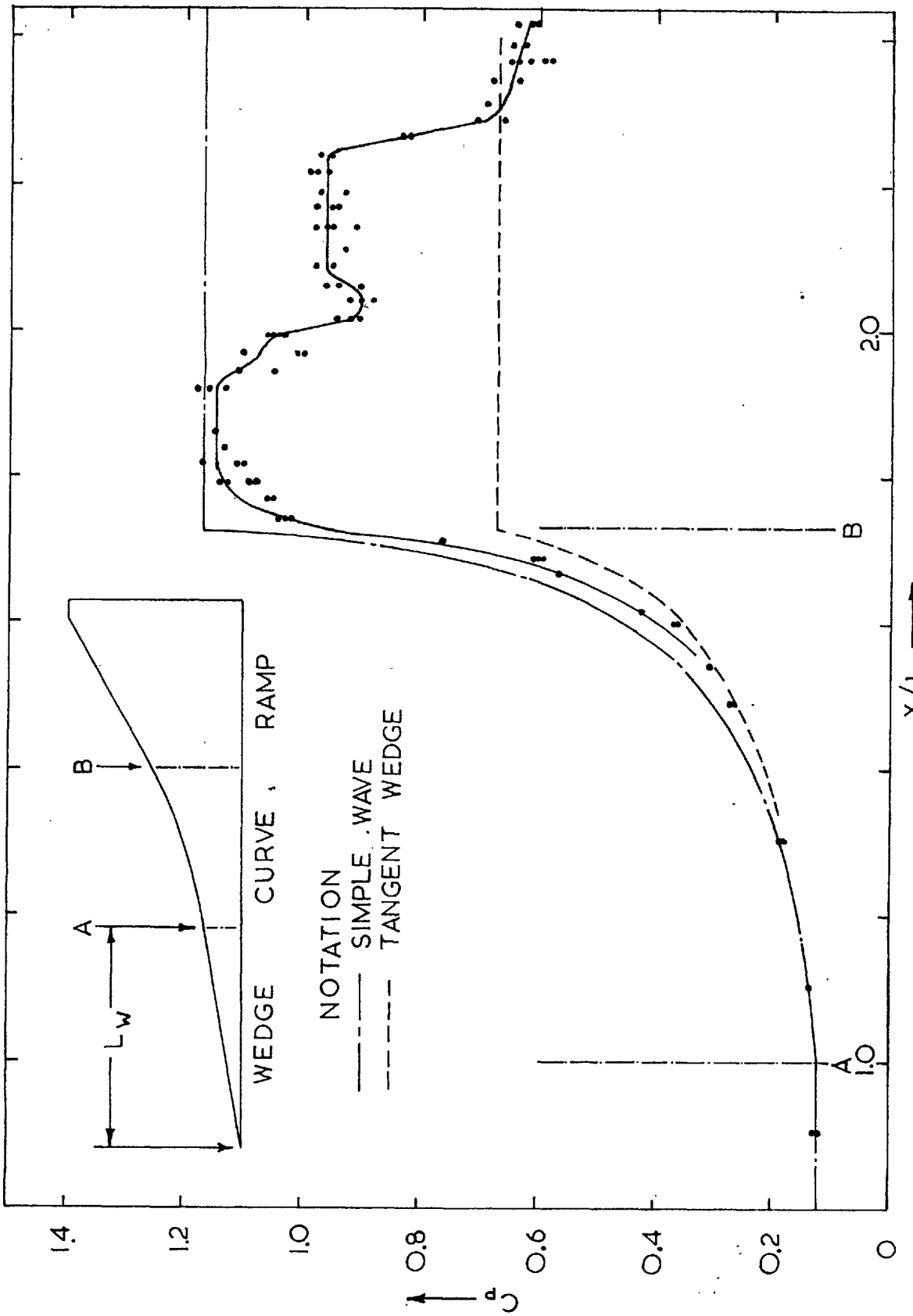


FIG. 7.8 : PRESSURE DISTRIBUTION ON MODEL "B" AT $M_N = 7.5$

the wedge measurements is plotted against ν/ν_0 with M_N as parameter in Fig. A6.

7.4) Pressure Distributions on Model B ; Overfocussed Surface.

7.41) Results and Discussion; The pressure distributions obtained on model B and corrected as in § 7.32 are given in Figs. 7.8 and 7.9. Schlieren photographs of the field are given in Figs. 7.10 and 7.11. The two theoretical estimates given in Figs. 7.8 and 7.9 are from the simple wave theory and the tangent wedge rule. The simple wave theory gives the maximum possible pressure that can occur on the ramp; whilst the tangent wedge rule gives the correct ramp pressure far downstream.

The corrected experimental measurements and the theoretical estimates of the pressure on the wedge forebody and the maximum ramp pressure are compared in Table 7.1.

TABLE 7.1

COMPARISON OF THEORETICAL AND EXPERIMENTAL PRESSURES ON THE WEDGE AND THE RAMP.

	C_p at $M_N = 7.5$			C_p at $M_N = 10$		
	Theory	Expt.	Error	Theory	Expt.	Error
Wedge	0.120	0.119	-1%	0.101	0.104	+3%
Ramp	1.170	1.15	-2%	1.440	1.46	+2%

The good agreement between the corrected experimental

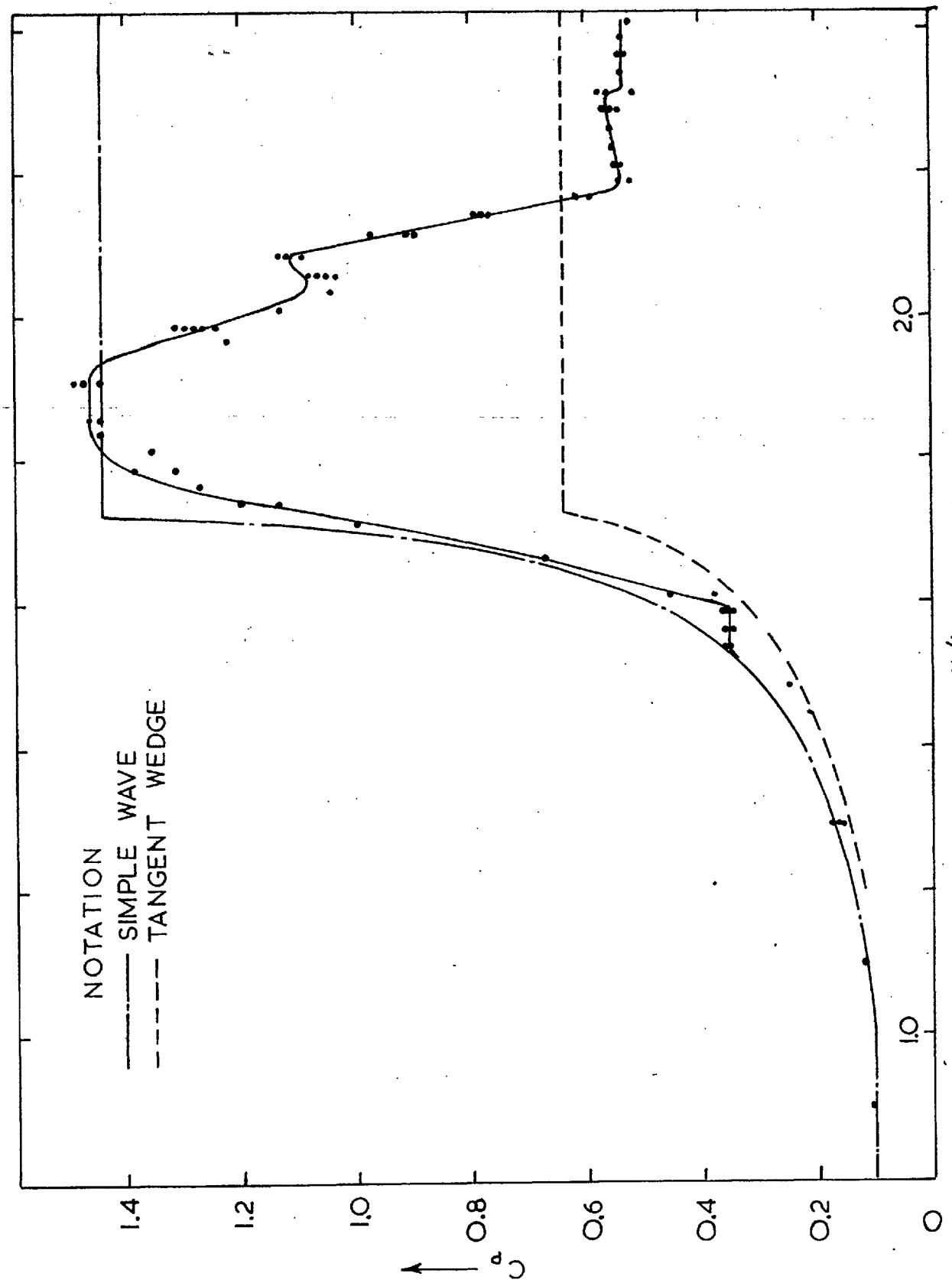


FIG. 7.9 : PRESSURE DISTRIBUTION ON MODEL "B" AT $M_\infty = 10$.



Fig. 7.10, Schlieren photograph of the flow on the overfocussed surface at M = 7.5.

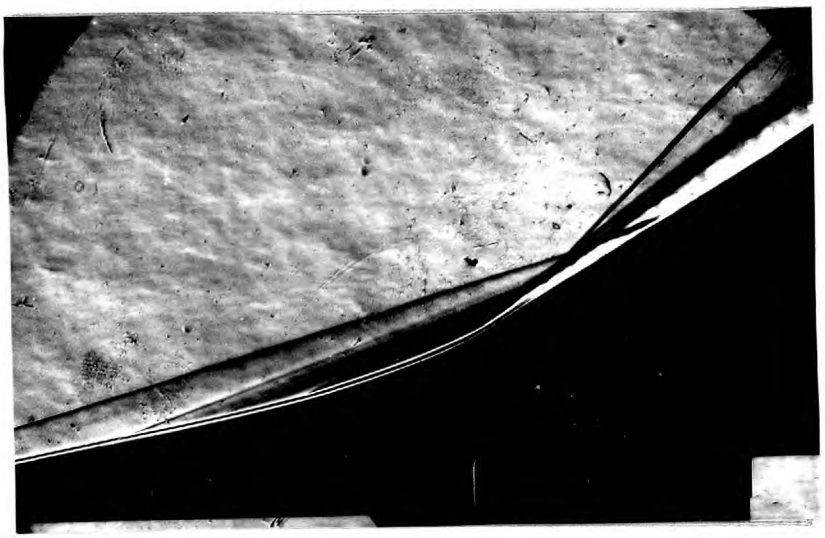


Fig. 7.11, Schlieren photograph of the flow on the overfocussed surface at M = 10.

and the theoretical wedge pressures demonstrates the usefulness of the adopted correction procedure.

To compare the effect of M_N on the surface pressure distribution, the results are replotted in Fig. 7.12 in the form p/p_w, where p_w is the pressure on the wedge forebody. For the experimental results, only the average values are plotted, and is taken as the corrected measured wedge pressure. For the theoretical curves, p_w is taken as the theoretical wedge pressure. The strength of the waves generated on the surface increases rapidly with increase in M_N. Also the distributions on the ramp suggest that the shape as well as the magnitude of the pressure variations is changing markedly with change of M_N.

The interpretation of the field generated at $M_N = 7.5$ is given in Fig. 7.13. The compression waves CF formed by the curved surface, degenerate into a shock EDB, and form a slipline DR and reflected waves EG, DH. This slipline is the inner of the two slip-lines visible in Fig. 7.10. The reflected waves DG, EH cause the first fall-off in the ramp pressure (Fig. 7.8). The shock EDB interacts with the leading edge shock AB to generate the shock BK, the slipline BL, and the reflected wave BM. This reflected wave causes second fall-off in the ramp pressure. Both BM and BL can be seen in Fig. 7.10.

The field generated at $M_N = 10$ is similar to that at $M_N = 7.5$, except that the two groups of reflected waves have moved

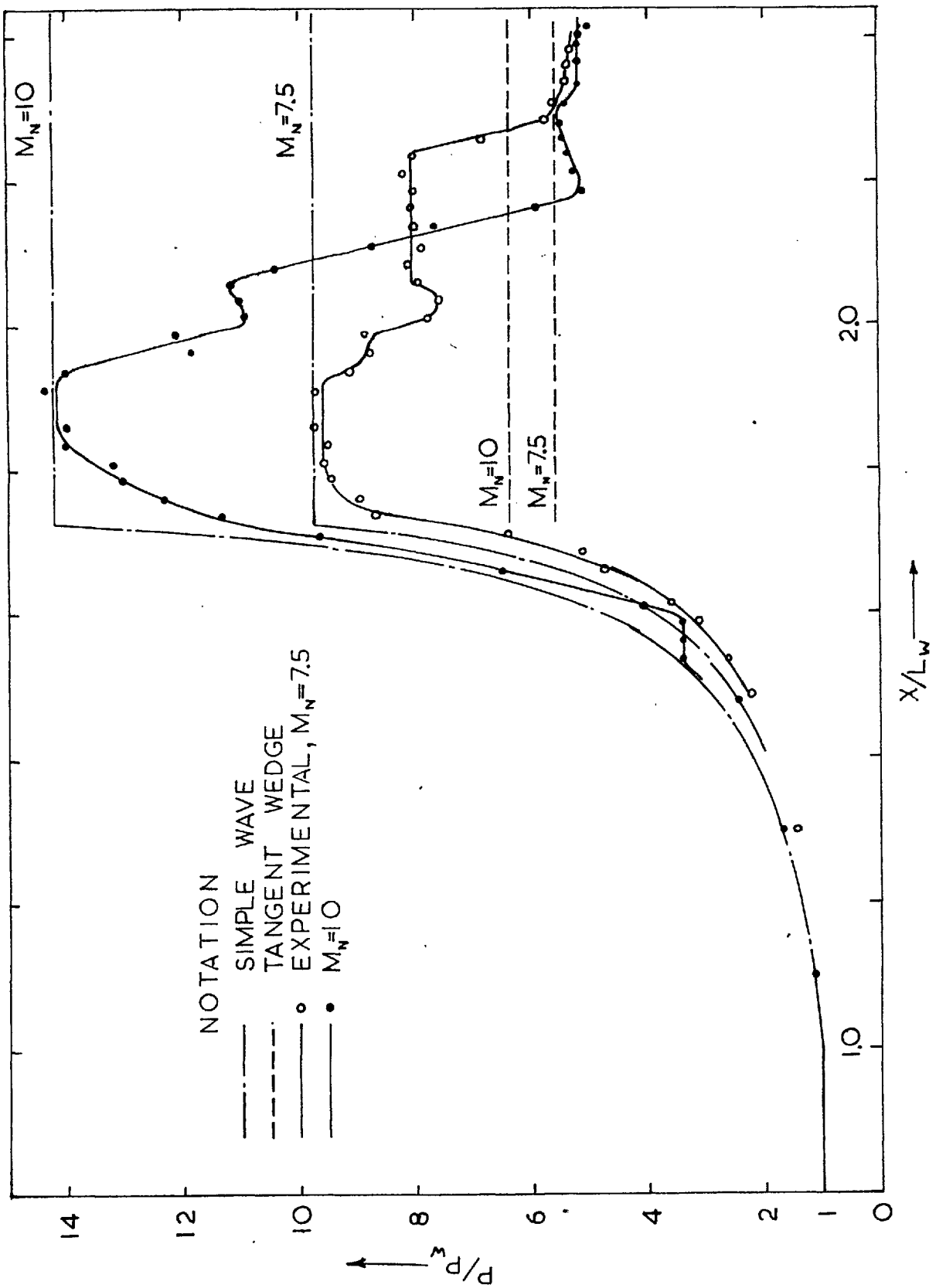


FIG. 7.12 : COMPARISON OF PRESSURE DISTRIBUTIONS ON MODEL 'B' AT M_N=10 & 7.5.

closer together.

Since the inner slipline in Figs. 7.10 and 7.11 is formed away from the ramp surface, there should be a region adjacent to the beginning of the ramp for which no reflected waves hit the ramp. This suggests that the maximum pressure on the ramp should be the simple wave value. The measurements confirm this inference.

The measured pressure at the rear of the model is below the tangent wedge value in both cases. This is consistent with the behaviour of the idealised flows discussed in § 5, in which the pressure just downstream of the first reflected waves to hit the surface (region 5 in Figs. 5.1 and 5.2) is less than the pressure far downstream.

7.42) Viscous Effects on Model B

(i) Separation on the Curved Surface; The pressure distribution at $M_N = 10$ shows a region of constant pressure on the curve.

Initial measurements on generator C at $M_N = 10$ showed that the flow was not repeatable. When side-plates were fitted, the flow was found to be repeatable. Consequently the axial distribution was taken with side-plates fitted.

The axial tests revealed the presence of the constant pressure region. Care was taken to ensure that experimental scatter was eliminated by taking several readings at each tapping in

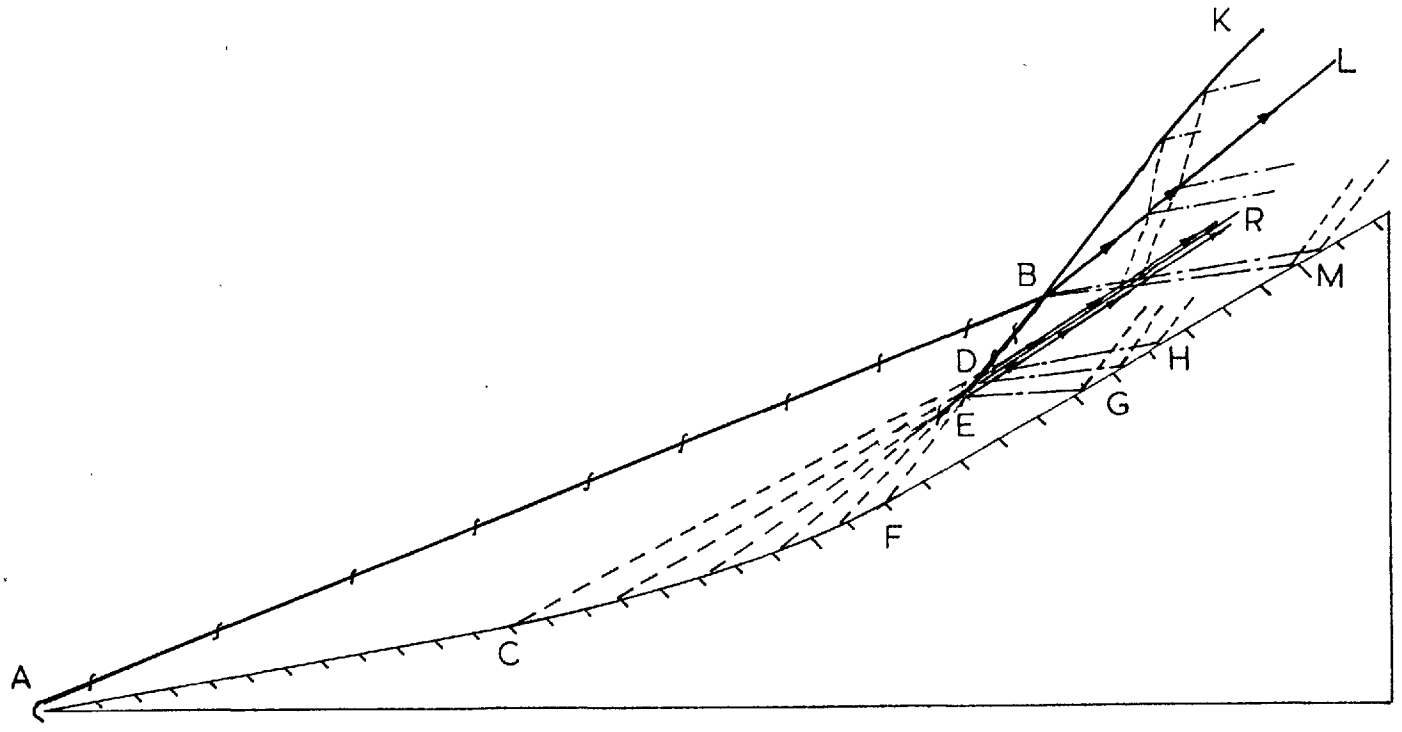


FIG. 7.13 : STRUCTURE OF THE FIELD ON MODEL "B".

the region of constant pressure. It was concluded that a separation bubble formed, and that this generated the non-repeatability. The high pressures on the model forced fluid through the sides of the bubble and caused it to collapse periodically. The side-plates blocked this side-flow and so caused the flow to be steady and repeatable.

(ii) Boundary Layer Displacement Effects: Although the simple wave theory predicts the correct maximum ramp pressure, the measured pressure near the beginning of the ramp differ from the inviscid distributions. This is caused by boundary layer displacement effects. The deviation increases with increase in M_N

7.5) Pressure Distribution on Model C, the Underfocussed Surface

The pressure distribution at $M_N = 10$ on model C is given in Fig. 7.44. The measured wedge pressure exceeded the theoretical value by 20% at the first tapping. This could be caused by shock-boundary layer interaction (c.f. Eq. 6.7). The measured maximum pressure was greater than the theoretical simple wave value. Presumably this was caused by the viscous interaction effects on the wedge.

The theoretical estimates of pressure generated on the ramp multiplied by the ratio of the measured to theoretical wedge pressures is marked in Fig. 7.14 ("compensated" pressures). The compensated simple wave estimate is greater than the measured

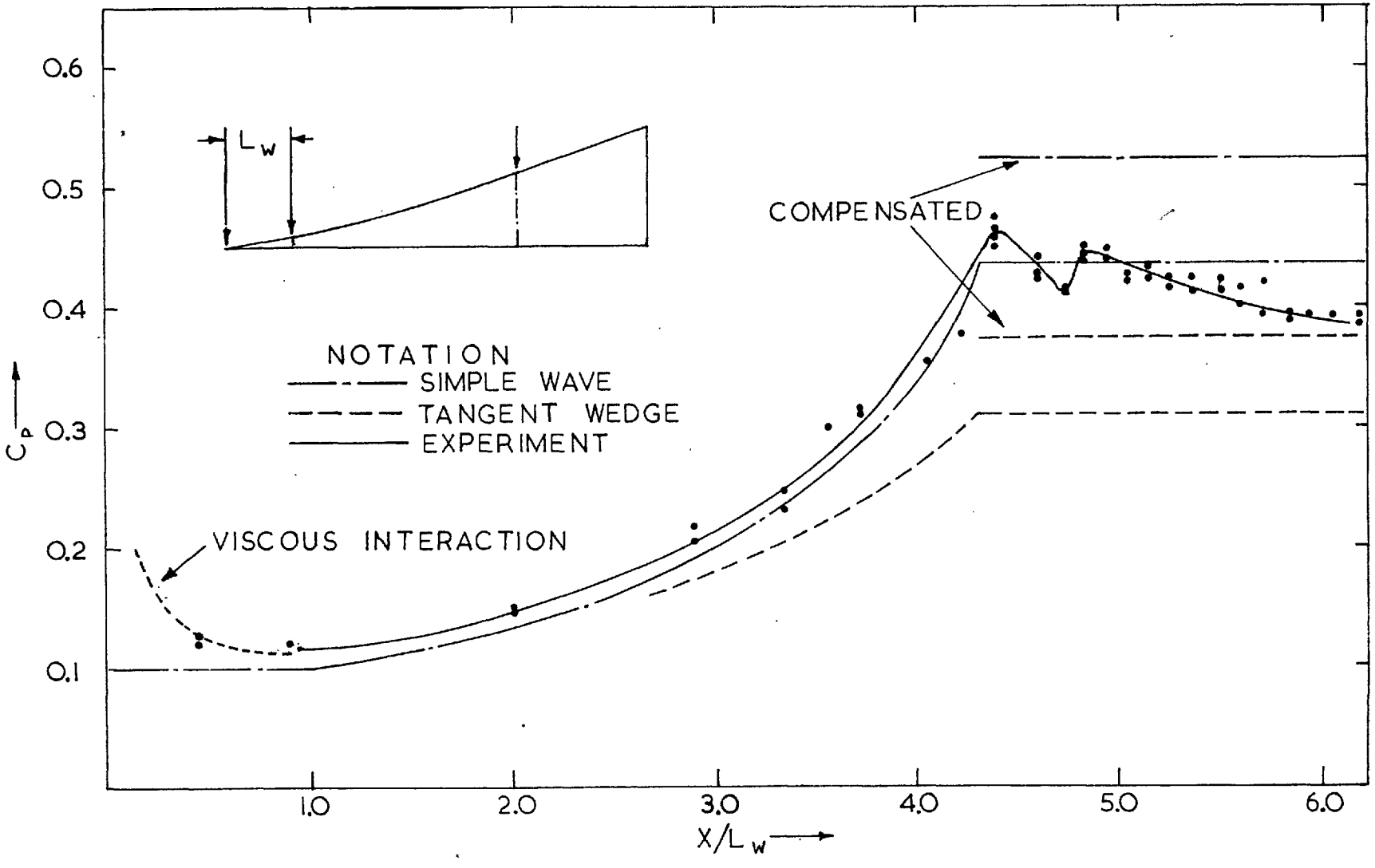


FIG. 7.14 : PRESSURE DISTRIBUTION ON MODEL "C" AT M_N=10.

maximum. This confirms that the first reflected waves to be generated by the concave part of the surface intersect the body upstream of the ramp.

Significant pressure fall-off on the ramp occurred only at $M_N = 10$ on this model.

7.6) Pressure Distributions on Model D - Cubic Surface

The corrected pressure distributions obtained on model D at $M_N = 7.5$ and $M_N = 10$ are given in Fig. 7.15. A photograph of the field generated at $M_N = 10$ is given in Fig. 7.16.

The leading edge of the model generates a shock. Between this shock and the body, the compression waves form a concave curved shock which intersects the leading edge shock. Since the concave shock is not deflected by the leading edge shock, it appears likely that the leading edge shock is very weak. It is neglected in the interpretation of the results.

The pressure distributions obtained on the model agree closely with the similar solutions. In contrast to the field generated on the overfocussed surface, this field is almost independent of Mach number. The pressure distribution on the ramp appears to approach a constant value, suggesting that the tangent wedge value has been attained. The theoretical and measured values of the centrifugal pressure differential (N in Fig. 7.15) are compared in Table 7.2.

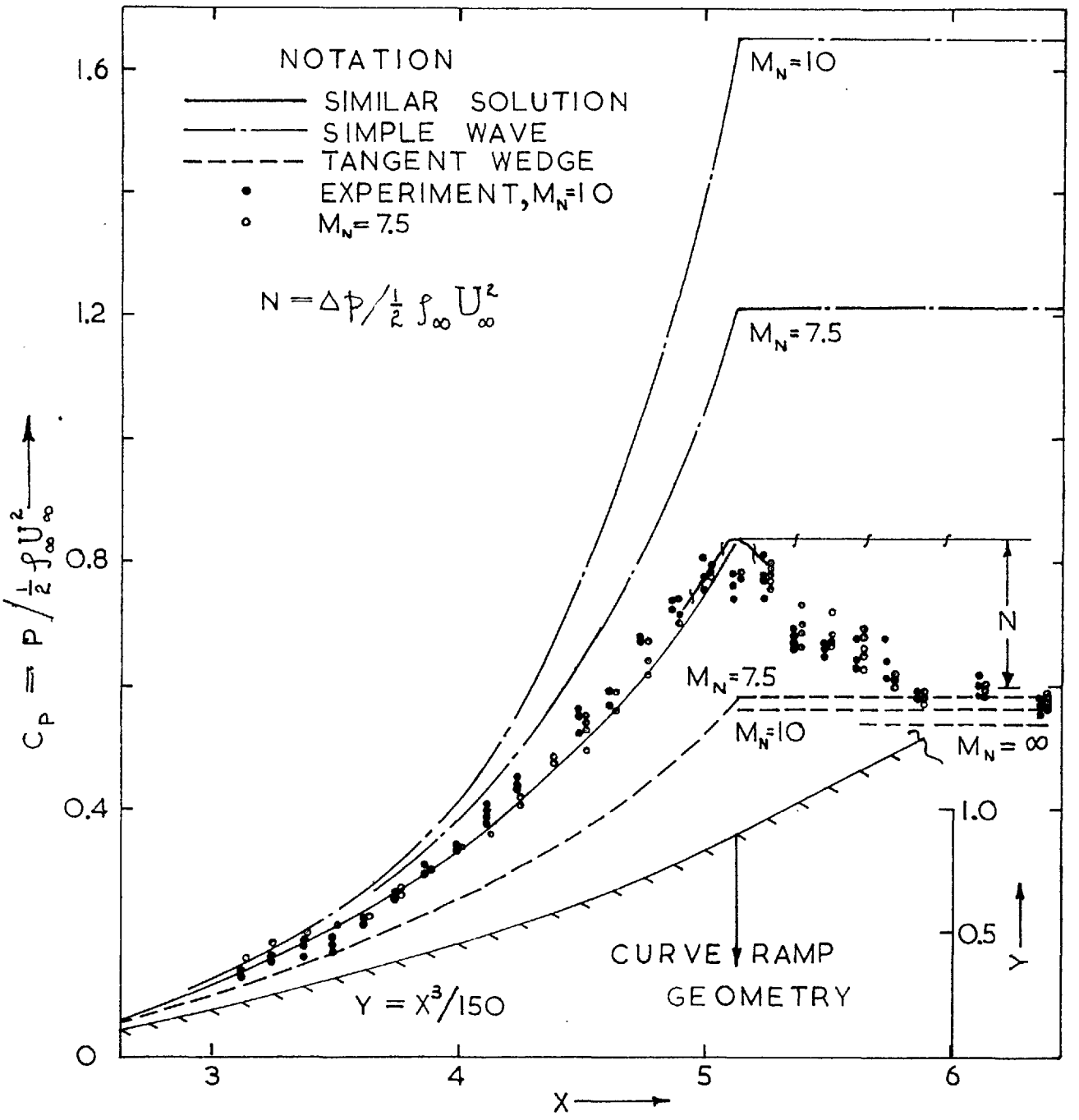


FIG 7.15: PRESSURE DISTRIBUTION ON MODEL "D", CUBIC SURFACE.

TABLE 7.2

MEASURED CENTRIFUGAL PRESSURE DIFFERENTIAL

$\frac{\Delta p}{\rho_\infty U_\infty^2 \vartheta_R^2}$	Theoretical	$M_N = 7.5$	$M_N = 10$
	0.55	0.54	0.58

There is good agreement, but the measurements need to be confirmed by taking the distributions on an extended ramp.

In this experiment a strong concave shock wave was formed only over a relatively small region extending upstream from the rear of the curved part of the surface. A larger region would be obtained on a body with the exponent k nearer one, since it would have a higher slope nearer the origin. Alternatively, the shock wave would be strong over a larger region on a non-similar surface derived as in § 4.2. The latter surface would have the additional advantage that the effects of shock-wave boundary layer interaction would be minimised, since the leading edge angle would now be finite.

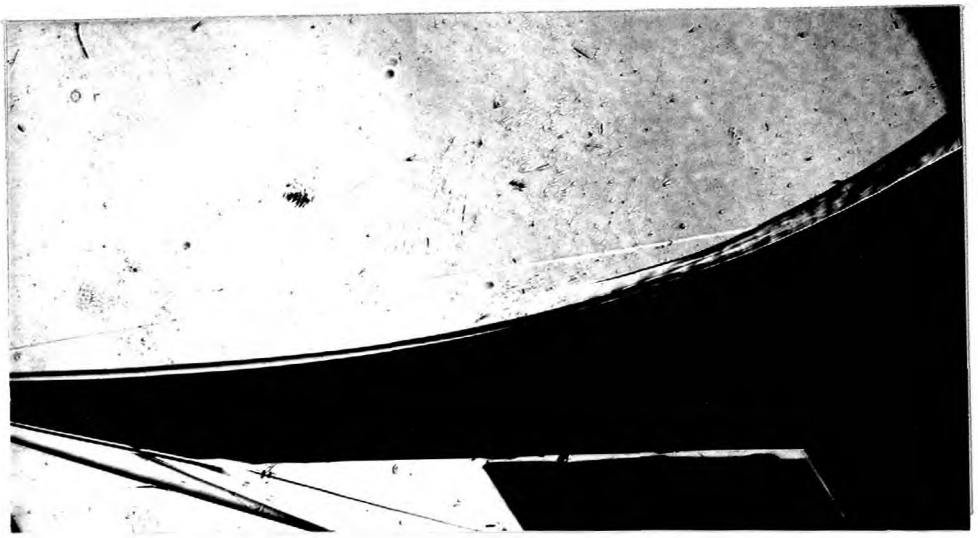


Fig. 7.16, Schlieren photograph of the field generated on the cubic surface at $M_\infty = 10$.

8) Comments on Experimental Facility

The accuracy and repeatability of pressure measurements taken in the Imperial College Gun Tunnel was found to be within ±3%.

Side-plates on two-dimensional models can cause gross spanwise distortions of the field. The spanwise pressure distribution is sensitive to plate size, shape and thickness. In general, their use should be avoided. If they are required to suppress an instability or interference, then they should be no larger than is necessary to suppress the phenomenon.

The source-like flow generated by a conical hypersonic nozzle has considerable effect on the pressures generated on models tested in it. For large models the "local pressure" and "buoyancy" correction methods were found to be inadequate, since they do not account for the incidence effects associated with the free stream. The empirical correction procedure devised and used here appears to be satisfactory.

9) Conclusions

Two principal types of inviscid flow over a concave surface are distinguished. One is an underfocussed flow, which is generated downstream of a concave curved shock wave. The other is an overfocussed flow, in which shocks are formed by compression waves, and shock waves of the same family interact.

The approximate theories which are available for slender bodies in hypersonic flow give widely differing estimates of the surface pressure on a body which generates an underfocussed flow. In the field downstream of a concave shock wave the reflected Mach waves generated at the shock wave and at the sliplines are both expansions. They combine and tend to reduce the pressure generated on the surface by the principal waves. This may be contrasted with the flow over a slender convex surface, where the reflected waves generated at the shock are weak compressions, and those at the sliplines are expansions. The two types of reflected wave tend to cancel, and can have negligible strength.

Because the shock wave generated in the hypersonic flow over a cusped body is a Mach wave at the leading edge, the field far downstream contains a thin layer of gas adjacent to the body across which the pressure is constant to first order. In this respect it is similar to the entropy layer generated in the field far downstream on a blunted slender body, but other than this it has different properties. The fluid in it is cold and dense and

has a much lower entropy than that of the fluid in the region above it. The velocity along the layer is constant throughout the layer and is not much less than the free stream velocity. Its displacement effect on the fluid in the outer region is always of higher order than the effect of variation in M_∞ on the shock wave boundary conditions. The analysis of the flow over cusped bodies showed that the similar solutions to the hypersonic small disturbance equations are the correct first order approximation to the field generated in the outer region of a concave power law body. They predict the correct pressure on the surface of the body.

Comparison of the approximate methods with the results from the similar solutions for both the similar and the derived non-similar surfaces, shows that if the body shape does not have any discontinuities in slope or curvature, then the thin shock layer theory gives a fairly accurate simple estimate of the surface pressure. The simple wave (shock expansion) theory overestimates the surface pressure because it neglects the effect of the reflected Mach waves, and the error increases rapidly with increase in M_∞. The tangent wedge rule underestimates the surface pressure because it accounts only for the shock pressure rise and neglects the centrifugal pressure difference across the shock layer. All of the approximate methods give trivial results downstream of a discontinuity in profile curvature.

The principal mechanisms present in an overfocussed

flow - the formation of shock waves by compression waves and the interaction of shock waves of the same family - both generate strong finite reflected Mach waves at hypersonic conditions. These in turn cause very large pressure variations on the body. The wave structure of an overfocussed flow is usually complex, and numerical methods are required to construct solutions.

The experimental measurements confirmed the theoretical conclusions. Good agreement was obtained between the similar solutions and the measurements on the cubic surface.

APPENDICES

1) Behaviour at the Leading Edge of a Power Law Body

Since $\bar{\sigma} = 1$ at $\bar{x} = 0$, and the oblique shock relations are functions of $\bar{\sigma}^2 - 1$, a simplification occurs as $\bar{\sigma} \to 1$. Put $\bar{\sigma} = 1 + \tau$, $\tau \ll 1$. The oblique shock relations become, as $\tau \to 0$

$$\frac{p_\Delta}{\rho_\infty U_\infty^2} = \frac{p_\infty}{\rho_\infty U_\infty^2} + O(\delta\tau) = \frac{\delta}{\gamma} + O(\delta\tau)$$

$$\frac{\rho_\Delta}{\rho_\infty} = 1 + O(\tau)$$

$$\frac{v_\Delta}{U_\infty} = O(\delta^{1/2}\tau)$$

$$\frac{u_\Delta}{U_\infty} = 1 - O(\delta\tau)$$

These are the orders of magnitude required for the small perturbation theory to apply.

2) **Series Solution of Eq. 4.4 Near Origin**

Since $z \simeq z_0 \xi^{\alpha}$ near the origin, terms like $\xi^{2\alpha}$, $\xi^{\alpha-1}$, $\xi^{\alpha+1}$ will appear in expansion of Eq. 4.4. Hence it is assumed that

$$z = \sum_{i=1}^{\infty} z_i \xi^{a_i}$$

subject only to the conditions that

$$a_1 = \alpha \quad , \quad z_i \neq 0 \quad , \quad a_{i+1}(\alpha) > a_i(\alpha)$$

Similar expressions are assumed for $\frac{d\eta}{d\xi}$ and $\xi \frac{d\mu}{d\xi}$

The solutions are, to third order

(i) if $\alpha < 1/2$

$$z = z_0 \xi^{\alpha} + \left(\frac{\alpha F - C}{G - 2D}\right)\xi + z_0\left(\frac{2-(1+j)\alpha}{G}\right)\xi^{1+\alpha}$$

$$\eta = \eta_0 - \xi/G + \frac{F\xi^{2-\alpha}}{G^2(\alpha-2)z_0} + \frac{1+j}{2G^2}\xi^2$$

$$\mu = \mu_0 - \alpha \ln \xi + \frac{F}{Gz_0}\xi^{1-\alpha} + \frac{(1+j)\alpha\xi}{G}$$

(ii) if $\alpha > \frac{1}{2}$, $\nu = \dfrac{\alpha F - C}{G - 2D}$

$$\zeta = z_0 \xi^{\alpha} + \frac{\alpha F - C}{G - 2D} + \frac{\xi^{2-\alpha}}{z_0}\left\langle \frac{F}{G}\left(\frac{\alpha F - C}{G - 2D}\right)\right\rangle$$

$$\eta = \eta_0 - \xi/G + \frac{F\,\xi^{2-\alpha}}{G^2(\alpha-2)z_0} + \frac{F(G\nu - F)\,\xi^{3-2\alpha}}{z_0^2 G^3(3-2\alpha)}$$

$$\mu = \mu_0 - \alpha \ln\xi + \frac{F}{G z_0}\xi^{1-\alpha} + \frac{F(F - G\nu)\,\xi^{2-2\alpha}}{2G^2 z_0^2}$$

The quantities z_0, η_0 and μ_0 are determined at the match point ξ_m

Error of Computation

Since Ψ in Eq. 4.12 is a function of ζ and ξ, it is possible to form its series near the origin

$$\Psi_0 = \Psi_0 - \frac{e^{\mu_c + \nu\eta_0}}{G}\frac{\xi^{1-\alpha}}{1-\alpha} + \cdots$$

where Ψ_0 is determined from the computed value of Ψ at $\xi = \xi_m$ But by definition $\Psi_b = \Psi(\xi = 0) = -1$. Hence $(1 + \Psi_0)$ is a measure of the truncation error. Ψ_0 is given in the tables.

APPENDIX 3

TABLE OF SELF-SIMILAR SOLUTIONS FOR POWER LAW BODIES.

CONCAVE TWO-DIMENSIONAL SURFACES.

$k = 1.5, \quad = 1.4$

λ	V	R_0	P	Ψ
1.0000, 0	1.2500, 0	6.0000, 0	1.8750, 0	0.0000, 0
9.9499, -1	1.2625, 0	6.1543, 0	1.9224, 0	-3.0454, -2
9.8996, -1	1.2750, 0	6.3179, 0	1.9710, 0	-6.1834, -2
9.8491, -1	1.2875, 0	6.4921, 0	2.0207, 0	-9.4172, -2
9.7984, -1	1.3000, 0	6.6783, 0	2.0717, 0	-1.2751, -1
9.7477, -1	1.3125, 0	6.8784, 0	2.1239, 0	-1.6189, -1
9.6969, -1	1.3250, 0	7.0947, 0	2.1776, 0	-1.9738 -1
9.6460, -1	1.3375, 0	7.3298, 0	2.2327, 0	-2.3404, -1
9.5952, -1	1.3500, 0	7.5874, 0	2.2894, 0	-2.7197, -1
9.5443, -1	1.3625, 0	7.8720, 0	2.3477, 0	-3.1128, -1
9.4935, -1	1.3750, 0	8.1896, 0	2.4080, 0	-3.5210, -1
9.4426, -1	1.3875, 0	8.5484, 0	2.4702, 0	-3.9461, -1
9.3919, -1	1.4000, 0	8.9596, 0	2.5347, 0	-4.3902, -1
9.3412, -1	1.4125, 0	9.4398, 0	2.6017, 0	-4.8562, -1
9.2906, -1	1.4250, 0	1.0014, 1	2.6716, 0	-5.3482, -1
9.2400, -1	1.4375, 0	1.0723, 1	2.7449, 0	-5.8717, -1
9.1895, -1	1.4500, 0	1.1638, 1	2.8224, 0	-6.4350, -1
9.1391, -1	1.4625, 0	1.2904, 1	2.9053, 0	-7.0517, -1
9.0887, -1	1.4750, 0	1.4874, 1	2.9958, 0	-7.7469, -1
9.0383, -1	1.4875, 0	1.8836, 1	3.0978, 0	-8.5691, -1
8.9879, -1	1.5000, 0	∞	3.2546, 0	-9.9822, -1

$k = 2.0,\ \gamma = 1.4$

λ	V	R	P	Φ
1.0000, 0	1.6667, 0	6.0000, 0	3.3333, 0	0.0000, 0
9.9598, -1	1.6833, 0	6.1861, 0	3.4212, 0	-2.4474, -2
9.9193, -1	1.7000, 0	6.3854, 0	3.5117, 0	-4.9920, -2
9.8786, -1	1.7167, 0	6.5997, 0	3.6050, 0	-7.6395, -2
9.8375, -1	1.7333, 0	6.8313, 0	3.7011, 0	-1.0396, -1
9.7962, -1	1.7500, 0	7.0829, 0	3.8004, 0	-1.3267, -1
9.7547, -1	1.7667, 0	7.3579, 0	3.9031, 0	-1.6264, -1
9.7130, -1	1.7833, 0	7.6604, 0	4.0094, 0	-1.9394, -1
9.6711, -1	1.8000, 0	7.9958, 0	4.1196, 0	-2.2672, -1
9.6291, -1	1.8167, 0	8.3711, 0	4.2342, 0	-2.6111, -1
9.5869, -1	1.8333, 0	8.7957, 0	4.3537, 0	-2.9730, -1
9.5446, -1	1.8500, 0	9.2822, 0	4.4786, 0	-3.3554, -1
9.5021, -1	1.8667, 0	9.8487, 0	4.6096, 0	-3.7611, -1
9.4595, -1	1.8833, 0	1.0521, 1	4.7477, 0	-4.1942, -1
9.4169, -1	1.9000, 0	1.1341, 1	4.8943, 0	-4.6602, -1
9.3741, -1	1.9167, 0	1.2374, 1	5.0512, 0	-5.1667, -1
9.3311, -1	1.9333, 0	1.3742, 1	5.2210, 0	-5.7256, -1
9.2881, -1	1.9500, 0	1.5691, 1	5.4083, 0	-6.3565, -1
9.2449, -1	1.9667, 0	1.8844, 1	5.6214, 0	-7.0964, -1
9.2013, -1	1.9833, 0	2.5569, 1	5.8733, 0	-8.0271, -1
9.1574, -1	2.0000, 0	∞	6.3747, 0	-9.9815, -1

$k = 3.0$, $\gamma = 1.4$.

λ	V	R	P	Ψ
1.0000, 0	2.5000, 0	6.0000, 0	7.5000, 0	0.0000, 0
9.9665, -1	2.5250, 0	6.2074, 0	7.7033, 0	-2.0453, -2
9.9326, -1	2.5500, 0	6.4310, 0	7.9133, 0	-4.1846, -2
9.8984, -1	2.5750, 0	6.6731, 0	8.1307, 0	-6.4241, -2
9.8639, -1	2.6000, 0	6.9366, 0	8.3560, 0	-8.7707, -2
9.8292, -1	2.6250, 0	7.2248, 0	8.5897, 0	-1.1233, -1
9.7941, -1	2.6500, 0	7.5422, 0	8.8327, 0	-1.3819, -1
9.7588, -1	2.6750, 0	7.8941, 0	9.0858, 0	-1.6543, -1
9.7233, -1	2.7000, 0	8.2876, 0	9.3501, 0	-1.9417, -1
9.6875, -1	2.7250, 0	8.7318, 0	9.6267, 0	-2.2459, -1
9.6515, -1	2.7500, 0	9.2391, 0	9.9173, 0	-2.5691, -1
9.6153, -1	2.7750, 0	9.8262, 0	1.0224, 1	-2.9138, -1
9.5789, -1	2.8000, 0	1.0517, 1	1.0549, 1	-3.2837, -1
9.5423, -1	2.8250, 0	1.1348, 1	1.0895, 1	-3.6832, -1
9.5056, -1	2.8500, 0	1.2374, 1	1.1267, 1	-4.1190, -1
9.4686, -1	2.8750, 0	1.3687, 1	1.1672, 1	-4.6000, -1
9.4313, -1	2.9000, 0	1.5458, 1	1.2118, 1	-5.1405, -1
9.3939, -1	2.9250, 0	1.8036, 1	1.2622, 1	-5.7643, -1
9.3562, -1	2.9500, 0	2.2331, 1	1.3214, 1	-6.5179, -1
9.3179, -1	2.9750, 0	3.1901, 1	1.3931, 1	-7.5103, -1
9.2792, -1	3.0000, 0	∞	1.5727, 1	-9.9803, -1

$k = 4.0,\ \gamma = 1.4$

λ		V		R		P		Ψ	
1.0000,	0	3.3333,	0	6.0000,	0	1.3333,	1	0.0000,	0
9.9691,	-1	3.3667,	0	6.2157,	0	1.3698,	1	-1.8900,	-2
9.9378,	-1	3.4000,	0	6.4487,	0	1.4076,	1	-3.8714,	-2
9.9061,	-1	3.4333,	0	6.7017,	0	1.4468,	1	-5.9503,	-2
9.8742,	-1	3.4667,	0	6.9777,	0	1.4875,	1	-8.1340,	-2
9.8420,	-1	3.5000,	0	7.2806,	0	1.5298,	1	-1.0431,	-1
9.8095,	-1	3.5333,	0	7.6150,	0	1.5739,	1	-1.2851,	-1
9.7767,	-1	3.5667,	0	7.9869,	0	1.6199,	1	-1.5407,	-1
9.7437,	-1	3.6000,	0	8.4042,	0	1.6680,	1	-1.8113,	-1
9.7104,	-1	3.6333,	0	8.8768,	0	1.7186,	1	-2.0986,	-1
9.6769,	-1	3.6667,	0	9.4185,	0	1.7719,	1	-2.4049,	-1
9.6431,	-1	3.7000,	0	1.0048,	1	1.8283,	1	-2.7329,	-1
9.6092,	-1	3.7333,	0	1.0792,	1	1.8883,	1	-3.0864,	-1
9.5750,	-1	3.7667,	0	1.1691,	1	1 9526,	1	-3.4700,	-1
9.5406,	-1	3.8000,	0	1.2807,	1	2.0221,	1	-3.8907,	-1
9.5060,	-1	3.8333,	0	1.4245,	1	2.0980,	1	-4.3579,	-1
9.4711,	-1	3.8667,	0	1.6196,	1	2.1825,	1	-4.8868,	-1
9.4360,	-1	3.9000,	0	1.9065,	1	2.2788,	1	-5.5026,	-1
9.4005,	-1	3.9333,	0	2.3900,	1	2.3936,	1	-6.2555,	-1
9.3649,	-1	3.9667,	0	3.4834,	1	2.5237,	1	-7.2628,	-1
9.3284,	-1	4.0000,	0	∞		2.8720,	1	-9.9703,	-1

$k = 6.0,\ \gamma = 1.4$

λ	V	R	P	Ψ
1.0000, 0	5.0000, 0	6.0000, 0	3.0000, 1	0.0000, 0
9.9713, -1	5.0500, 0	6.2227, 0	3.0829, 1	-1.7566, -2
9.9422, -1	5.1000, 0	6.4639, 0	3.1688, 1	-3.6017, -2
9.9127, -1	5.1500, 0	6.7264, 0	3.2580, 1	-5.5414, -2
9.8830, -1	5.2000, 0	7.0133, 0	3.3507, 1	-7.5833, -2
9.8530, -1	5.2500, 0	7.3289, 0	3.4474, 1	-9.7358, -2
9.8227, -1	5.3000, 0	7.6782, 0	3.5482, 1	-1.2009, -1
9.7921, -1	5.3500, 0	8.0678, 0	3.6537, 1	-1.4416, -1
9.7612, -1	5.4000, 0	8.5060, 0	3.7645, 1	-1.6971, -1
9.7302, -1	5.4500, 0	9.0039, 0	3.8810, 1	-1.9691, -1
9.6988, -1	5.5000, 0	9.5764, 0	4.0042, 1	-2.2601, -1
9.6672, -1	5.5500, 0	1.0244, 1	4.1350, 1	-2.5727, -1
9.6354, -1	5.6000, 0	1.1036, 1	4.2746, 1	-2.9108, -1
9.6034, -1	5.6500, 0	1.1997, 1	4.4249, 1	-3.2794, -1
9.5711, -1	5.7000, 0	1.3195, 1	4.5880, 1	-3.6854, -1
9.5386, -1	5.7500, 0	1.4748, 1	4.7673, 1	-4.1387, -1
9.5058, -1	5.8000, 0	1.6868, 1	4.9681, 1	-4.6552, -1
9.4727, -1	5.8500, 0	2.0010, 1	5.1991, 1	-5.2613, -1
9.4393, -1	5.9000, 0	2.5361, 1	5.4776, 1	-6.0102, -1
9.4056, -1	5.9500, 0	3.7667, 1	5.8052, 1	-7.0297, -1
9.3711, -1	6.0000, 0	∞	6.7470, 1	-9.9714, -1

$k = 4.0, \quad \gamma = 1.2$

λ		V		R		P		$\mathfrak{V}$	
1.0000,	0	3.6364,	0	1.1000,	1	1.4545,	1	0.0000,	0
9.9845,	-1	3.6545,	0	1.1396,	1	1.4830,	1	-1.7302,	-2
9.9690,	-1	3.6727,	0	1.1826,	1	1.5125,	1	-3.5402,	-2
9.9532,	-1	3.6909,	0	1.2295,	1	1.5431,	1	-5.4368,	-2
9.9374,	-1	3.7091,	0	1.2809,	1	1.5749,	1	-7.4275,	-2
9.9214,	-1	3.7273,	0	1.3375,	1	1.6080,	1	-9.5214,	-2
9.9052,	-1	3.7455,	0	1.4004,	1	1.6427,	1	-1.1729,	-1
9.8890,	-1	3.7636,	0	1.4706,	1	1.6789,	1	-1.4063,	-1
9.8726,	-1	3.7818,	0	1.5499,	1	1.7170,	1	-1.6539,	-1
9.8560,	-1	3.8000,	0	1.6401,	1	1.7532,	1	-1.9176,	-1
9.8393,	-1	3.8182,	0	1.7441,	1	1.7997,	1	-2.1995,	-1
9.8225,	-1	3.8364,	0	1.8658,	1	1.8450,	1	-2.5028,	-1
9.8056,	-1	3.8545,	0	2.0105,	1	1.8935,	1	-2.8311,	-1
9.7885,	-1	3.8727,	0	2.1866,	1	1.9459,	1	-3.1897,	-1
9.7712,	-1	3.8909,	0	2.4071,	1	2.0030,	1	-3.5855,	-1
9.7538,	-1	3.9091,	0	2.6936,	1	2.0663,	1	-4.0289,	-1
9.7362,	-1	3.9273,	0	3.0867,	1	2.1377,	1	-4.5360,	-1
9.7183,	-1	3.9455,	0	3.6718,	1	2.2206,	1	-5.1341,	-1
9.7003,	-1	3.9636,	0	4.6745,	1	2.3219,	1	-5.8778,	-1
9.6820,	-1	3.9818,	0	7.0080,	1	2.4505,	1	-6.9038,	-1
9.6632,	-1	4.0000,	0	∞		2.8324,	1	-9.9805,	-1

$k = 4.0$, $\gamma = 1.6667$

λ	V	R	P	Ψ
1.0000, 0	3.0000, 0	4.0000, 0	1.2000, 1	0.0000, 0
9.9483, -1	3.0500, 0	4.1434, 0	1.2454, 1	-2.1035, -2
9.8959, -1	3.1000, 0	4.2974, 0	1.2926, 1	-4.3142, -2
9.8429, -1	3.1500, 0	4.4637, 0	1.3415, 1	-6.6365, -2
9.7893, -1	3.2000, 0	4.6440, 0	1.3924, 1	-9.0760, -2
9.7353, -1	3.2500, 0	4.8407, 0	1.4453, 1	-1.1639, -1
9.6808, -1	3.3000, 0	5.0565, 0	1.5004, 1	-1.4335, -1
9.6259, -1	3.3500, 0	5.2951, 0	1.5580, 1	-1.7174, -1
9.5707, -1	3.4000, 0	5.5609, 0	1.6182, 1	-2.0167, -1
9.5153, -1	3.4500, 0	5.8600, 0	1.6813, 1	-2.3331, -1
9.4596, -1	3.5000, 0	6.2002, 0	1.7477, 1	-2.6685, -1
9.4038, -1	3.5500, 0	6.5926, 0	1.8177, 1	-3.0255, -1
9.3478, -1	3.6000, 0	7.0528, 0	1.8918, 1	-3.4072, -1
9.2917, -1	3.6500, 0	7.6037, 0	1.9707, 1	-3.8181, -1
9.2354, -1	3.7000, 0	8.2811, 0	2.0554, 1	-4.2641, -1
9.1791, -1	3.7500, 0	9.1445, 0	2.1470, 1	-4.7539, -1
9.1226, -1	3.8000, 0	1.0302, 1	2.2476, 1	-5.3009, -1
9.0661, -1	3.8500, 0	1.1978, 1	2.3605, 1	-5.9277, -1
9.0094, -1	3.9000, 0	1.4750, 1	2.4916, 1	-6.6778, -1
8.9522, -1	3.9500, 0	2.0857, 1	2.6493, 1	-7.6493, -1
8.8946, -1	4.0000, 0	∞	3.0136, 1	-9.9741, -1

4) Streamline Distribution in the Working Section

Consider a streamtube having a cross-sectional area A at some distance x which expands to an area $A + dA$ over a length dx. Since similar areas are proportional to corresponding lengths squared,

$$\frac{A + dA}{A} = \left(\frac{y + \alpha\, dx}{y}\right)^2, \quad \alpha << 0$$

where y is the distance of a given streamline (having a slope α) from the centre of symmetry. Hence, as $dx \to 0$

$$\frac{1}{A}\frac{dA}{dx} = \frac{2\alpha}{y}$$

It can be shown* by using the concepts of one-dimensional gasdynamics that for an isentropic flow :

$$\frac{A_*}{A} = \left(\frac{\gamma+1}{2}\right)^{\frac{1}{2}\left(\frac{\gamma+1}{\gamma-1}\right)} M \left(1 + \frac{\gamma-1}{2} M^2\right)^{-\frac{1}{2}\left(\frac{\gamma+1}{\gamma-1}\right)}$$

where A_* is the cross-sectional area of a streamtube at $M = 1$

If $M \gg 1$,

$$\frac{A_*}{A} \propto M^{(1/\varepsilon - 1)}, \quad \frac{dA}{A} = \left(\frac{1}{\varepsilon} - 1\right)\frac{dM}{M}$$

Hence

$$\hat{\omega} = \frac{\alpha}{y} = \frac{1}{2}\left(\frac{1}{\varepsilon} - 1\right)\frac{1}{M}\frac{dM}{dx}$$

---

*See, for example, Liepmann and Roshko (1957).

This expression was used to estimate the incidence factor $\tilde{\omega}$ in the Imperial College Gun Tunnel from the measured axial Mach number M = M(x). Curves of ($\tilde{\omega}/R_E$) against (x/R_E) are given in Fig. A1. The scatter of the calculated points is caused by the graphical differentiation of the Mach number distribution.

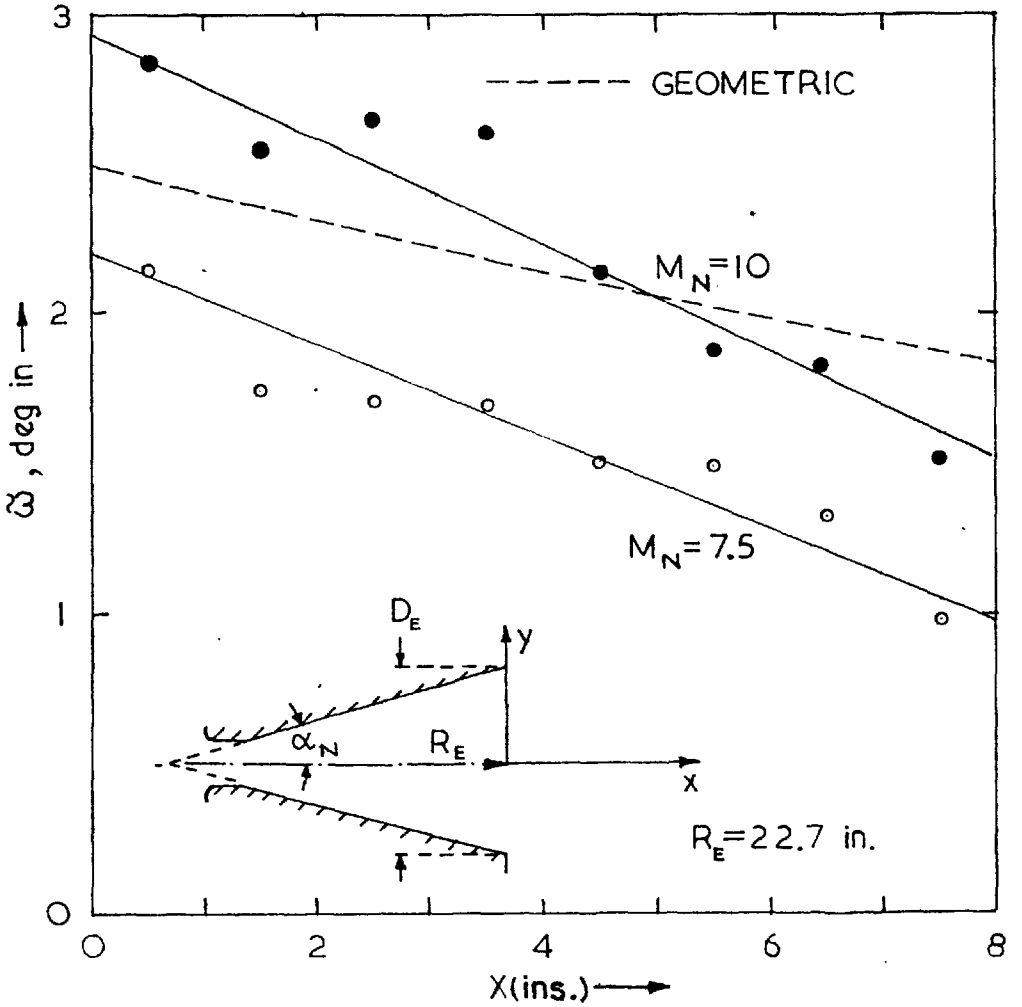


FIG A1 : STREAMLINE INCIDENCE DISTRIBUTION.

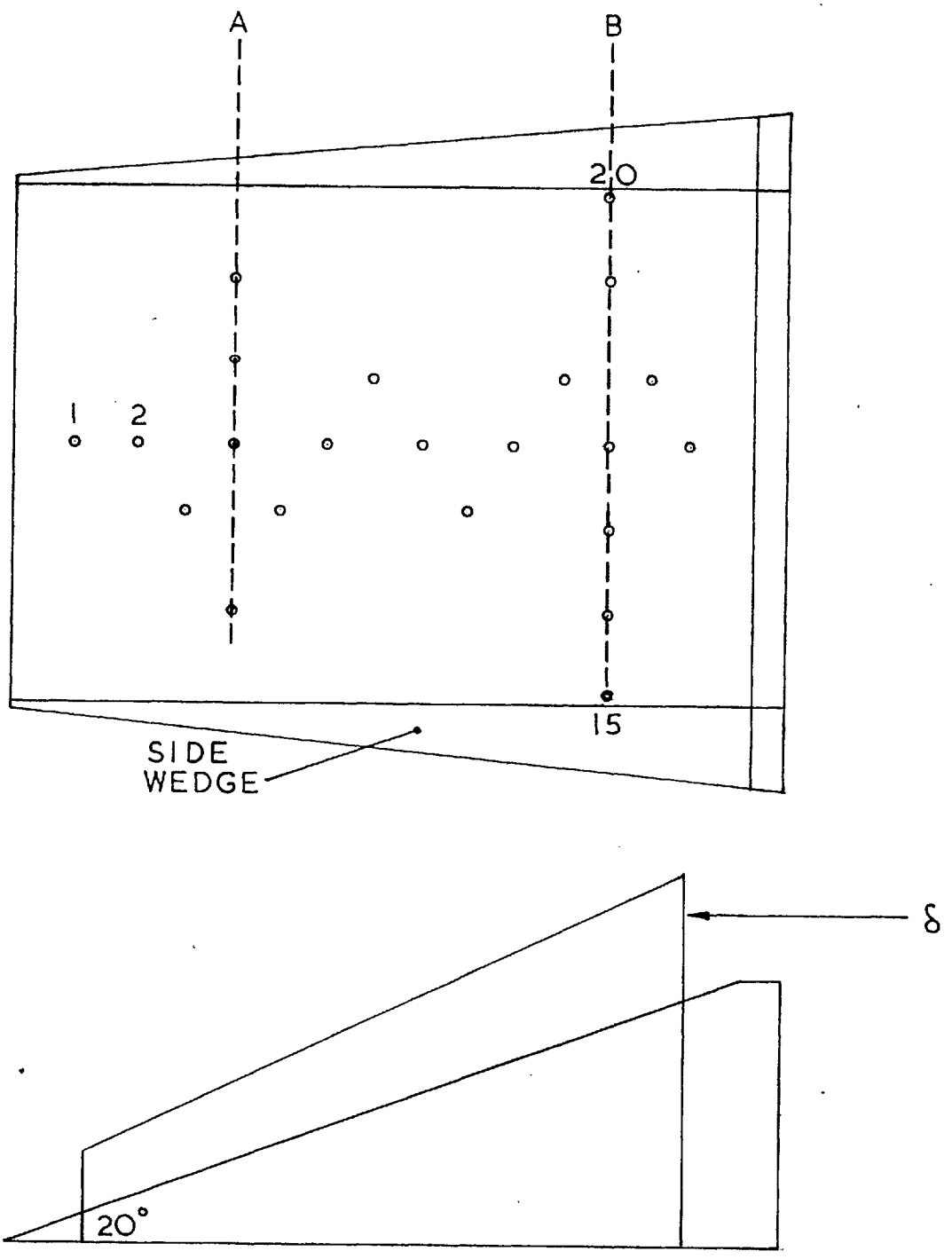


FIG. A2: MODEL "A", CALIBRATING WEDGE.

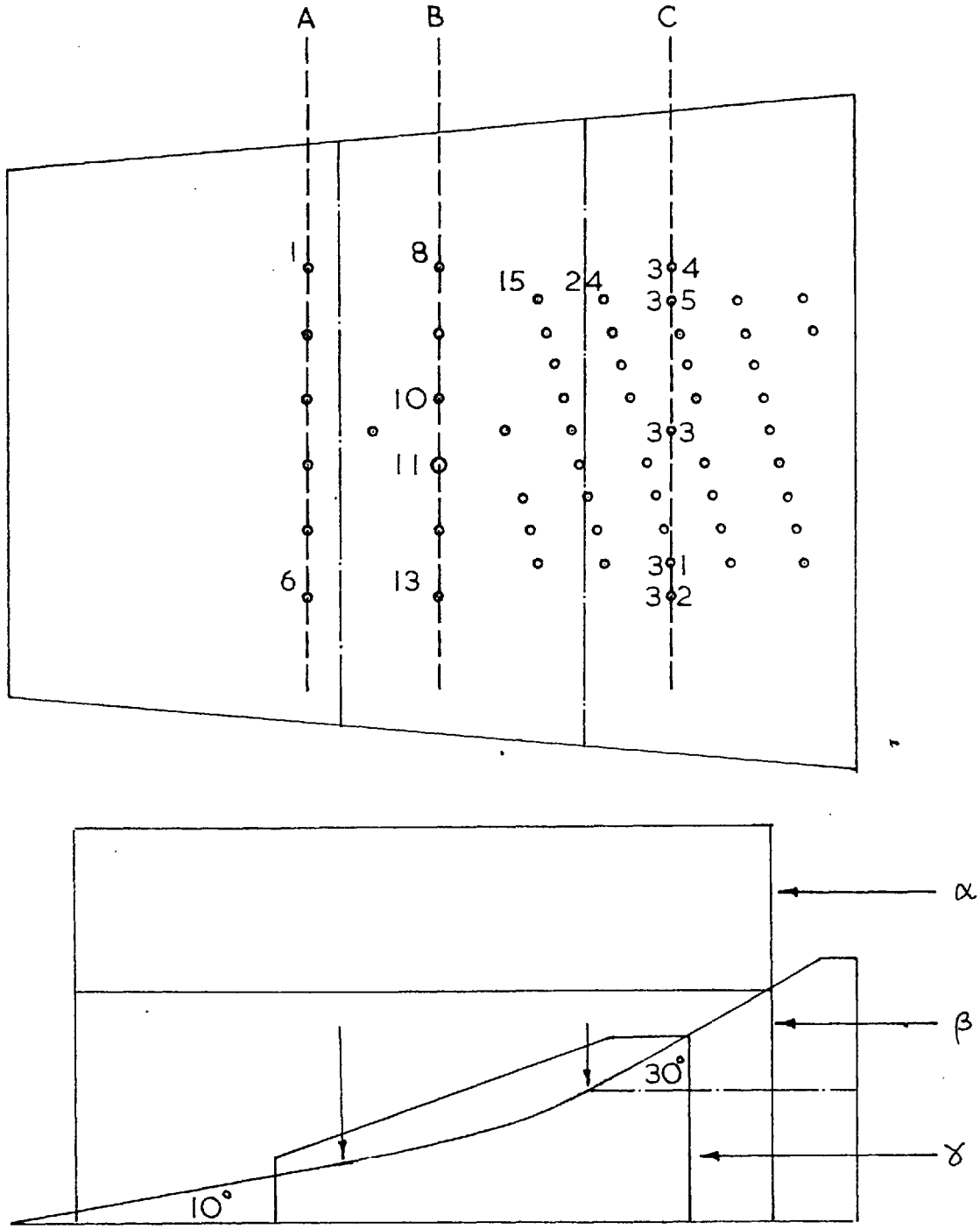


FIG. A3 : MODEL "B", OVERFOCUSSED SURFACE.

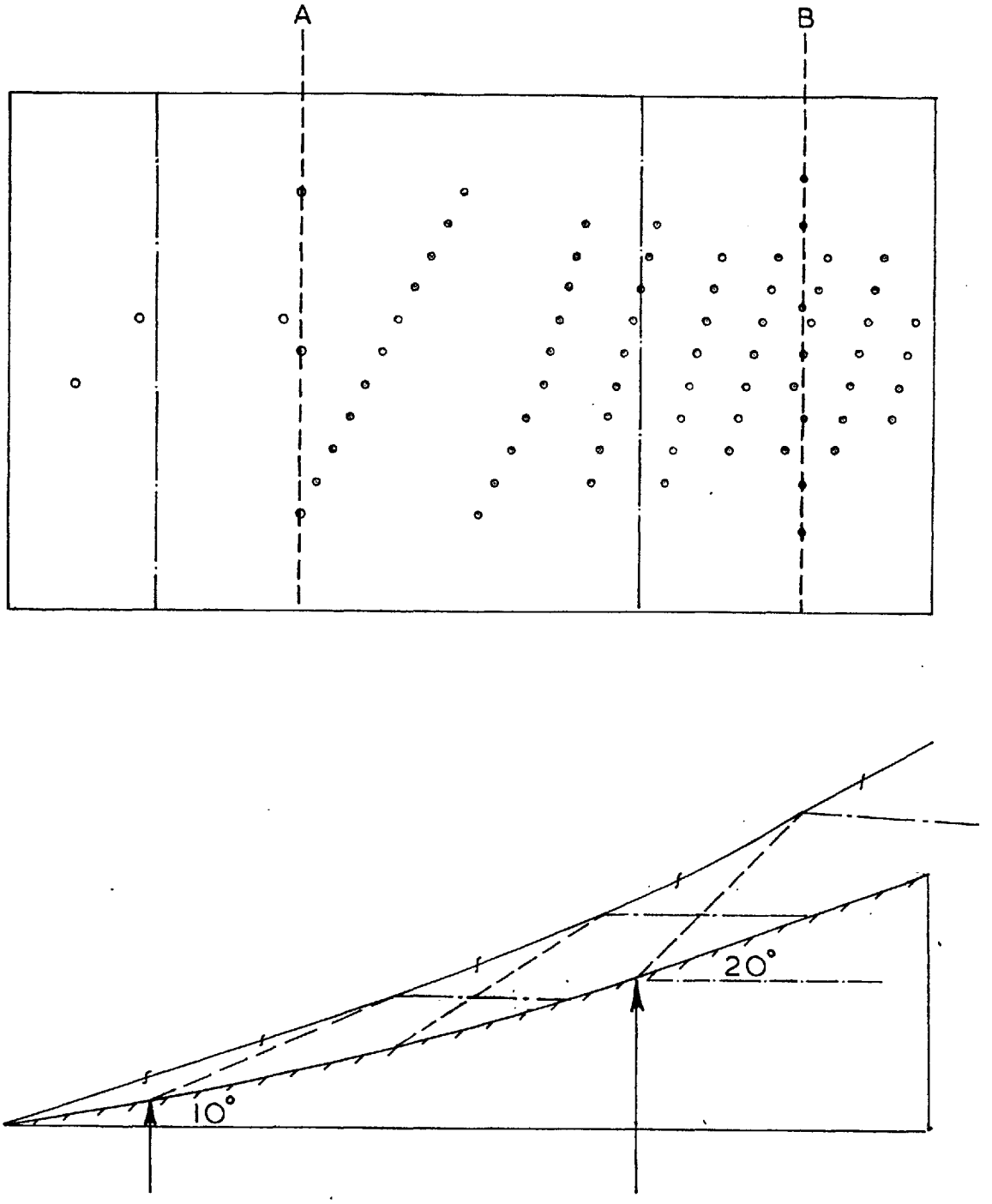


FIG.A4 : MODEL"C",UNDERFOCUSSED SURFACE .

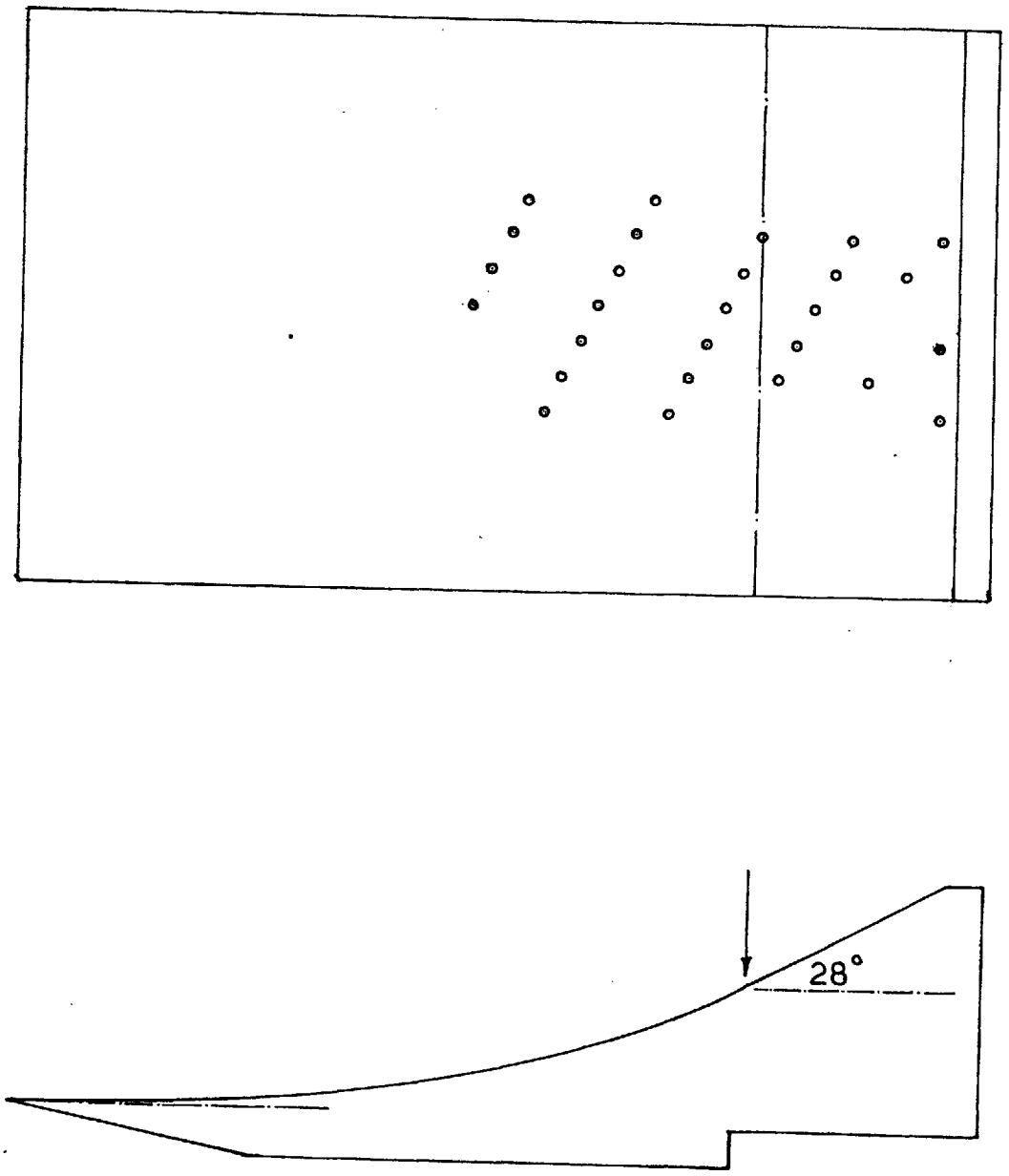


FIG.A 5: MODEL "D", CUBIC SURFACE.

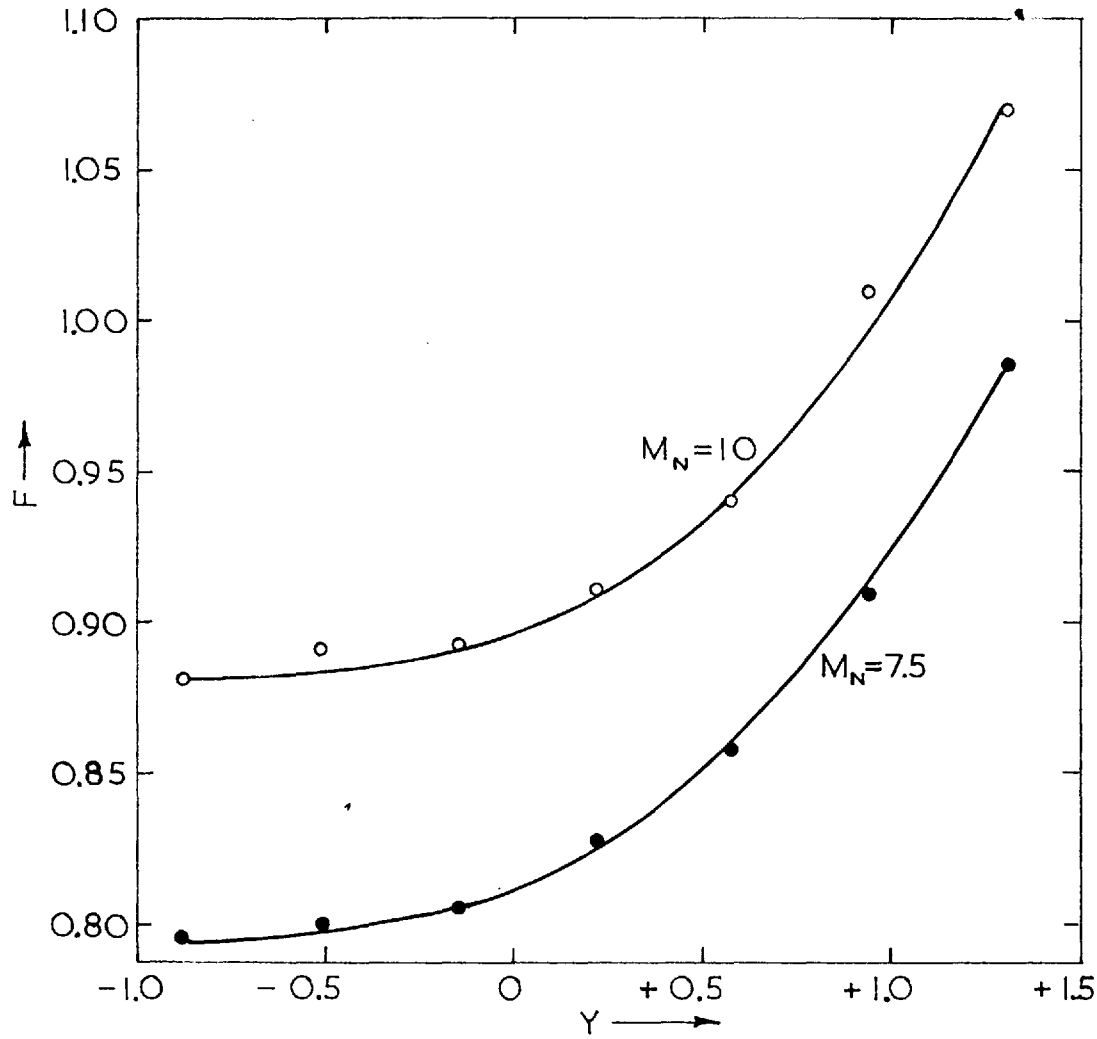


FIG. A 6 : EMPIRICAL INCIDENCE CORRECTION FACTOR

5) Leading Edge Effects on Models

Only two possible effects were considered; these were:

(i) the effect of leading edge bluntness on inviscid attached shock wedge pressure,

(ii) shock-boundary layer interaction

Estimation of the effect (i) was based on calculations given by Chernyi (1961, p.222) for $M_\infty = \infty$*. For a leading edge thickness $t_{L.E} = 0.002''$, effects were negligible (i.e. less than 2%) at 0.10".

Estimation of effect (ii) based on the formula for weak interaction ($\bar{\chi} \ll 1$) (Hayes and Probstein, 1959, p.349)

$$\frac{p}{p_w} = 1 + 0.31\,\bar{\chi}\,, \qquad \bar{\chi} = \frac{M_w^3 \sqrt{C_w}}{\sqrt{R_{Ew}}}$$

where C is the Chapman-Rubesin factor, and the subscript w denotes inviscid conditions behind the attached shock. According to this formula $p/p_w < 1.02$ at the first set of tappings on models A and B, but on model C $p/p_w = 1.25$ at $M_N = 10$.

---

*The drag coefficient C_D of the leading edge was assumed to be the Newtonian value, $C_D = 2$.

LIST OF SYMBOLS

B	$y = B(x)$ expression for body shape
C_p	pressure coefficient $C_p \equiv p / \frac{1}{2} \rho_\infty U_\infty^2$
C_{pc}	pressure coefficient corrected for conical flow
D_E	diameter of gun tunnel nozzle at exit plane
K	hypersonic similarity parameter $K = M_\infty \varphi_1$
M	Mach number
M_N	nominal tunnel Mach number
M_∞	free stream Mach number in uniform flow
P	non-dimensional pressure in similar solutions Eq. 3.26
P_c	corrected pressure ratio (Eq. 6.4)
R	non-dimensional density in similar solution (Eq. 3.26)
R_E	distance from nozzle exit plane to nozzle cone apex
R_1, R_2	reflection coefficients, § 5.5
U_∞	free stream velocity
V	non-dimensional velocity in similar solutions (Eq. 3.26)
V_s, V_p	velocity of shock and piston in unsteady flow (Eq. 3.21)
a	speed of sound
j	$j = 0$ for two-dimensional flow
	$j = 1$ for axially symmetric flow
k	exponent in cusped body shape (Eq. 3.6)
l	typical length
n	normals to surface in boundary layer co-ordinates

p static pressure

p_B barrel pressure in gun tunnel

p_D drive pressure in gun tunnel

p_R effective reservoir pressure

p_w theoretical pressure generated on wedge forebodies on the models

q local speed $q = (u^2 + v^2)^{1/2} = (\tilde{u}^2 + \tilde{v}^2)^{1/2}$

s distance along the body surface in boundary layer co-ordinates

t time, in similar solutions $x = U_\infty t$ (Eq. 3.21)

u velocity in x - direction

$\tilde{u}$ velocity in s - direction

v velocity in y - direction

$\tilde{v}$ velocity in n - direction

x streamwise co-ordinate

y normal co-ordinate

z non-dimensional speed of sound, $z = \sqrt{\gamma p/R}$

Ψ non-dimensional stream function defined in Eq. 4.11

α exponent in $z \simeq z_0 \xi^{\alpha}$, (Eq.3.33d)

α_N tunnel nozzle cone angle

β error exponent

γ specific heat ratio

δ free stream Mach number parameter

ε infinite density ratio $\varepsilon = \gamma - 1 / \gamma + 1$

ξ variation parameter in § 5.4

η $\ln \lambda$

ϑ_b local body slope $dy_b/dx = \tan \vartheta_b$

ϑ_v slipline angle relative to the second wedge or ramp in idealized flows, § 5

λ transformed independent variable in similar solutions (Eq. 4.1)

μ $\ln R$, (Eq. 3.26)

ξ $V - k$ in similar solutions

ω incidence distribution function

ρ gas density

σ shock wave angle measured with respect to incident stream $dy_s/dx = \tan \sigma$

ν error exponent

φ independent variable in similar solutions (Eq. 3.26)

φ_1, φ_2 wedge angles in double wedge problem $\varphi_* = \varphi_1 + \varphi_2$

χ variation coefficient in § 5.4

Subscripts

Those generally used are :

$_L$	denotes conditions at model leading edge
$_N$	nominal gun tunnel conditions
$_b$	denotes conditions at the body
$_s$	denotes conditions at the shock
$_\infty$	conditions in free stream

REFERENCES

Baradell, D.L., and Bertram, M.H.

The blunt plate in hypersonic flow, NASA TN D-408, (Oct. 1960)

Barenblatt, G.I.

On limiting self-similar motions in the theory of unsteady filtration of a gas in a porous medium and the theory of the boundary layer, Prikl. Mat. Mekh. (18) 409-414 (1954).

Bird, G.A.

Effect of wave interactions on pressure distributions in supersonic and hypersonic flow, AIAA J. (7) 634-639 (1963).

Chernyi, G.G.

Introduction to Hypersonic Flow, (Academic Press, New York, 1961).

Chu, B.T.

On weak interaction of strong shock and Mach waves generated downstream of the shock, J. Aero. Sci. (19) 433 (1952).

Cole, J.D.

Newtonian flow theory for slender bodies, J. Aero. Sci. (24) 448 (1957).

Collar, A.R.

Iterative solutions of shocks and Prandtl-Meyer expansions, J. R. Aero. Soc. (Nov. 1959).

Courant, R., and Friedrichs, K.O.

Supersonic Flow and Shock Waves, (Interscience, New York, 1948).

Eggers, A.J., Jr., and Syvertson, C.A.

Inviscid flow about airfoils at high supersonic speeds, NACA TN 2646 (1952).

Epstein, P.S.

On the air resistance of projectiles, Proc. Nat. Acad. Sci., U.S.A., (17) 532 (1931).

Ferri, A.

Method of Characteristics, Vol. 6, Section G of the Princeton Series, High Speed Aerodynamics and Jet Propulsion, (Princeton, 1954).

Freeman, N.C.

On the theory of hypersonic flow past plane and axially symmetric bluff bodies, J. Fluid Mech. (1) 366 (1956).

Freeman, N.C.

An approach to second order solutions of hypersonic small disturbance theory, NPL Aero. Rep.1035, ARC 23999, Hyp. 265, (1962).

Hayes, W.D., and Probstein, R.F.

Hypersonic Flow Theory, (Academic Press, New York, 1959).

Johannesen, N.H.

Experiments on two-dimensional supersonic flow in corners and over concave surfaces, ARC. FM. 1669, (Jan. 1952).

Lees, L.

Hypersonic flow, Proc. 5th. Internatl. Aero. Conference, Los Angeles, Inst. Aero. Sci., New York, 241-276 (1955).

Lees, L., and Kubota, T.

Inviscid hypersonic flow over blunt-nosed slender bodies, J. Aero. Sci. (24) 195-202 (1957).

Liepmann, H.W., and Roshko, A.

Elements of Gasdynamics, (Wiley, New York, 1957).

Lighthill, M.J.

The flow behind a stationary shock, Phil. Mag. (40) 214 (1949).

Lighthill, M.J.

Higher Approximations, Vol.6, Section E of the Princeton Series, High Speed Aerodynamics and Jet Propulsion, (Princeton, 1954).

Needham, D.A.

A progress report on the Imperial College Gun Tunnel, Imperial College Aero. TN 118, (1963).

Sedov, L.I.

Similarity and Dimensional Methods in Mechanics, (Gostekhizdat, Moscow, English Translation (M. Holt, ed.), Academic Press, New York and London, 1959).

Vas, I.E., and Bogdonoff, S.M.

Hypersonic studies of blunt unswept wings, Princeton University Dept. of Aero. Eng., Rep. 450, (April, 1959).

Yakura, J.K.

Theory of entropy layers and nose-bluntness in hypersonic flow, Progress in Astronautics and Rocketry, Vol. 7, Hypersonic Flow Research, (Academic Press, New York, 1962